Chemical diversity of gas in distant galaxies

T. Ramburuth-Hurt, A. de Cia, J.-K. Krogager, C. Ledoux, P. Petitjean, C. Péroux, M. Dessauges-Zavadsky, J. Fynbo, M. Wendt, Nicolas F. Bouché, et al.

A&A 672, A68 (2023)
https://doi.org/10.1051/0004-6361/202244609

Astronomy & Astrophysics

Chemical diversity of gas in distant galaxies

Metal and dust enrichment and variations within absorbing galaxies

T. Ramburuth-Hurt[1], A. De Cia[1], J.-K. Krogager[1,2], C. Ledoux[3], P. Petitjean[4], C. Péroux[5,6], M. Dessauges-Zavadsky[1], J. Fynbo[7,8], M. Wendt[9], N. F. Bouché[2], C. Konstantopoulou[1], and I. Jermann[1]

[1] Department of Astronomy, University of Geneva, Chemin Pegasi 51, Versoix, Switzerland
e-mail: tanita.ramburuth-hurt@unige.ch
[2] Univ. Lyon, Univ. Lyon1, ENS de Lyon, CNRS, Centre de Recherche Astrophysique de Lyon UMR5574, 69230 Saint-Genis-Laval, France
[3] European Southern Observatory, Alonso de Córdova 3107, Vitacura, Casilla 19001, Santiago, Chile
[4] Institut d'Astrophysique de Paris, Sorbonne Université and CNRS, 98bis Boulevard Arago, 75014 Paris, France
[5] European Southern Observatory, Karl-Schwarzschild-Str. 2, 85748 Garching, Germany
[6] Aix-Marseille Université, CNRS, LAM (Laboratoire d'Astrophysique de Marseille) UMR 7326, 13388 Marseille, France
[7] Cosmic Dawn Center (DAWN), Copenhagen, Denmark
[8] Niels Bohr Institute, University of Copenhagen, Jagtvej 128, 2200 Copenhagen N, Denmark
[9] Institut für Physik und Astronomie, Universität Potsdam, Karl-Liebknecht-Str. 24/25, 14476 Golm, Germany

Received 27 July 2022 / Accepted 23 January 2023

ABSTRACT

The chemical composition of gas in galaxies can be measured in great detail using absorption spectroscopy. By studying gas in galaxies in this way, it is possible to investigate small and faint galaxies, which are the most numerous in the universe. In particular, the chemical distribution of gas in absorbing systems gives us insight into cycles of gas in and around galaxies. In this work we study chemical enrichment within 64 damped Lyman-α absorption systems (DLAs) for redshifts in the range $1.7 < z < 4.2$. We use high-resolution spectra from VLT/UVES to infer dust depletion from relative abundances of several metals. Specifically, we performed a component-by-component analysis within DLAs, and characterised variations in their chemical enrichment. Unlike hydrogen, the metal columns can be characterised according to their individual components. We used them to derive the dust depletion, which is an indicator of chemical enrichment. Our main results are as follows. Firstly, we find that some DLAs are chemically diverse within themselves (with the measure of dust depletion $[\mathrm{Zn/Fe}]_{\mathrm{fit}}$ ranging up to 0.62 dex within a single system), suggesting that the absorbing gas within these galaxies is chemically diverse. Secondly, although we do not find a clear trend of decreasing dust depletion with redshift, we do see that the most chemically enriched systems are at lower redshifts. We also observe evidence for dust-poor components at all redshifts, which may be due to the accretion of pristine gas onto galaxies. By combining the chemical and kinematic properties of the individual gas components, we observe potential signatures of infalling gas with low depletion at velocities below $\sim$100 km s^{-1}, and outflows with high depletion and velocities of $\sim$600 km s^{-1}. Finally, we find over-abundances of α-elements (an enhancement of $\sim$0.3 dex) and under-abundances of Mn in several gas components, which is likely a signature of core-collapse supernovae nucleosythesis in the ISM. We observe these effects mostly at lower levels of chemical enrichment.

Key words. galaxies: ISM – galaxies: kinematics and dynamics – dust, extinction – evolution – quasars: absorption lines

1. Introduction

Chemical abundances in galaxies across cosmic time play a crucial role in our understanding of galactic baryon cycles (Maiolino & Mannucci 2019). In particular, damped Lyman-α absorption systems (DLAs), defined as having a neutral hydrogen (H I) column density of $N(\mathrm{H\,I}) > 10^{20.3}$ cm^{-2} (e.g. Wolfe 1986), are excellent laboratories for studying chemical abundances in galaxies out to high z. This criterion ensures shielding of the gas cloud from ionising radiation. DLAs are H I-rich absorption systems, and are associated with galaxies over a wide range of masses (10^6–10^{11} $M_\odot$; e.g. Christensen et al. 2014; Augustin et al. 2018). This includes low-mass galaxies, which are the most numerous in the Universe (e.g. Grazian et al. 2015), but are very difficult to observe in emission (e.g. Lowenthal et al. 1995; Bouché et al. 2001; Christensen et al. 2009; York et al. 2012; Krogager et al. 2017). Not only are DLAs the largest cosmic reservoirs of H I, but also of cosmic metals up to high z (Péroux & Howk 2020). Therefore, these absorbing systems can give us great insight into the evolution and composition of galaxies and of the neutral gas in the Universe.

The population of DLAs is expected to be quite diverse in principle, due to a range of different masses, star formation histories (and therefore nucleosynthesis enrichment), and dust content (e.g. Prochaska et al. 2003; Noterdaeme et al. 2008; Christensen et al. 2014). Further, the metal content of DLAs increases across cosmic time (Prochaska & Wolfe 2002; Rafelski et al. 2012; De Cia et al. 2018), due to the production of metals by different nucleosynthetic processes. There is also growing observational evidence that the interstellar medium (ISM) in galaxies is not chemically homogeneous, for example from observations of the Milky Way (Welty et al. 2020; De Cia et al. 2021) and nearby galaxies (e.g. Sánchez Almeida et al. 2015; Wang et al. 2022).

While most studies of DLAs have focused on their global properties, variations in metal content inside individual systems have been observed in a few cases through component-by-component analysis of the absorption-line profiles (Prochaska 2003; Dessauges-Zavadsky et al. 2006; Rodríguez et al. 2006; Wiseman et al. 2017; de Ugarte Postigo et al. 2018; Noterdaeme et al. 2017; Guber et al. 2018). These gas components, which have been identified using Voigt-profile fitting techniques, relate to clouds of gas that move at different velocities. While we sometimes call them clouds, individual components may still have relatively large velocity broadening, indicating that they are probably a mix of multiple clouds. With very high resolution (e.g. $1\,\mathrm{km\,s^{-1}}$), it is possible to isolate individual gas components, such as the translucent cloud observed in the Milky Way by Welty et al. (2020). However, while there is general agreement on the properties of gas in simulations and observations along whole line-of-sight (LOS) profiles (Marra et al. 2021), on a component-by-component basis, there can be degeneracies between physical parameters such as temperature, N(H), and metallicity (Marra et al. 2022). It is therefore important to note that, when studying DLAs on a component-by-component basis, components could indeed be a mix of sub-components with different physical parameters.

In a component-by-component analysis, the total metallicity cannot be characterised because the information on the H I is normally obtained from the Lyman-alpha line, which is a broad blend of the individual components. Despite this challenge, it is still viable to obtain information regarding the metal enrichment of components by studying their dust depletion. This is the phenomenon whereby metals form dust grains and are no longer observable in the gas phase (Field 1974; Phillips et al. 1982; Jenkins et al. 1986; Savage & Sembach 1996; Jenkins 2009; De Cia et al. 2016, 2021; Roman-Duval et al. 2021). The depletions of different elements correlate with each other to varying degrees depending on how easily they form dust grains (Jenkins 2009; De Cia et al. 2016; Roman-Duval et al. 2021). It has been shown that the amount of dust in a system is indicative, to some extent, of its total metallicity (Ledoux et al. 2002a; Vladilo 2002; Noterdaeme et al. 2008; De Cia et al. 2016). Therefore, although we cannot accurately know the total metallicity of individual gas clouds in DLAs, it is still possible to study their chemical enrichment by characterising their dust depletion.

When studying chemical abundances it is also important to take into consideration possible nucleosynthetic effects that could impact observed metal abundances. Here we refer to the nucleosynthetic effects as over- or under-abundances of certain metals due to their formation processes. The α-elements (e.g. S, Si, O, Mg, Ti, Ca) tend to be more abundant in the early part of a galaxy's evolution (Tinsley 1979; McWilliam 1997) because they are formed mostly by core-collapse supernovae, and these are the first supernovae to explode (Nomoto et al. 2006). This over-abundance of α-elements decreases with time, as the metals formed mostly by Type Ia supernovae (e.g. Fe, Ni, Co, Mn) begin to contribute more to the overall metal content of the galaxy.

The observation of α-element enhancement is mostly limited to the Local Group from measurements of chemical abundances in stars, where older stellar populations with a lower metallicity have an over-abundance of α-elements and an under-abundance of Mn (Lambert 1987; McWilliam 1997; Tolstoy et al. 2009; de Boer et al. 2014). At higher redshift it is more challenging to observe α-element enhancement. In some cases it is possible to observe enhancements as signatures in the ISM of galaxies (Cullen et al. 2021) and metal-poor DLAs, where the effects of dust depletion are minimal and it is therefore more straightforward to disentangle dust depletion from nucleosynthetic effects (e.g. Dessauges-Zavadsky et al. 2002, 2006; Cooke et al. 2011; Becker et al. 2012; Ledoux et al. 2002b; De Cia et al. 2016). When gas components have a higher metallicity, however, it is important to be able to make considerations for both dust depletion and nucleosynthesis.

Thanks to observations of the galactic gas cycles, signatures of outflowing and inflowing gas from the circumgalactic medium (CGM) have been seen in the Milky Way in the form of high-velocity clouds (HVCs; e.g. Fox et al. 2019). In extragalactic studies, correlations between metallicity tracers and azimuthal angle of galaxies have been found, indicating metal-rich outflowing gas along the minor axis (e.g. Bouché et al. 2012; Péroux et al. 2020; Wendt et al. 2021). In DLAs, however, this task is more difficult without the emission counterpart of the galaxy: we do not know their morphologies. It is not straightforward to assess whether the gas in a DLA is indeed part of the ISM, or whether it is gas in the CGM. There is evidence from studies of DLA samples with galaxy emission counterparts that DLA absorption systems are built up of gas extending to the full halo of their host galaxies (e.g. Christensen et al. 2019). It is possible to use the combination of the chemical enrichment of individual gas components with their relative velocities to start investigating signatures of inflow and outflow to and from DLA galaxies.

In this work we perform a component-by-component analysis of the column densities measured from absorption-line spectra of 70 DLAs by De Cia et al. (2016). We analyse the metal and dust-depletion properties of individual gas components within DLAs over the redshift range $z_{\rm abs} = 1.7{-}4.2$ and investigate their chemical diversity and the possible effects of nucleosynthesis. We combine the chemical enrichment properties with the kinematics of individual components to investigate possible evidence for inflow and outflow of gas. We denote the relative abundances of metals X with respect to the metal Y as $[X/Y] = \log(N(X)/N(Y)) - \log(N(X)_\odot/N(Y)_\odot)$, where $\log(N(X))$ is the column density of X measured in units of $\mathrm{cm^{-2}}$, and $N(X)_\odot$ is the solar abundance of X (Asplund et al. 2021), and also using the recommendations of Lodders et al. (2009). This paper is structured as follows: in Sect. 2 we describe the methodology used to study dust-depletion; in Sect. 3 we present our results and discuss their implications; and in Sect. 4 we present our concluding remarks.

2. Methodology

We use the column density measurements of De Cia et al. (2016), who studied the abundances and relative abundances for a sample of 70 DLAs towards quasars (QSOs) at redshifts $1.7 \leq z_{\rm abs} \leq 4.2$ using data from the Very Large Telescope (VLT) and the Ultraviolet and Visual Echelle Spectrograph (UVES). The average resolution of the spectra is $R \sim 40\,000$. All DLAs have at least $\log N(\mathrm{H}) \geq 20$ to ensure overall shielding from ionising radiation. De Cia et al. (2016) studied depletion sequences for systems with $\log N(\mathrm{H}) \geq 20$, ensuring that ionisation effects do not play a significant role. However, the hydrogen column density is not available for individual clouds, and therefore we cannot ensure the criteria of $\log N(\mathrm{H}) \geq 20$. Here we make the assumption that the depletion sequences are still valid at the level of individual components because we still observe strong correlations in their depletion sequences. Figure A.1 shows that the depletion sequences for the individual components are indeed very similar to the depletion sequences of De Cia et al. (2016), with an overall larger scatter. This scatter possibly holds

information on ionisation and nucleosynthetic effects, which are important aspects of this work.

In this work we perform a component-by-component analysis of these line profiles. Individual gas components were identified by De Cia et al. (2016) through Voigt profile fitting to the spectral lines available. To avoid misidentification of individual components and the effects of blending between lines, several lines were modelled simultaneously, both transitions from the same ion and from different ions, to determine individual components. This means that we are not necessarily identifying individual separated clouds, but rather groups of clouds at similar velocities. The zero velocity is chosen to be the component with the highest Fe II column density because we assume this to be the component closest to the inner parts of the galaxy. The full data set is listed in Table F.1 of De Cia et al. (2016). From the 70 DLAs, we identified 64 DLAs with one or more components for which we could measure the level of dust depletion within an error of 0.5 dex. From this we found that there are 25 DLAs with two or more components, which we used to study the chemical diversity within systems.

2.1. Measuring dust depletion from depletion patterns

Several methods have been used in the literature to estimate the amount of dust depletion in gas clouds (e.g. Jenkins 2009; De Cia et al. 2016, 2021). The overall strength of dust depletion can be estimated from the differences in the observed column densities of metals that have different refractory properties, regardless of the H content. The analysis in this work is based on the analysis of relative abundances developed in De Cia et al. (2016), who found correlations between the relative abundances of metals and the relative abundances of zinc and iron, [Zn/Fe], also called depletion sequences. We describe below the method we use in this work.

The depletion of an element X in a system, δ_X, can be expressed as

$$\delta_X = A2_X + B2_X \times [\mathrm{Zn/Fe}]_{\mathrm{fit}}, \quad (1)$$

where $[\mathrm{Zn/Fe}]_{\mathrm{fit}}$ is the overall strength of depletion, or the depletion factor; $A2_X$ and $B2_X$ are coefficients of the depletion sequence fits in Konstantopoulou et al. (2022) and are specific for each element (see Table 1). In principle, $A2_X$ can be assumed to be zero because we expect to have no dust depletion when there is no depletion, $[\mathrm{Zn/Fe}]_{\mathrm{fit}} = 0$ (i.e. positive depletion is unphysical). In this work we make use of $[\mathrm{Zn/Fe}]_{\mathrm{fit}}$ instead of [Zn/Fe], as is used in De Cia et al. (2016), because this new quantity is derived from information of all the available metals and is therefore more solid. We show a comparison of the two procedures in Fig. B.1. $B2_X$ can be interpreted as a refractory index, which is closer to zero for elements that do not form dust grains easily (volatile elements), and further from zero for elements that are able to form dust grains more readily (refractory elements).

The total dust-corrected abundance of metal X is given by

$$[\mathrm{X/H}]_{\mathrm{tot}} = [\mathrm{X/H}] - \delta_X, \quad (2)$$

where [X/H] are the observed gas-phase abundances. Combining these equations, we obtain

$$y_i = a_i + B2_X \times [\mathrm{Zn/Fe}]_{\mathrm{fit}}, \quad (3)$$

which is a linear relation, $y_i = a_i + bx$, where

$$y_i = \log N(X) - X_\odot + 12 - A2_X, \quad (4)$$

$$a_i = [\mathrm{M/H}]_{\mathrm{tot}} + \log N(\mathrm{H}). \quad (5)$$

Table 1. Coefficients of the depletion sequences for metals X (Konstantopoulou et al. 2022).

X	$A2$	$B2$
δ_{Zn}	0.00 ± 0.01	-0.27 ± 0.03
δ_{O}	0.00 ± 0.00	-0.20 ± 0.05
δ_{P}	0.08 ± 0.05	-0.26 ± 0.08
δ_{S}	0.01 ± 0.02	-0.48 ± 0.04
δ_{Si}	-0.04 ± 0.02	-0.75 ± 0.03
δ_{Mg}	0.01 ± 0.03	-0.66 ± 0.04
δ_{Mn}	0.07 ± 0.02	-1.03 ± 0.03
δ_{Cr}	0.12 ± 0.01	-1.30 ± 0.01
δ_{Fe}	-0.01 ± 0.03	-1.26 ± 0.04

Notes. The values for P that we use here are being revised and updated in Konstantopoulou et al. (in prep.).

The value of y_i represents the amount of each metal normalised by its solar abundance. We use the notation y_i, instead of y, to highlight the difference from the notation of De Cia et al. (2021). Here y_i does not represent abundances, but rather normalised metal column densities, which can be characterised in individual gas components i. If there is no dust depletion in a system, or any additional sources of variation, y_i for each metal would be similar. If there is only dust depletion at play, we would expect the y_i values to align on a straight line with a gradient $[\mathrm{Zn/Fe}]_{\mathrm{fit}}$, which represents the overall strength of depletion. The y-intercept of this straight line, $a_i = [\mathrm{M/H}]_{\mathrm{tot}} + \log N(\mathrm{H})$, represents an 'equivalent metal column density'. This is the total amount of metals after correcting for dust depletion. Additional deviations to the straight line could be due to other processes, such as nucleosynthesis (e.g. alpha-element enhancement).

For this work we performed two sets of linear fits to the depletion patterns. In the first we fitted a straight line to all the available metals, and in the second we included only Cr, Fe, Zn, and/or P, and excluded α-elements and Mn, which we refer to as non-α elements and Mn (NAM). In both cases we require at least three constrained data points for a linear fit to the data and we do not include the upper limits in the fitting procedure. The second approach highlights any deviations due to nucleosysnthesis and ensures that these are not biasing the estimate of the dust depletion. We obtained the depletion factors $[\mathrm{Zn/Fe}]_{\mathrm{fit}}$ and equivalent metal columns $[\mathrm{M/H}]_{\mathrm{tot}} + \log N(\mathrm{H})$ from the linear fits to the depletion patterns for individual gas components within the DLAs in our sample. We used the Python package ODR to fit the lines, which uses orthogonal distance regression (ODR) and considers uncertainties on both x and y.

2.2. Deviations from depletion patterns

Deviations from the linear fits to the depletion patterns could occur for at least two possible reasons, ionisation and/or nucleosynthetic effects. Because we do not know if the H column density is sufficient to shield each individual gas cloud from ionising radiation, we could expect ions with lower ionisation potentials to be more easily ionised and fall below the linear fits to the depletion patterns. On the other hand, if all the metals were evenly ionised, there would not be any deviations from the straight line, and the depletion factor $[\mathrm{Zn/Fe}]_{\mathrm{fit}}$ would still be an accurate representation of the dust depletion in the system. We investigate the possibility of ionisation effects by comparing ionisation potential to deviation from the depletion pattern

in Sect. 3.4. If ionisation effects do occur in our sample, then we expect some correlation between ionisation potential and the amount of deviation from the depletion pattern.

Secondly, deviations from the linear fit to the depletion pattern could also be due to nucleosynthetic effects. For example, some galaxies could have an enhancement of α-elements due to the contribution of α-elements from Type II supernovae. In particular, if this is the case for some for our galaxies, we may observe over-abundances of Si, S, Mg, and O, and an under-abundance of Mn, similarly to what is observed in the Milky Way and nearby dwarf galaxies. If nucleosynthetic effects are indeed present in our data, then including these four metals in the fitting procedure could produce an inaccurate fit to the depletion patterns. In an attempt to investigate any nucleosynthetic effects, we exclude the α-elements and Mn from the depletion pattern fit. We describe deviations from the linear fit due to nucleosynthesis as the difference between the deviation of X and the deviation of Fe, $[\mathrm{X/Fe}]_{\mathrm{nucl}} = X_{\mathrm{dev}} - \mathrm{Fe}_{\mathrm{dev}}$, where the deviation is the vertical distance from the observed point to the linear fit to the depletion pattern. In other words, $[\mathrm{X/Fe}]_{\mathrm{nucl}}$ describes the relative abundances observed in the gas after correcting for dust depletion, and likely represents the product of stellar nucleosynthesis on the gas.

3. Results and discussion

3.1. Diversity of dust depletion within DLAs

In Figs. 1–4 we present the depletion patterns and their linear fits for obtaining the overall strength of dust depletion $[\mathrm{Zn/Fe}]_{\mathrm{fit}}$, and equivalent metal columns $[\mathrm{M/H}]_{\mathrm{tot}} + \log N(\mathrm{H})$ for individual components in systems towards QSO 0013−004, QSO 2116−358, QSO 2206−199, and QSO 1331+170, respectively. Figures 1 and 2 are selected to highlight chemical diversity in the level of depletion within single DLAs, while Figs. 3 and 4 highlight the deviations due to nucleosynthesis. The depletion patterns for the remaining individual systems are included in the appendix.

Figures 5a and b show the diversity in dust depletion across our DLA population when we performed the linear fits to the depletion patterns with and without the α-elements and Mn respectively. In six cases, fewer than three metals were constrained, so we did not perform a linear fit to the depletion patterns to ensure robustness of this analysis. We did not include these cases in Table E.1, and this leaves us with 64 DLAs out of the total of 70.

The system towards QSO 0013−004 has the largest range in depletion, where the least depleted component has $[\mathrm{Zn/Fe}]_{\mathrm{fit}} = 0.35 \pm 0.004$ dex, and the most depleted has $[\mathrm{Zn/Fe}]_{\mathrm{fit}} = 1.43 \pm 0.19$ dex. In Table E.1 we present the values for $[\mathrm{Zn/Fe}]_{\mathrm{fit}}$ and $[\mathrm{M/H}]_{\mathrm{tot}} + \log N(\mathrm{H})$ for each DLA, both when fitting to all available metals and when we exclude the α-elements and Mn.

We include a statistical measure of diversity within each system by performing a z-test. For each component within the system we calculate the weighted difference between the depletion and that of the reference component:

$$\sigma_{z\text{-test}} = \frac{|[\mathrm{Zn/Fe}]_{\mathrm{fit},i} - [\mathrm{Zn/Fe}]_{\mathrm{fit,ref}}|}{\sqrt{\sigma^2_{[\mathrm{Zn/Fe}]_{\mathrm{fit},i}} + \sigma^2_{[\mathrm{Zn/Fe}]_{\mathrm{fit,ref}}}}}. \quad (6)$$

We chose the reference to be the component with the minimum uncertainty on its depletion, so as to optimise the sensitivity of the z-test[1]. We plot $\sigma_{z\text{-test}}$ for each component in each system in Fig. 6. There are ten systems with $\sigma_{z\text{-test}} \geq 3\sigma$, implying statistically significant diversity in dust depletion. Specifically, these are systems towards QSO 0013−004 ($z = 1.97$), QSO 0058−292 ($z = 2.67$), QSO 0405−443 ($z = 1.91$), QSO 0528−250 ($z = 2.81$), QSO 1157+014 ($z = 1.94$), QSO 1223+178 ($z = 2.47$), QSO 1331+170 ($z = 1.78$), QSO 1444+014 ($z = 2.09$), QSO 2206−199 ($z = 1.92$), and QSO 2243−605 ($z = 2.33$). We observe diversity in dust depletion within these systems regardless of whether Si, S, Mg, O, and Mn are included in the fit to the depletion patterns. The remaining 15 DLAs seem to be chemically homogeneous within the limit of 3σ. In Sect. 3.6 we discuss further the depletion distribution of four of the systems that have statistically significant variations in depletion strength alongside their kinematics.

The depletion factor is broadly correlated with the metallicity of DLAs (e.g. Noterdaeme et al. 2008; De Cia et al. 2016), and in general the amount of dust in the ISM can be considered a tracer of metal enrichment. The relation between the dust depletion and metallicity is theoretically expected in galaxies where dust is mostly built through grain growth in the ISM (Triani et al. 2020). Thus, variations that we observe in the depletion factor in individual absorbing clouds indicate variations in the metal enrichment within distant galaxies. These results add further evidence (and at higher redshifts) that gas in galaxies can be, in general, chemically inhomogeneous, as observed in recent years in the Milky Way and other nearby galaxies (e.g. De Cia et al. 2021; Sánchez Almeida et al. 2015). This inhomogeneity could have several causes. One could be local variations in star formation within the disk of the galaxy itself. There is evidence for metallicity gradients in galaxies, out to $z \sim 3$ (e.g. Cresci et al. 2010; Patrício et al. 2019; Kreckel et al. 2019; Arellano-Córdova et al. 2020). Another could be the infall and ouflow of gas to and from the galaxy (e.g. Fox & Davé 2017; Tumlinson et al. 2017). Wendt et al. (2021) show the first chemical characterisation of the circumgalactic medium indicating dust and metal-rich outflows and dust and metal-poor infalling gas using a technique similar to the one we use in this work. Diversity of depletion could also be due to local variations in metal production, and dust production and destruction within the galaxy itself (Dessauges-Zavadsky et al. 2017; Triani et al. 2020; Slavin et al. 2020).

3.2. Including or excluding α-elements and Mn

At first we included all of the available metals in a linear fit to the depletion patterns. From these fits we often observed an over-abundance of the α-elements and an under-abundance of Mn (see Figs. 3 and 4). Therefore, nucleosynthetic effects seemed to add a level of complexity to a simple linear fit to the data. The linear fits to the depletion patterns describe only the effect of dust depletion. Excluding the α-elements and Mn from the linear fit provides a way to characterise dust depletion independently from nucleosynthetic effects by removing deviations that are not due to dust depletion. It also allows us to estimate the potential nucleosynthetic effects after having taken dust depletion into

[1] The test is sensitive to the chosen reference point. We find that the use of the maximum uncertainty produces fewer (6) components with $\sigma_{z\text{-test}} \geq 3$. One could also choose the component with the minimum (or maximum) depletion as a reference in order to maximise the difference in depletion between the minimum/maximum. However, in case the component with minimum/maximum depletion has a very large uncertainty, this choice would not capture diversity between all the other components.

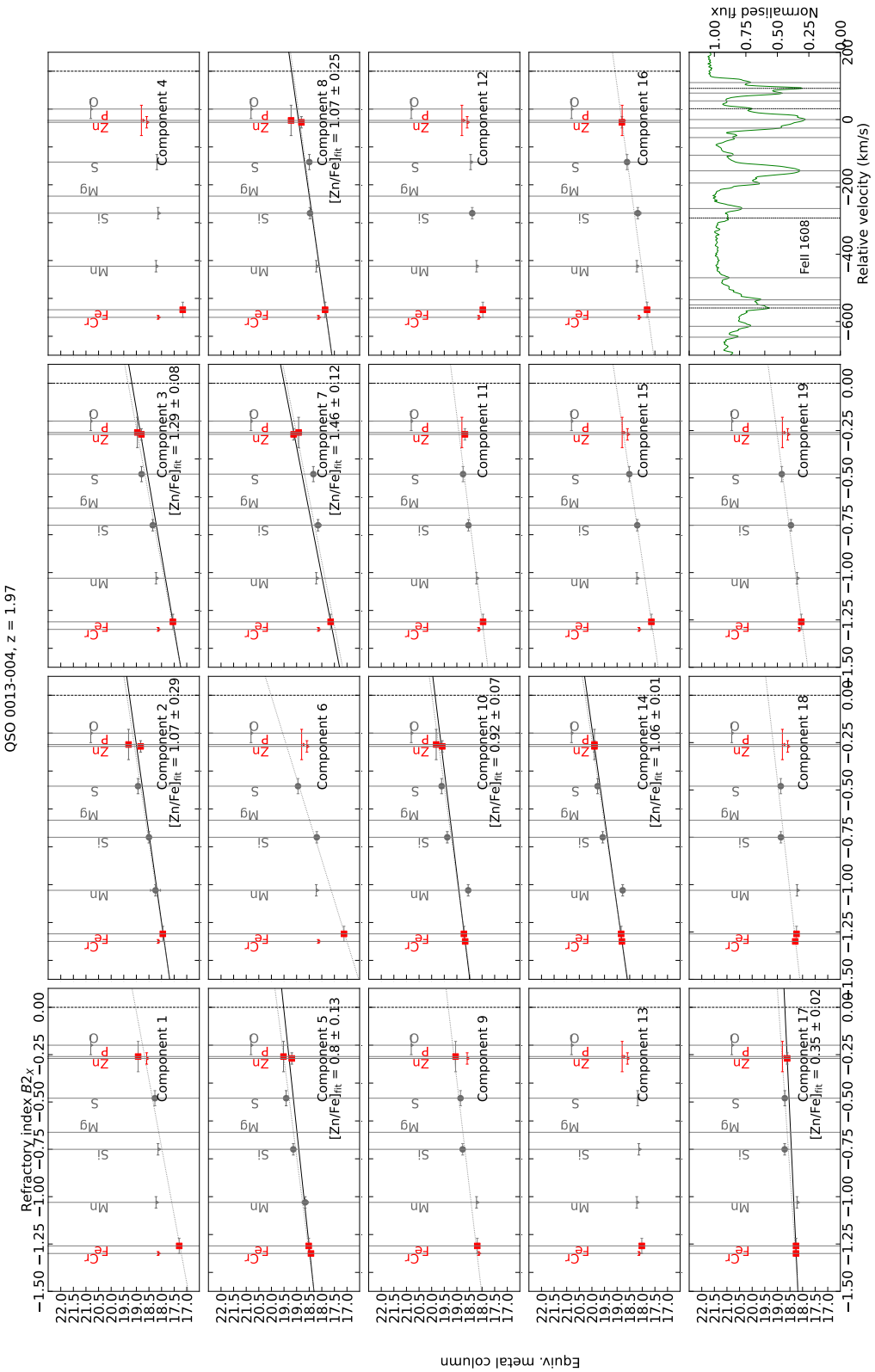

Fig. 1. The depletion pattern and fitted straight lines to DLA system QSO 0013−004 with at least 19 individual gas components. Components are numbered increasingly with increasing velocities (i.e., number one being the bluest component). Here the solid black line shows the linear fit to the depletion pattern for only the non-α elements Cr, Fe, Zn, P (in red squares). The depletion factor $[Zn/Fe]_{fit}$ is the slope of the fit. The dotted line shows the linear fit to the depletion patterns when all the available metals are included. The dashed vertical line is where $B2_X = 0$. The last panel shows the spectrum of the quasar, and indicates the positions of the individual components as determined with a Voigt-profile fitting technique. We see diversity in the depletion strengths of the components. The dashed black line shows the components in which H_2 is detected by Petitjean et al. (2002).

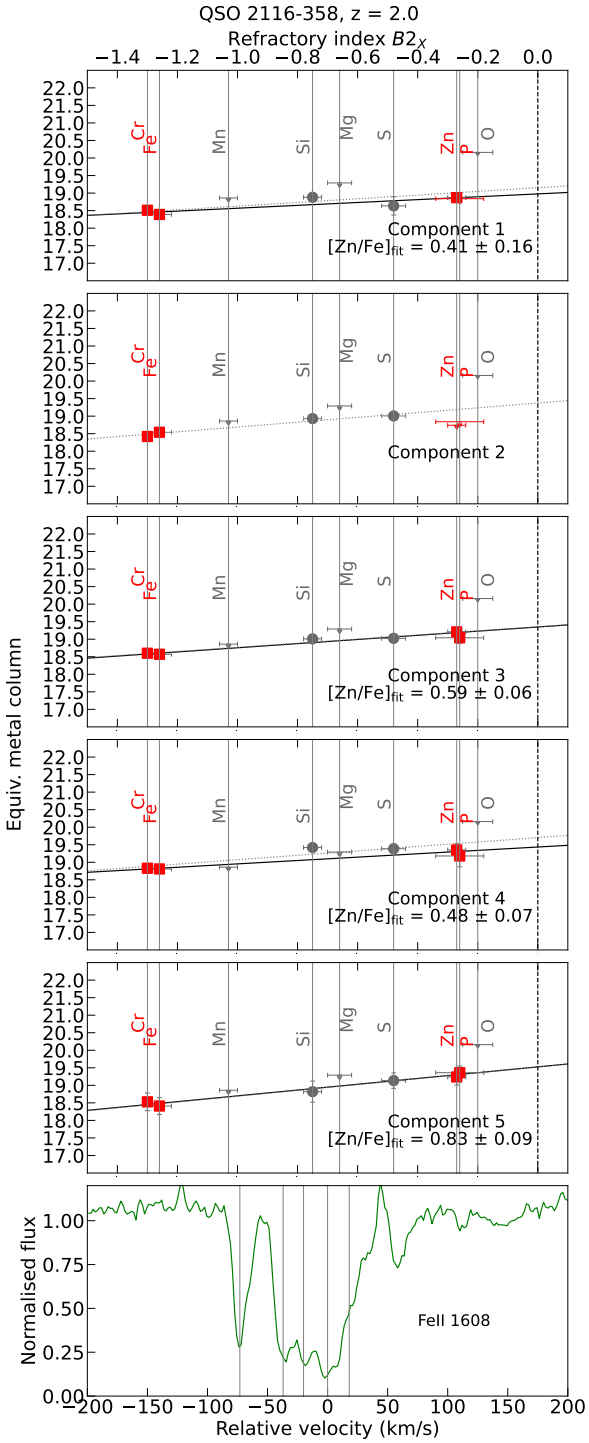

Fig. 2. Same as Fig. 1, but for QSO 2116−358. The label for relative velocity only refers to the bottom panel.

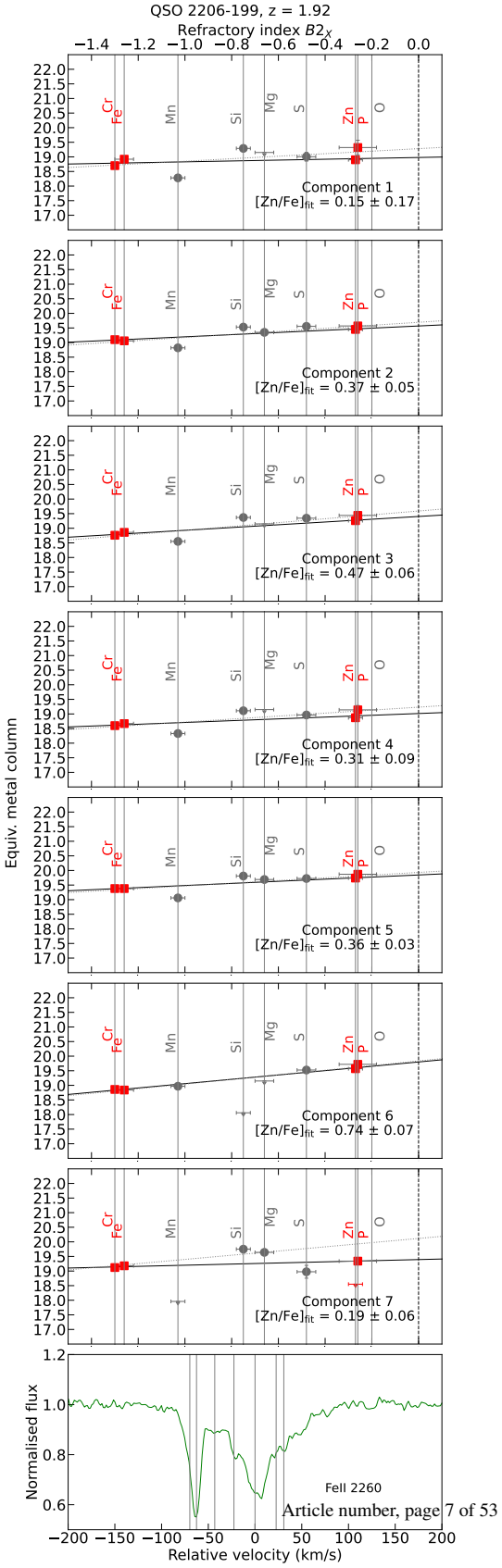

Fig. 3. Same as Fig. 1, but for QSO 2206−199. The label for relative velocity only refers to the bottom panel.

account. In general, excluding the α-elements and Mn flattens the slope of the linear fit to the depletion patterns because the α elements considered here are mainly volatile. This causes an offset towards lower column densities. In some cases slightly negative values of $[\mathrm{Zn/Fe}]_{\mathrm{fit}}$ result from the linear fit to the depletion patterns. This cannot be physically caused by depletion, but is instead due to the observational uncertainties. Thus, we limit the possible $[\mathrm{Zn/Fe}]_{\mathrm{fit}}$ values to be non-negative. Figure 7 shows the comparison between the depletion factors derived with the two methods. The two deviate significantly from a one-to-one line ($y = 0.98(\pm0.03)x + 0.09(\pm0.01)$), with $[\mathrm{Zn/Fe}]_{\mathrm{fit}}$, NAM being lower in general. This implies that the systems are on average

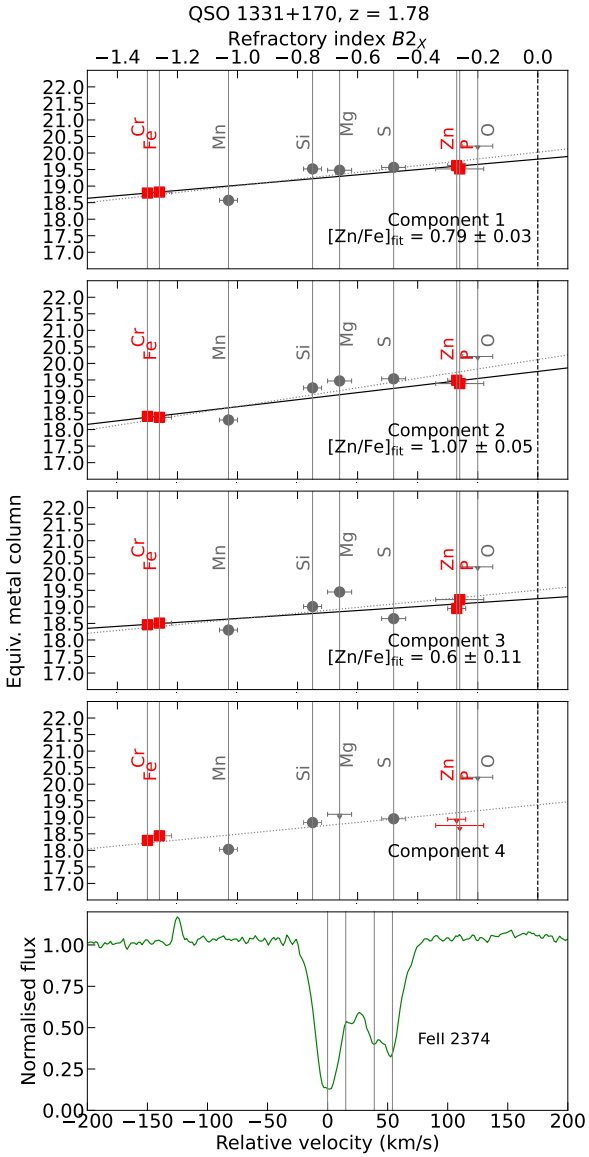

Fig. 4. Same as Fig. 1, but for QSO 1331+170. The label for relative velocity only refers to the bottom panel.

affected by nucleosynthetic differences in α-element enrichment. However, there is some scatter and some systems are indeed consistent with no α-element enhancement. There are several points that fit the $y = x$ line in Fig. 7 well. We found that these are components with either little deviation of the α-elements from the linear fit to the depletion patterns, which we interpret as not having evidence for nucleosynthesis effects, or components with few constrained data points.

Figures 5a and b show, respectively, the depletion factors for all of the gas components calculated using all the available metals and those using only Zn, Fe, Cr, and/or P.

3.3. Depletion properties across redshift

Figures 8a and b show the depletion factors for each individual component as a function of redshift using the two fitting methods. The colour bar shows the equivalent metal column densities. A particularly interesting result that we see in the figures is that there are components with little depletion at all redshifts. This could be the contribution from infalling pristine (metal-poor) gas either from gas inflows or within the galaxy itself. The colour bar highlights that low equivalent metal column densities are observed most frequently with low depletion factors, indicating either a low metallicity or an overall low amount of gas. Although there is no clear trend of increasing chemical enrichment with decreasing redshift, we do observe the most depleted components more frequently at lower redshifts. We also see that the upper bound limit of depletion in general decreases with increasing z, which is an indication of evolution of dust depletion with redshift. These results are consistent with observations of decreasing metallicity with increasing redshift (Rafelski et al. 2012; De Cia et al. 2018; Péroux & Howk 2020). Overall, there are two effects that result in the differences between Figs. 8a and b. First, Fig. 8a includes more components than 8b because in some components it was not possible to perform a NAM fit due to a lack of data. Secondly, omitting alpha elements from the linear fits to the depletion patterns, which are over-abundant and mainly volatile in this data set, causes an offset towards lower metal columns. Fitting without the alpha elements and Mn causes the slope to decrease, but there is no clear trend for the y-intercept (i.e. the equivalent metal column density). In 55 out of 96 cases (57%) the y-intercept decreases, while in 41 of 96 cases (43%) it increases.

3.4. Ionisation effects

Metal abundances in DLAs are not strongly affected by ionisation (e.g. Vladilo et al. 2001). However, the individual components studied in this work could be clouds or groups of clouds at lower columns densities than DLAs, where ionisation may play a non-negligible role. To identify any potential effects of ionisation, we plotted the ionisation potential of each metal against their residual from the abundance pattern. If the gas clouds are indeed affected by ionising radiation, we expect a correlation in these plots: metals with a low ionisation potential should deviate more from the linear fits to the depletion pattern than the metals that require more ionisation energy. Figure 9 shows that this is not the case. Although this is not final evidence that the gas clouds are not significantly affected by ionisation, the lack of correlation is enough to rule out any major ionisation effects.

3.5. α-element enhancement and Mn under-abundance

Evidence for nucleosythesis effects are apparent from the observation of systematic over-abundances of S, Si, Mg, and O and an under-abundance of Mn in several systems, such as in Figs. 3 and 4. The deviations from the linear fit to the depletion patterns are even more pronounced after excluding the α-elements and Mn from the depletion pattern fit, because it separates the possible nucleosynthetic effects from dust depletion. In Fig. 10 we present $[X/Fe]_{nucl}$ as a function of $[Zn/Fe]_{fit}$ for individual components for each of S, Si, O, Mn, and Mg. Assuming a linear conversion between $[Zn/Fe]_{fit}$ and metallicity (De Cia et al. 2016), we derive the $[X/Fe]_{nucl}$ distribution as a function of metallicity. We can then compare this directly with stellar metallicity measurements. We observe an over-abundance of the α-elements and under-abundance of Mn at low levels of dust depletion, which begins to level out at higher levels of depletion, and thus higher levels of chemical enrichment. This result is similar to studies of stellar abundances in the Milky Way and nearby dwarf galaxies (e.g. Lambert 1987; McWilliam 1997; Tolstoy et al. 2009; de Boer et al. 2014).

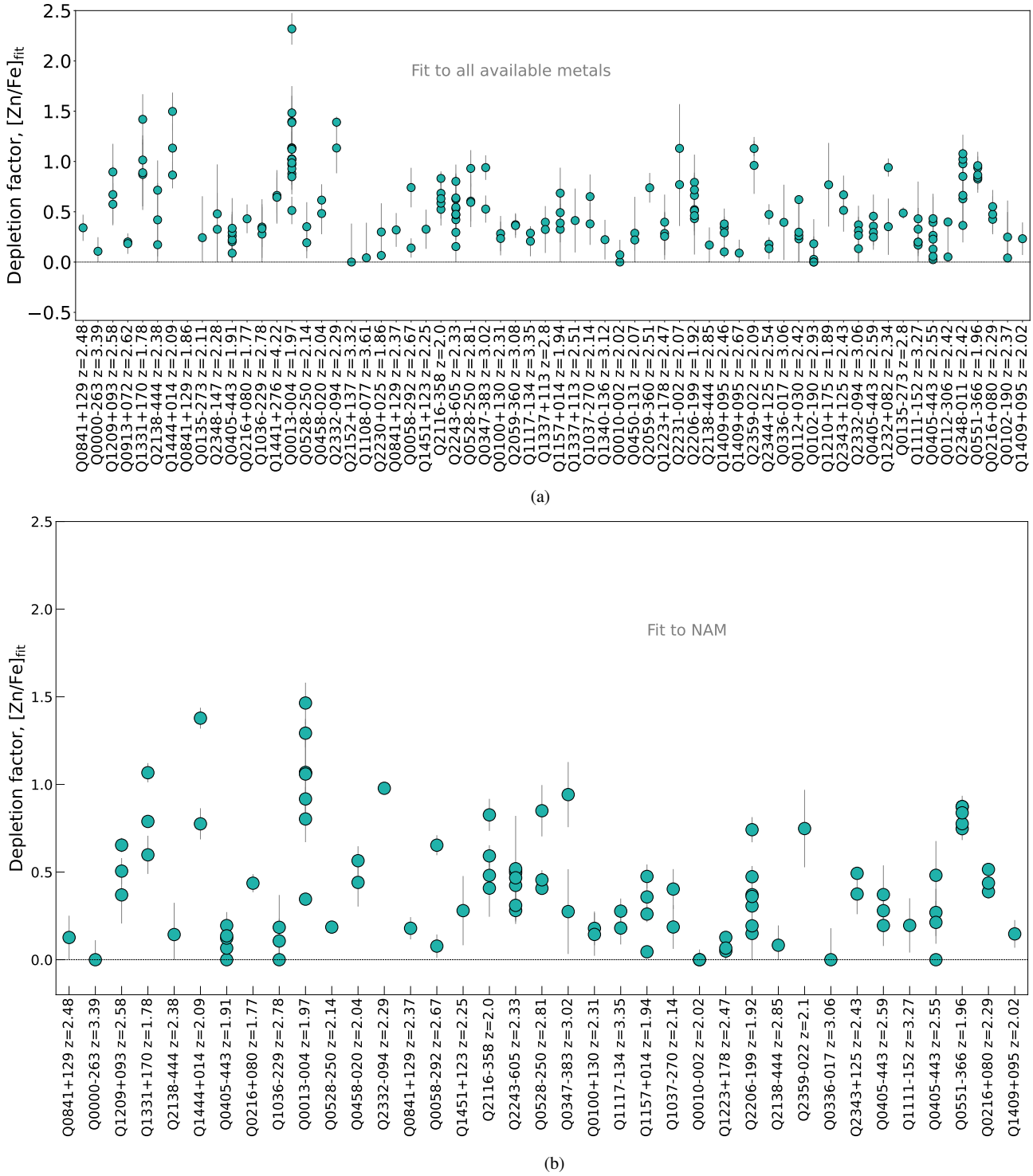

Fig. 5. The range of dust depletion strength $[Zn/Fe]_{fit}$ within each DLA system. In the top panel, the depletion factor was calculated by fitting to the depletion patterns for all available metals. In the bottom panel, the depletion factor was calculated by fitting to the non-α elements and Mn (NAM). (*a*) Depletion strengths calculated with a linear fit to all available metals. (*b*) Depletion strengths calculated with a linear fit to the depletion patterns, excluding α-elements and Mn (NAM).

The enhancement of alpha elements is somewhat more pronounced for Mg and possibly O, which have a lower ionisation potential (Fig. 9). This effect, if real, has not been fully explained. Ionisation of the dominant species in the warm neutral medium would cause the contrary effect because ions with a lower ionisation potential would be more easily ionised.

The position of the knee in the distribution of the α-element enhancement with the metallicity (hereafter the α-element knee) depends on the star formation history (SFH) of a galaxy and its efficiency in producing metals (e.g. Tinsley 1979; McWilliam 1997). From measurements of nearby dwarfs, it has been observationally shown that the α-element knee varies with stellar mass

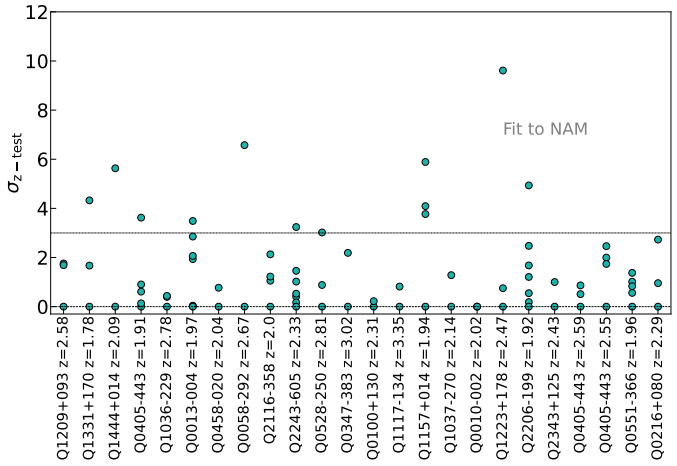

Fig. 6. Statistical significance of diversity in $[\mathrm{Zn/Fe}]_{\mathrm{fit}}$ within DLAs using the z-test: $\sigma_{z\text{-test}} = \left|[\mathrm{Zn/Fe}]_{\mathrm{fit},i} - [\mathrm{Zn/Fe}]_{\mathrm{fit,ref}}\right| \Big/ \sqrt{\sigma^2_{[\mathrm{Zn/Fe}]_{\mathrm{fit},i}} + \sigma^2_{[\mathrm{Zn/Fe}]_{\mathrm{fit,ref}}}}$, where we choose the reference component $[\mathrm{Zn/Fe}]_{\mathrm{fit,ref}}$ to be the one with the minimum uncertainty on its depletion. Here, the linear fits to the depletion patterns exclude the α-elements and Mn (NAM). QSO 0013−004 has an additional point at sigma ~55, which is not shown here for clarity.

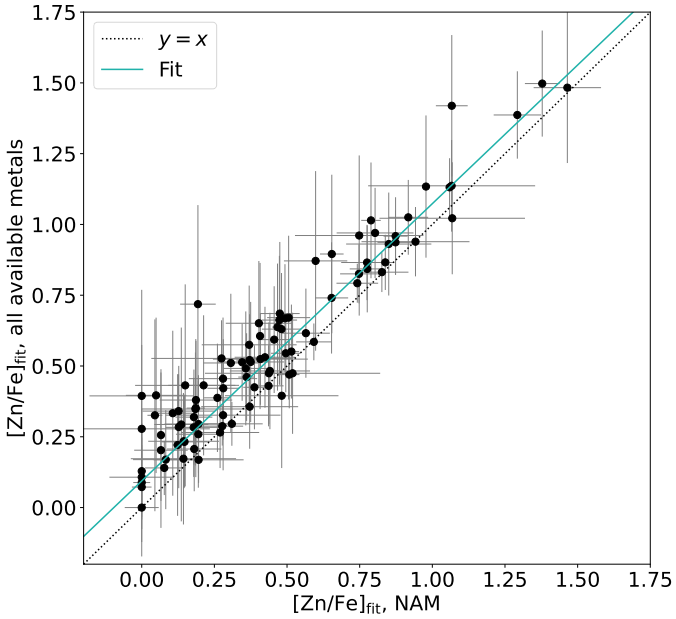

Fig. 7. $[\mathrm{Zn/Fe}]_{\mathrm{fit}}$ values calculated from fitting a straight line to the depletion patterns. The x-axis has $[\mathrm{Zn/Fe}]_{\mathrm{fit}}$ where we exclude the α-elements and Mn (NAM) in the fitting process. The y-axis has $[\mathrm{Zn/Fe}]_{\mathrm{fit}}$ derived using all the available metals in the fit. Fitting a straight line to these two values for $[\mathrm{Zn/Fe}]_{\mathrm{fit}}$ gives $y = 0.98(\pm0.03)x + 0.09(\pm0.01)$. This is different from the $y = x$ line, which implies that including or excluding the α-elements and Mn does notably affect the dust depletion factor that we calculate.

(de Boer et al. 2014). The amplitude of the plateau depends on the initial mass function (IMF) because if there are more massive stars then there are more core-collapse supernovae, and therefore more α-elements. In Fig. 10 we include stellar nucleosynthesis curves observed for the Milky Way and two satellite galaxies, Fornax and Sagittarius, from de Boer et al. (2014).

There is some debate about whether we can assume that Zn and Fe follow each other nucleosynthetically because of the complex origin of Zn (e.g. Skúladóttir et al. 2017). The stellar nucleosynthesis of Zn and Fe follow each other, to a first approximation, within the metallicity range $-2 \leq [\mathrm{Fe/H}] \leq 0$, which is most relevant for DLAs. Thus, to a first approximation, [Zn/Fe] is a solid tracer of dust content. More details are discussed in De Cia (2018).

There is a large scatter in Fig. 10, and our data points do not closely follow the lines for the Milky Way and local dwarf galaxies. However, it should be noted that these assumed curves are based on stellar observations, also with broad scatter. Moreover, DLAs (and their sub-components) represent a heterogeneous mix of galaxies with different masses and SFHs. Nevertheless, α-element enhancements and Mn under-abundance in DLAs are evident in Fig. 10.

Alpha-element enhancements have been conclusively observed for systems with depletion levels close to zero (e.g. Dessauges-Zavadsky et al. 2006; Cooke et al. 2011; Becker et al. 2012; Ledoux et al. 2002b; De Cia et al. 2016) or systems with $[\mathrm{Zn/Fe}] \sim 0.5$ (Konstantopoulou et al. 2022). For systems with $[\mathrm{Zn/Fe}] > 0.5$ it has been difficult to disentangle dust depletion from nucleosynthetic effects. Here we were able to perform this disentanglement, and we show that some DLA sub-components with higher metal enrichment (depletion, and possibly metallicity) have α-element enhancements.

We show that their extent is not dissimilar to what we observe in local galaxies, and so, although there is indeed scatter in our plot, this seems to be a common feature in α-element enhancement observed in stellar spectra (de Boer et al. 2014; Tolstoy et al. 2009). Nevertheless, our points do cluster around the lines and, despite the uncertainties, the observations of the α-element enhancement in DLAs seem to be consistent with the plateau observed in the Milky Way and local galaxies. In general, the α-element plateau is influenced by the IMF (e.g. Tinsley 1979). The location of the α-element knee cannot be further constrained with the current sample, especially since it represents a mixed-bag of galaxies and their sub-components. Nevertheless, our observations are the first hints of the distribution of the α-element enhancement with metallicity in distant galaxies.

It could be argued that these nucleosynthetic effects would exist by construction of the method because our data are a subset of the total column densities from De Cia et al. (2016), which were used to derive the coefficients $A2_X$ and $B2_X$ and made an assumption on the α-element enhancement. These coefficients are in turn used to derive y_i in this work. However, there are several reasons why we do not believe this is a concern. Firstly, the individual components can be considered as independent from the data set used by De Cia et al. (2016), who consider only integrated column densities. Secondly, although Konstantopoulou et al. (2022) found small values for $A2_X$, we argue that, in principle, we can assume a value of 0 for $A2_X$ because a positive depletion is non-physical. This is indeed consistent with the uncertainties on $A2_X$, with the exception of Cr. This would remove the dependence of y_i on $A2_X$.

3.6. Kinematics of individual gas components

We search for potential evidence of infalling and outflowing gas by comparing relative velocities of individual components and their level of depletion. In Figs. 11–14 we show the $[\mathrm{Zn/Fe}]_{\mathrm{fit}}$ distribution with the velocity of each component in the left panel and their z-test in the right panel for systems towards QSO 0013−004, QSO 0405−443, QSO 0528−250 and QSO 1157+014, respectively. These four systems show statistically significant chemical diversity (i.e. with $\sigma_{z\text{-test}} \geq 3$, as

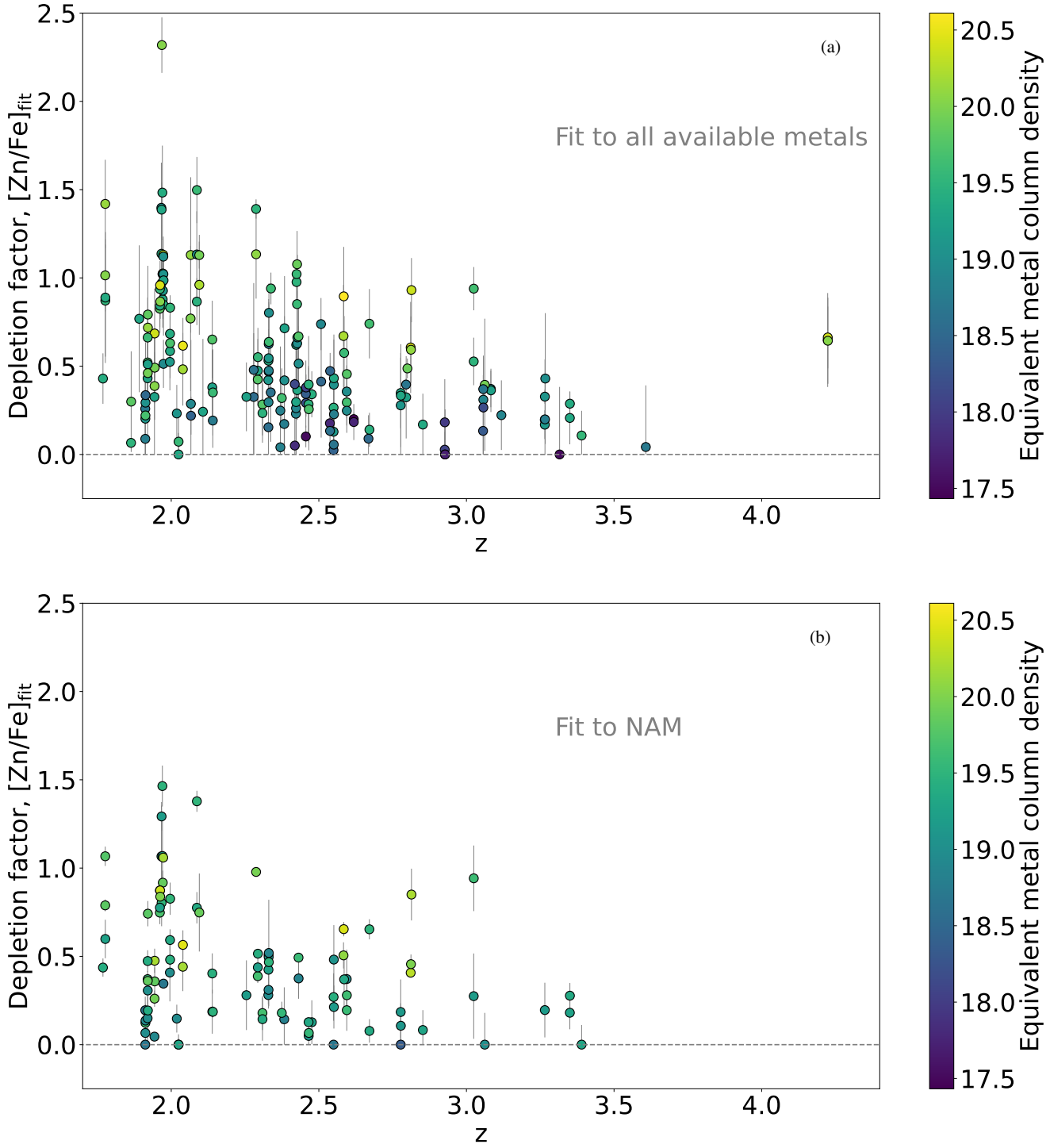

Fig. 8. Depletion factors as a function of redshift. The colour bar represents the equivalent metal column densities ($[M/H]_{TOT} + \log N(H)$). In the top panel, the depletion factor was calculated by fitting to the depletion patterns for all available metals. In the bottom panel, the depletion factor was calculated by fitting to the non-α elements and Mn (NAM). (*a*) Depletion factors in individual components as a function of redshift. Here, the depletion factors were calculated by fitting a straight line to all the available metals in the depletion patterns.(*b*) Depletion factors as a function of redshift, calculated from linear fits to the depletion patterns excluding the α-elements and Mn (NAM).

discussed in Sect. 3.1), and show some diversity in the kinematic properties. Similar plots for the other systems are included in the appendix. For most systems, the velocities of the components are between −100 and 100 km s^{-1}. An exception is the system towards QSO 0013−004, which is shown in Fig. 11, where we see components with both high blue-shifted velocities and high depletion. We discuss this system further in Sect. 3.6.2.

The system towards QSO 0528−250 (Fig. 13) also has a component with velocity ∼200 km s^{-1}, but with high depletion, which could be related to outflows. This system has a detected galaxy counterpart (Møller & Warren 1993), which allows for more detailed studies. In an in-depth study of this system, Balashev et al. (2020) find that this system is likely at a physical distance of 150−200 kpc away from the quasar. This makes

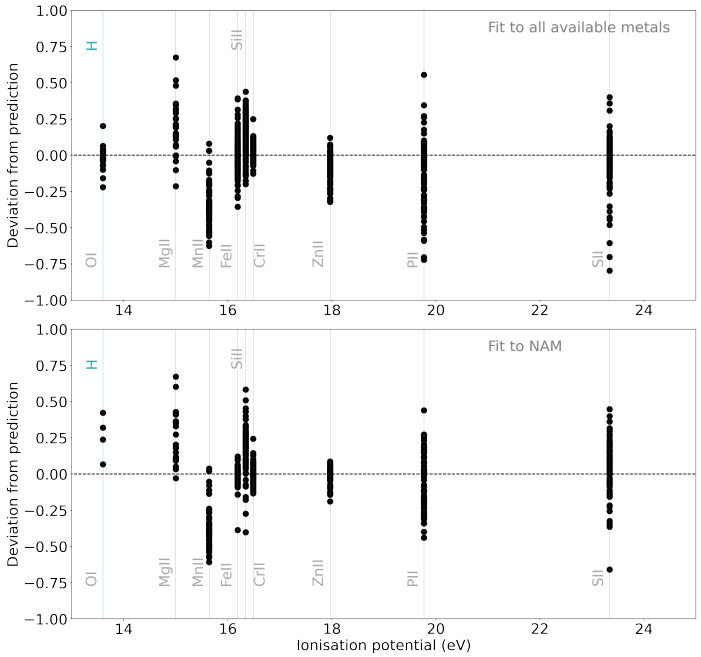

Fig. 9. Ionisation potential against the residuals, including and excluding the α-elements and Mn (NAM) respectively. We do not see a clear correlation between deviation from the fit to the depletion patterns and the ionisation potential. Although this is not concrete evidence that ionisation is completely negligible, it is enough to rule out any major ionisation effects.

it more likely that the metal-rich DLA sub-component is associated with a companion galaxy, rather than with a metal-rich outflow. In this work we find a statistically significant variation in depletion strength, with $\sigma_{z\text{-test}} \sim 3$ for component 3. This result supports that of Balashev et al. (2020).

Our observations could also probe the accretion of metal-poor gas, for example the system towards QSO 2243−605 in Fig. 15. Bouché et al. (2013) found evidence for infalling gas in UVES spectra of this QSO–galaxy pair, where the infalling components are blue-shifted ~ -150 to $-100\,\mathrm{km\,s^{-1}}$ with respect to the galaxy counterpart observed in emission. In their work they measure a component with lower depletion and lower metallicity (using Si II as a proxy for the H I column density at the level of individual components) compared to the strongest component (component 6 compared to component 9 in Fig. 15), which they attribute to infalling gas onto the galaxy. In our work we do not see large diversity in the depletion between these two components. We do, however, see statistically significant diversity for the outermost component (component 1).

In Fig. 16 we show the distribution of the absolute values of the velocities of the individual components. We make a distinction between zero-depletion components and low- and high-depletion components at a $[\mathrm{Zn/Fe}]_{\mathrm{fit}}$ value of 0.25. In these figures we see different distributions for the low- versus high-depletion groups. Interestingly, the low-depletion components have velocities below $100\,\mathrm{km\,s^{-1}}$, while the high-depletion components show a wider distribution of velocities up to $\sim 600\,\mathrm{km\,s^{-1}}$. It is possible that some of the components with high depletion are associated with metal-rich outflowing gas that is being ejected from the galaxy due to star formation. On the other hand, some of the components with low dust depletion could be consistent with infalling gas, with typically lower infalling velocities. The dust-free components are

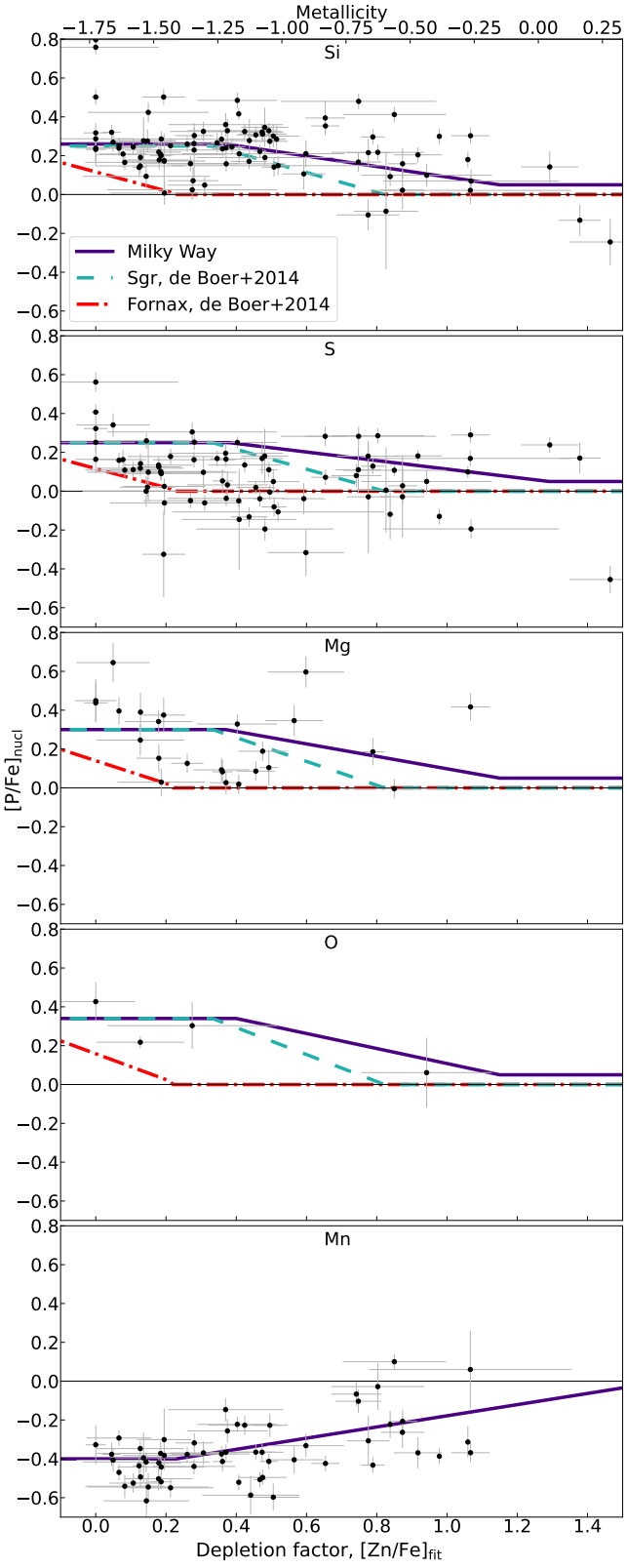

Fig. 10. $[\mathrm{X/Fe}]_{\mathrm{nucl}}$ plotted against the depletion factor. Here, we excluded the α-elements and Mn from the depletion pattern fitting to reduce potential nucleosynthesis bias. The assumed nucleosynthetic under- and over-abundance in units of the depletion factor $[\mathrm{Zn/Fe}]_{\mathrm{fit}}$ from Fig. 7 of De Cia et al. (2016) is shown in the solid purple line. We also include nucleosynthesis over-abundances for local dwarf galaxies, Fornax, and Sgr from de Boer et al. (2014). Here we only include points for which the absolute value of the error on $[\mathrm{X/Fe}]_{\mathrm{nucl}}$ is less than 0.5.

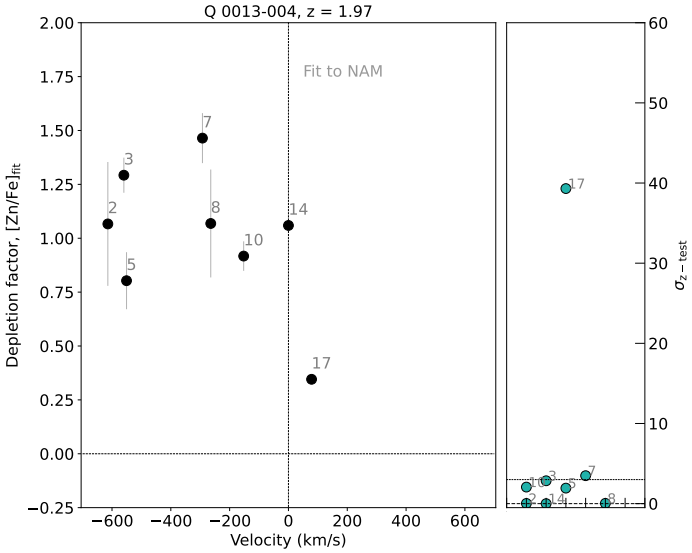

Fig. 11. The velocity of individual components within DLA system QSO 0013−004 against their depletion strengths. The depletion factor is derived from a fit to the non-α elements and Mn (NAM) in the depletion patterns. The component with the highest Fe column density was chosen as the zero-velocity point, because this is likely the component closest to the inner parts of the galaxy. This system has the highest number of components in our sample, and the highest velocities. Each component is numbered.

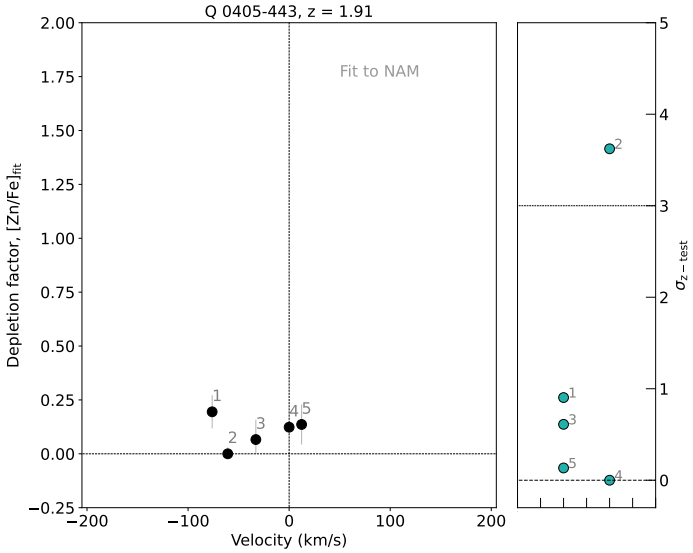

Fig. 12. Same as Fig. 11 but for DLA system QSO 0405−443.

not exclusively the components with the highest column density, which are likely the innermost parts of the galaxy (at 0 km s^{-1}), and the distribution is largely flat. This is consistent with evidence for pockets of dust-free gas within galaxies. We note that these conclusions were drawn loosely because we do not have a statistically significant representation for low-, high-, and zero-depletion components.

Further studies can be done on the systems towards QSO 0458−020 and QSO 0528−250 because they have confirmed galaxy counterparts (Møller & Christensen 2020). However, without knowing the morphologies for most of the host galaxies in our DLA sample, it is not straightforward for us to interpret the DLA kinematics, and the values to be expected are highly dependent on the geometry of the system.

3.6.1. Proximate DLAs

There are four DLAs in our sample for which the redshift difference between the quasar and the DLA corresponds to a velocity difference smaller than 5000 km s^{-1}: $v_{\rm diff} = c|z_{\rm em} - z_{\rm abs}|/(1 + z_{\rm abs}) \leq 5000\,{\rm km\,s^{-1}}$. These are the systems towards QSO 0528−250 ($v_{\rm diff} = 3225\,{\rm km\,s^{-1}}$), QSO 0841+129 ($v_{\rm diff} = 2070\,{\rm km\,s^{-1}}$), QSO 1157+014 ($v_{\rm diff} = 4684\,{\rm km\,s^{-1}}$), and QSO 2059−360 ($v_{\rm diff} = 514\,{\rm km\,s^{-1}}$), and are called proximate DLAs (PDLAs).

There are several possible scenarios we can use to interpret the depletion-kinematics relationship. The first scenario is to assume that the absorbing galaxy is the QSO host itself. In this case, the interpretation of the geometry of the absorbing gas should be easier because we are necessarily on the closest side of the absorbing galaxy. We could naively expect inflowing gas clouds to be red-shifted and outflows blue-shifted. We could also expect outflowing gas to be more metal rich and inflowing gas to be more metal poor. We checked for a trend among these PDLAs to see if they differ from the sample. For QSO 0528−250 (Fig. 13) and QSO 1157+014 (Fig. 14) we see instead components with higher depletion being red-shifted compared to low-depletion components, which is counter-intuitive in this scenario. We are not able to perform this analysis for the remaining two PDLAs because there are too few absorbing components to make such a comparison. In comparing the kinematics-depletion trend for QSO 0528−250 and QSO 1157+014 to the overall sample, we see a similar trend in the systems towards QSO 0216+080 (Fig. D.4), QSO 0347−383 (Fig. D.5) and QSO 2116−358 (Fig. D.17), although with less significant variations in the dust depletion ($z_{\rm test} < 3\sigma$). We see this trend in 2/2 of the PDLAs, and in 3/12 of the standard DLAs (for systems with three or more components). This interpretation is based on a very small sample, and the system towards QSO 0528−250 is a special case, as we explain below.

Since a velocity limit of 5000 km s^{-1} does not ensure that the absorbing galaxy is indeed the QSO host, another scenario is that the DLA may be a nearby companion galaxy to the QSO. QSO 0528−250 is shown to be part of a small galaxy group, and the absorber is likely to not be associated with the QSO, which makes this scenario more likely for this system (Møller & Warren 1993; Prochaska & Wolfe 1997; Srianand & Petitjean 1998; Ledoux et al. 1998; Balashev et al. 2020). Further, $z_{\rm abs} > z_{\rm em}$ for this DLA, which makes it particularly interesting, although the QSO redshift may have been underestimated. In this interpretation, it could be that the red-shifted, highly depleted components are metal-rich outflows from the far side of the companion galaxy.

However, relative velocities of gas clouds are not robust indicators of their physical locations. For example, gas clouds on either side of a galaxy can produce red-shifted velocities due to the motion of the galaxy with respect to the QSO. In theory, it is possible to have a combination of the two scenarios described above that could produce red-shifted highly depleted components. In this case, part of the absorption could be located within the QSO and part of it could be in a different galaxy with a peculiar velocity towards the QSO. In velocity space, the absorption lines of these two parts could coincide by chance. It is therefore difficult to make any conclusive remarks about the relationship between kinematics, as interpreted in velocity space, and depletion of individual gas components.

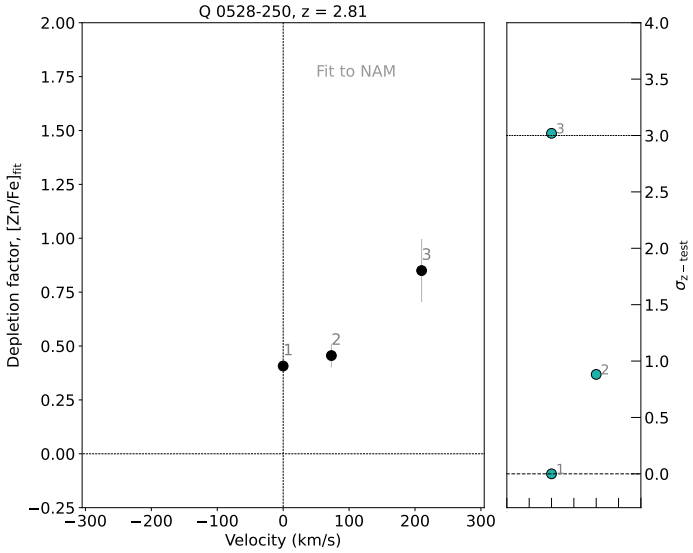

Fig. 13. Same as Fig. 11 but for DLA system towards QSO 0528−250. This system is a proximate DLA, where the redshift difference between the quasar and the DLA corresponds to a velocity difference smaller than 5000 km s^{-1}, i.e. $c|z\mathrm{em} - z\mathrm{abs}|/(1 + z\mathrm{abs})$. Here we see a relatively high-velocity red-shifted component with high depletion (component 3).

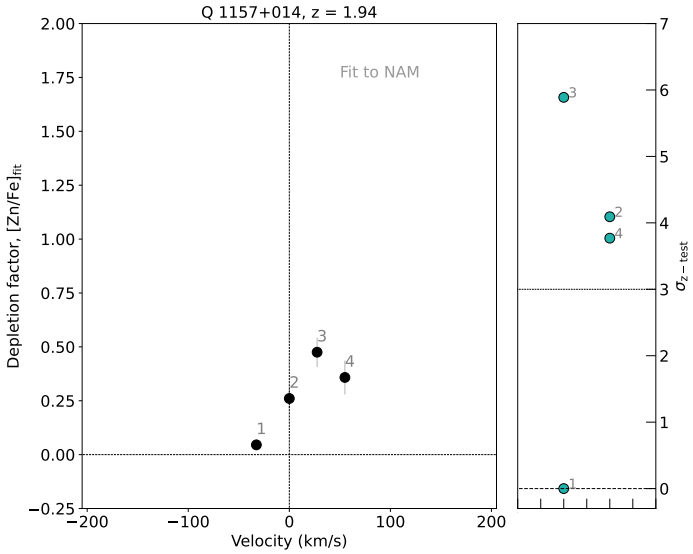

Fig. 14. Same as Fig. 11 but for DLA system QSO 1157+014. This system is a proximate DLA.

3.6.2. QSO 0013–004

This system has many components (see Fig. 1), some with high velocities (up to −600 km s^{-1}) and high depletion strengths (mostly between 0.75 and 1.5 dex). It has also been studied in the literature (e.g. Petitjean et al. 2002; Ledoux et al. 2002b; Rodríguez et al. 2006; Noterdaeme et al. 2021). Given its relatively high metallicity for a DLA, this system is likely to be associated with a relatively massive galaxy according to the mass–metallicity relation in DLAs (Christensen et al. 2014), possibly of the order of $M_* \sim 10^{10}\,M_\odot$. Furthermore, the system is an outlier from the velocity–metallicity relation of Ledoux et al. (2006): it seems to have a higher velocity width of their low-ionisation absorption-line profiles, $\Delta V = 720$ km s^{-1}, for its

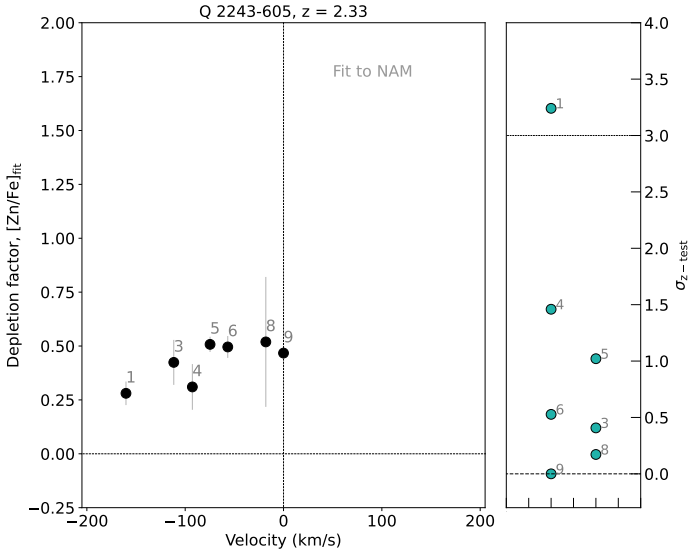

Fig. 15. Same as Fig. 11 but for DLA system QSO 2243−605. This system shows a general trend of the depletion decreasing with blue-shifted velocities.

metallicity, [M/H] = −0.4 ± 0.1 (De Cia et al. 2016). In a detailed study, Petitjean et al. (2002) found that at least four of the components have H_2 absorption, which they attribute to intense star formation activity in the regions around the absorbing system (components 2, 6, 14, and 17 in this paper). In their paper they postulate that the system is composed of two main sub-systems centred at 0 and −480 km s^{-1}. From this work we calculate that the first sub-component would have an average $[\mathrm{Zn/Fe}]_{\mathrm{fit}}$ of 1.03 ± 0.21 and the second an average of 0.96 ± 0.21, which are very similar. This is the only system that contributes to the very high velocities (∼600 km s^{-1}) in the top and bottom panels of Fig. 16. However, if this is indeed two sub-systems, the system centred at 480 km s^{-1} would fall right on top of the other system centred at 0 km s^{-1} in the cumulative distribution if we were to split the systems. This could be motivation for QSO 0013−004 being a set of two sub-systems, as postulated by Petitjean et al. (2002), instead of out-flowing gas. This system shows α-element enhancement and Mn under-abundance in several components, as shown in Fig. 17. This may also indicate some recent star formation in the system. Intriguingly, the distribution of the α-element enhancement for this system follows closely the curve for the Milky Way. Furthermore, we compare the velocities, depletion, and the α-element enhancement by looking at Figs. 1, 11, and 17 simultaneously. For example, component 17 has the lowest chemical enrichment, but a large α-element enhancement. This may suggest that this gas component could be associated with a more metal-poor part of the galaxy or a satellite galaxy, and could possibly have recent star formation. Our observation suggests that this gas is not well-mixed or homogeneously distributed.

3.7. Dust-to-metal ratio

The dust-to-metal ratio can be defined as the fraction of a metal that is in the dust phase, and can be written in terms of number of atoms as

$$\mathrm{d}tm_{\mathrm{Fe}} = \frac{N(\mathrm{Fe})_{\mathrm{dust}}}{N(\mathrm{Fe})_{\mathrm{tot}}} = 1 - 10^{\delta_{\mathrm{Fe}}}, \quad (7)$$

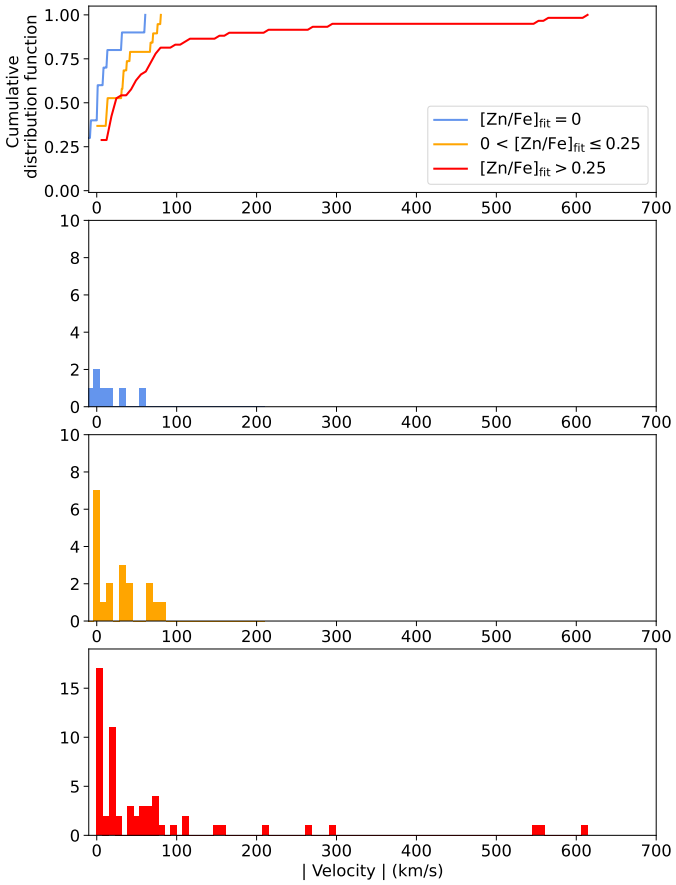

Fig. 16. Absolute value velocity distribution for all components. Here we make a distinction between zero depletion, and low- and higher-depletion components at a $[Zn/Fe]_{fit}$ value of 0.25. The top panel shows the cumulative distributions for all three distribution. The following three panels show histograms for zero, low- and high-depletion components respectively. We see a similar distribution for the proximate DLAs.

$$\mathrm{DTM_{Fe}} = \frac{\mathrm{d}tm_{\mathrm{Fe}}}{\mathrm{d}tm_{\mathrm{Gal}}}, \tag{8}$$

where DTM is the selective dust-to-metal ratio, based on Fe, normalised by the value for the Milky Way $\mathrm{d}tm_{\mathrm{Gal}} = 0.98$ (De Cia et al. 2016), and δ_X is the depletion of element X, as defined in Eq. (1). We adopt $\delta_{\mathrm{Fe}} = A2_{\mathrm{Fe}} + B2_{\mathrm{Fe}} \times [\mathrm{Zn/Fe}]_{\mathrm{fit}} = -0.01 + (-1.26) \times [\mathrm{Zn/Fe}]_{\mathrm{fit}}$ (De Cia et al. 2016). These values of DTM are not absolute mass ratios, so they are not directly comparable to those of Konstantopoulou et al. (2022). The DTM is plotted for each individual component in the DLAs in Figs. 18 and 19[2]. Notably, we see DTM values that are similar to the Galactic value in several DLAs. The diversity of depletion strengths within DLAs is also reflected in the range of values we obtain for the DTM although the uncertainty is large.

[2] For some systems, there are a different number of components in the NAM fit compared to the fit with all available metals. This is because we neglect points where the observational uncertainties are too large, i.e. for which the absolute value of the error on the DTM calculation is greater than 0.5. This is the case for the system towards QSO 1444+014, for example.

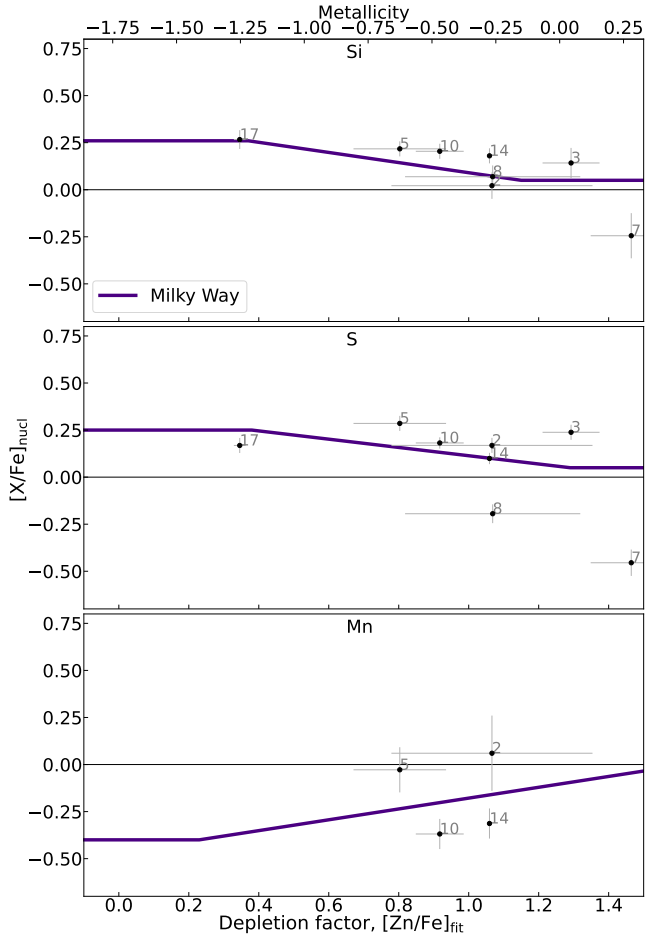

Fig. 17. The same as Fig. 10, but only for the DLA system towards QSO 0013−004.

4. Summary and conclusions

We performed a component-by-component analysis of the relative abundances of different metals in the ISM–CGM of a sample of 64 DLAs in the redshift range 1.7−4.2. Below we summarise the main results from this work.

1. Our results show that chemical enrichment, as traced by dust depletion ($[Zn/Fe]_{fit}$), is diverse within DLAs. We see ten systems with statistically significant diversity ($\geq 3\sigma_{z\text{-test}}$). This indicates that these distant galaxies are chemically diverse. This diversity is also reflected in the DTM values that we derive from the depletion.
2. There are components with very low depletion at all redshifts, including DLAs at $z \sim 2$, albeit with large uncertainties. This suggests the presence of dust-poor gas, likely with low metallicity, potentially falling onto and contributing to the build-up of DLA galaxies.
3. We performed a check on the effect of ionisation as a potential cause for deviations from the linear fit to the depletion patterns, and can exclude strong ionisation effects.
4. Our measurements reveal an over-abundance of α-elements (Si, S, O, and Mg), and an under-abundance of Mn in some gas clouds in our DLA sample, to a level very similar to that of the Milky Way and local dwarf galaxies. We interpret this as an effect of SNe nucleosynthesis. These are the first observations of the distribution of α-elements with chemical enrichment in the gas for distant galaxies.

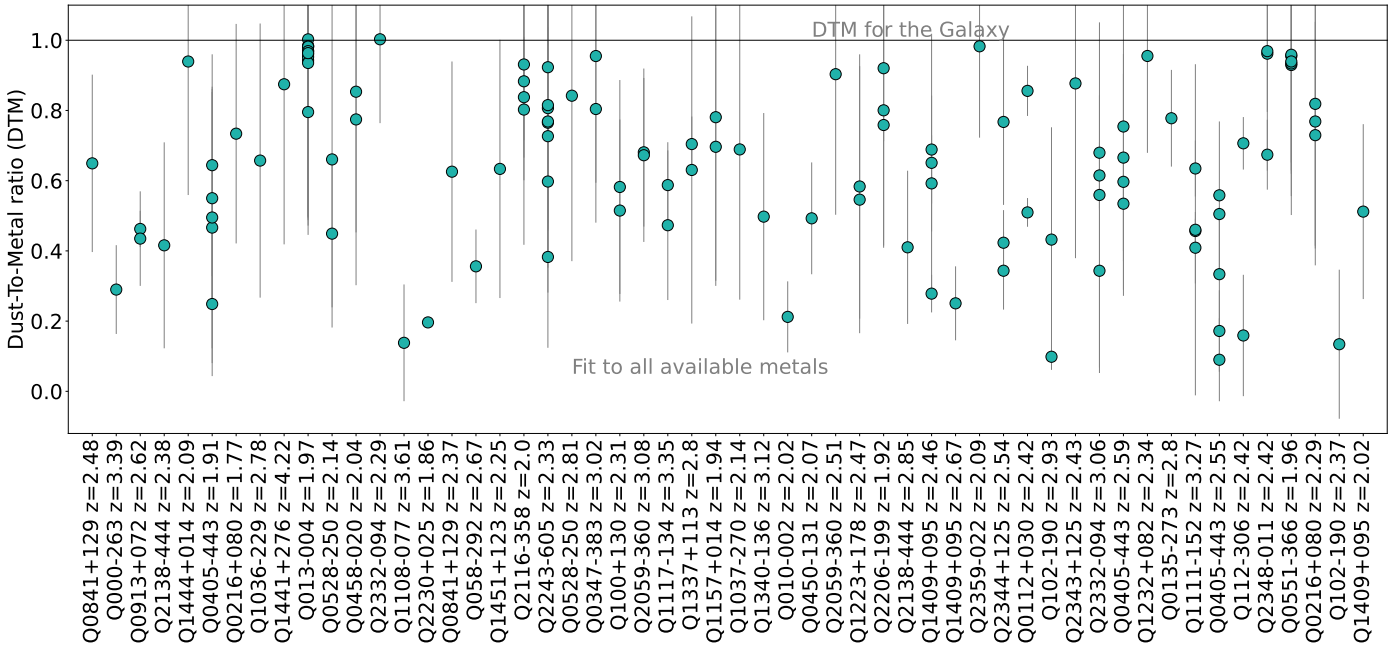

Fig. 18. Dust-to-metal ratios (DTM) for each individual component in each DLA. Here, the DTM ratio was calculated by fitting to all the available metals in the depletion patterns. Notably, we see many individual components with a DTM similar to that of the Milky Way.

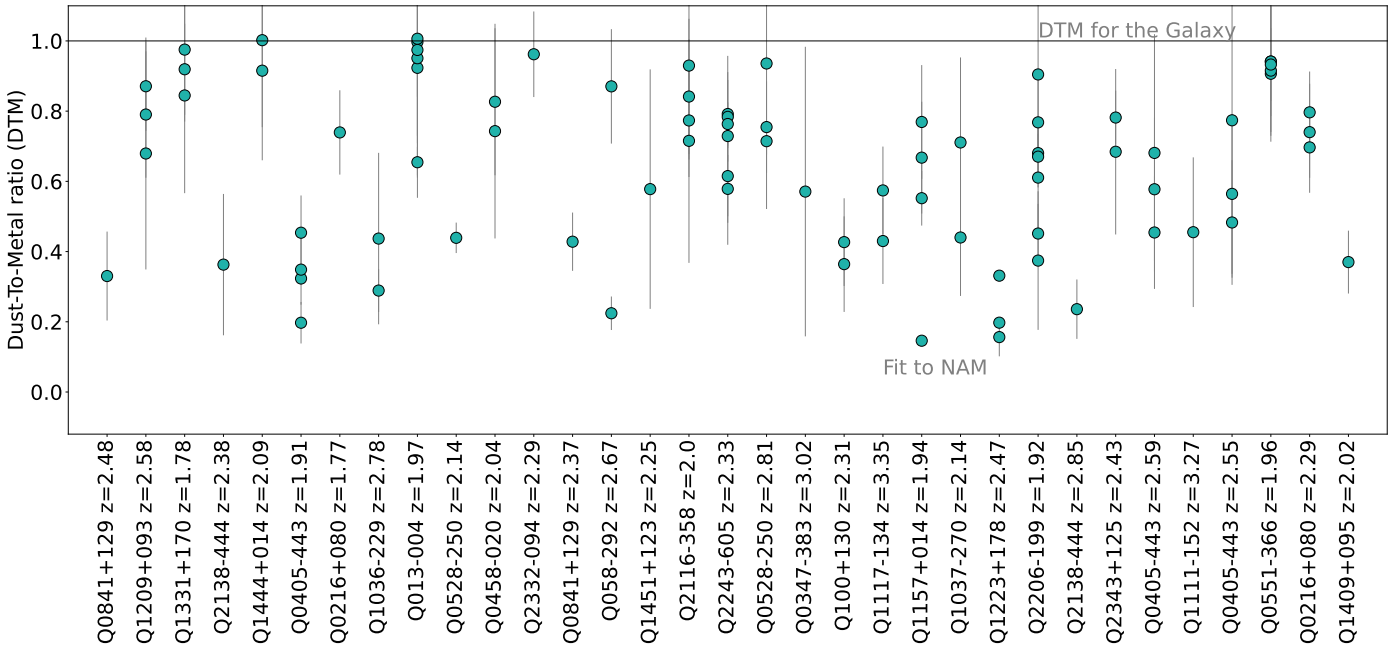

Fig. 19. Similar to Fig. 18 calculated from a fit excluding the non-α-elements and Mn.

5. We compare the chemical properties of the individual gas components with their kinematic information. We see different distributions for the zero, low-, and high-depletion components. This could be a result of some of the high-depletion components being associated with metal-rich outflows. On the other hand, some of the low-depletion components are consistent with metal-poor infalling gas.
6. In the system towards QSO 0013−004 we observe components with high depletion (up to $[\mathrm{Zn/Fe}]_{\mathrm{fit}} \sim 1.25$) and high velocities (up to $\sim -600\,\mathrm{km\,s^{-1}}$). This system could be a massive DLA galaxy, and the high-depletion, high-velocity components may suggest evidence of metal-enriched outflows. On the other hand, this could be a galaxy system of two subsystems centred at $0\,\mathrm{km\,s^{-1}}$ and $\sim -480\,\mathrm{km\,s^{-1}}$ with similar chemical enrichment. The system towards QSO 2243−605 has low-depletion, high-velocity components, which could be evidence for infalling metal-poor gas onto the galaxy.

Although it is difficult to make any solid conclusions about infalling and outflowing gas components without knowing the morphologies of these galaxies, our results on the diversity of chemical enrichment within DLAs contribute towards the broad understanding of gas cycles in and around galaxies across cosmic time.

Acknowledgements. T.R.-H., A.D.C., J.-K.K., and C.K. acknowledge support by the Swiss National Science Foundation under grant 185692. This work is based on observations carried out at the European Organisation for Astronomical Research in the Southern Hemisphere under ESO programmes 065.P-0038, 065.O-0063, 066.A-0624, 067.A-0078, and 068.A-0600. This research has made use of NASA's Astrophysics Data System. N.B. acknowledges support from the grant 3DGasFlows (ANR-17-CE31-0017) from the Agence Nationale de Recherche (ANR).

References

Arellano-Córdova, K. Z., Esteban, C., García-Rojas, J., & Méndez-Delgado, J. E. 2020, MNRAS, 496, 1051
Asplund, M., Amarsi, A. M., & Grevesse, N. 2021, A&A, 653, A141
Augustin, R., Péroux, C., Møller, P., et al. 2018, MNRAS, 478, 3120
Balashev, S. A., Ledoux, C., Noterdaeme, P., et al. 2020, MNRAS, 497, 1946
Becker, G. D., Sargent, W. L. W., Rauch, M., & Carswell, R. F. 2012, ApJ, 744, 91
Bouché, N., Lowenthal, J. D., Charlton, J. C., et al. 2001, ApJ, 550, 585
Bouché, N., Hohensee, W., Vargas, R., et al. 2012, MNRAS, 426, 801
Bouché, N., Murphy, M. T., Kacprzak, G. G., et al. 2013, Science, 341, 50
Christensen, L., Noterdaeme, P., Petitjean, P., Ledoux, C., & Fynbo, J. P. U. 2009, A&A, 505, 1007
Christensen, L., Møller, P., Fynbo, J. P. U., & Zafar, T. 2014, MNRAS, 445, 225
Christensen, L., Møller, P., Rhodin, N. H. P., Heintz, K. E., & Fynbo, J. P. U. 2019, MNRAS, 489, 2270
Cooke, R., Pettini, M., Steidel, C. C., Rudie, G. C., & Nissen, P. E. 2011, MNRAS, 417, 1534
Cresci, G., Mannucci, F., Maiolino, R., et al. 2010, Nature, 467, 811
Cullen, F., Shapley, A. E., McLure, R. J., et al. 2021, MNRAS, 505, 903
de Boer, T. J. L., Belokurov, V., Beers, T. C., & Lee, Y. S. 2014, MNRAS, 443, 658
De Cia, A. 2018, A&A, 613, L2
De Cia, A., Ledoux, C., Mattson, L., et al. 2016, A&A, 596, A97
De Cia, A., Ledoux, C., Petitjean, P., & Savaglio, S. 2018, A&A, 611, A76
De Cia, A., Jenkins, E. B., Fox, A. J., et al. 2021, Nature, 597, 206
de Ugarte Postigo, A., Thöne, C. C., Bolmer, J., et al. 2018, A&A, 620, A119
Dessauges-Zavadsky, M., Prochaska, J. X., & D'Odorico, S. 2002, A&A, 391, 801
Dessauges-Zavadsky, M., Prochaska, J. X., D'Odorico, S., Calura, F., & Matteucci, F. 2006, A&A, 445, 93
Dessauges-Zavadsky, M., Schaerer, D., Cava, A., Mayer, L., & Tamburello, V. 2017, ApJ, 836, L22
Field, G. B. 1974, ApJ, 187, 453
Fox, A. J., & Davé, R. 2017, Astrophys. Space Sci. Lib., 430
Fox, A. J., Richter, P., Ashley, T., et al. 2019, ApJ, 884, 53
Grazian, A., Fontana, A., Santini, P., et al. 2015, A&A, 575, A96
Guber, C. R., Richter, P., & Wendt, M. 2018, A&A, 609, A85
Jenkins, E. B. 2009, ApJ, 700, 1299
Jenkins, E. B., Savage, B. D., & Spitzer, L. 1986, ApJ, 301, 355
Konstantopoulou, C., De Cia, A., Krogager, J.-K., et al. 2022, A&A, 666, A12
Kreckel, K., Ho, I. T., Blanc, G. A., et al. 2019, ApJ, 887, 80
Krogager, J. K., Møller, P., Fynbo, J. P. U., & Noterdaeme, P. 2017, MNRAS, 469, 2959
Lambert, D. L. 1987, JApA, 8, 103
Ledoux, C., Petitjean, P., Bergeron, J., Wampler, E. J., & Srianand, R. 1998, A&A, 337, 51
Ledoux, C., Bergeron, J., & Petitjean, P. 2002a, A&A, 385, 802
Ledoux, C., Srianand, R., & Petitjean, P. 2002b, A&A, 392, 781
Ledoux, C., Petitjean, P., Fynbo, J. P. U., Møller, P., & Srianand, R. 2006, A&A, 457, 71
Lodders, K., Palme, H., & Gail, H. P. 2009, Landolt Börnstein, 4B, 712
Lowenthal, J. D., Heckman, T. M., Lehnert, M. D., & Elias, J. H. 1995, ApJ, 439, 588
Maiolino, R., & Mannucci, F. 2019, A&ARv, 27, 3
Marra, R., Churchill, C. W., Doughty, C., et al. 2021, MNRAS, 508, 4938
Marra, R., Churchill, C. W., Kacprzak, G. G., et al. 2022, MNRAS, submitted [arXiv:2202.12228]
McWilliam, A. 1997, ARA&A, 35, 503
Møller, P., & Christensen, L. 2020, MNRAS, 492, 4805
Møller, P., & Warren, S. J. 1993, A&A, 270, 43
Nomoto, K., Tominaga, N., Umeda, H., Kobayashi, C., & Maeda, K. 2006, Nucl. Phys. A, 777, 424
Noterdaeme, P., Ledoux, C., Petitjean, P., & Srianand, R. 2008, A&A, 481, 327
Noterdaeme, P., Krogager, J. K., Balashev, S., et al. 2017, A&A, 597, A82
Noterdaeme, P., Balashev, S., Combes, F., et al. 2021, A&A, 651, A17
Patrício, V., Richard, J., Carton, D., et al. 2019, MNRAS, 489, 224
Péroux, C., & Howk, J. C. 2020, ARA&A, 58, 363
Péroux, C., Nelson, D., van de Voort, F., et al. 2020, MNRAS, 499, 2462
Petitjean, P., Srianand, R., & Ledoux, C. 2002, MNRAS, 332, 383
Phillips, A. P., Gondhalekar, P. M., & Pettini, M. 1982, MNRAS, 200, 687
Prochaska, J. X. 2003, ApJ, 582, 49
Prochaska, J. X., & Wolfe, A. M. 1997, ApJ, 487, 73
Prochaska, J. X., & Wolfe, A. M. 2002, ApJ, 566, 68
Prochaska, J. X., Gawiser, E., Wolfe, A. M., Castro, S., & Djorgovski, S. G. 2003, ApJ, 595, L9
Rafelski, M., Wolfe, A. M., Prochaska, J. X., Neeleman, M., & Mendez, A. J. 2012, ApJ, 755, 89
Rodríguez, E., Petitjean, P., Aracil, B., Ledoux, C., & Srianand, R. 2006, A&A, 446, 791
Roman-Duval, J., Jenkins, E. B., Tchernyshyov, K., et al. 2021, ApJ, 910, 95
Sánchez Almeida, J., Elmegreen, B. G., Muñoz-Tuñón, C., et al. 2015, ApJ, 810, L15
Savage, B. D., & Sembach, K. R. 1996, ARA&A, 34, 279
Skúladóttir, Á., Tolstoy, E., Salvadori, S., Hill, V., & Pettini, M. 2017, A&A, 606, A71
Slavin, J., Dwek, E., Mac Low, M.-M., et al. 2020, ApJ, 902, 135
Srianand, R., & Petitjean, P. 1998, A&A, 335, 33
Tinsley, B. M. 1979, ApJ, 229, 1046
Tolstoy, E., Hill, V., & Tosi, M. 2009, ARA&A, 47, 371
Triani, D. P., Sinha, M., Croton, D. J., Pacifici, C., & Dwek, E. 2020, MNRAS, 493, 2490
Tumlinson, J., Peeples, M., & Werk, J. K. 2017, ARA&A, 55, 389
Vladilo, G. 2002, A&A, 391, 407
Vladilo, G., Centurión, M., Bonifacio, P., & Howk, J. C. 2001, ApJ, 557, 1007
Wang, X., Li, Z., Cai, Z., et al. 2022, ApJ, 926, 70
Welty, D. E., Sonnentrucker, P., Snow, T. P., & York, D. G. 2020, ApJ, 897, 36
Wendt, M., Bouché, N. F., Zabl, J., Schroetter, I., & Muzahid, S. 2021, MNRAS, 502, 3733
Wiseman, P., Perley, D. A., Schady, P., et al. 2017, A&A, 607, A107
Wolfe, A. M. 1986, Philos. Trans. R. Soc. London Ser. A, 320, 503
York, D. G., Straka, L. A., Bishof, M., et al. 2012, MNRAS, 423, 3692

Appendix A: Depletion sequences

Figure A.1 shows the relation between the dust tracer [Zn/Fe] and the relative abundances of metals with respect to a volatile metal (Zn, S, or P). We do this for individual DLA components, while the original sequences were discovered and characterised for full DLAs (De Cia et al. 2016; Konstantopoulou et al. 2022). The correlations are also evident for individual gas components, which justifies our use of the slopes of these correlations for our sample as well.

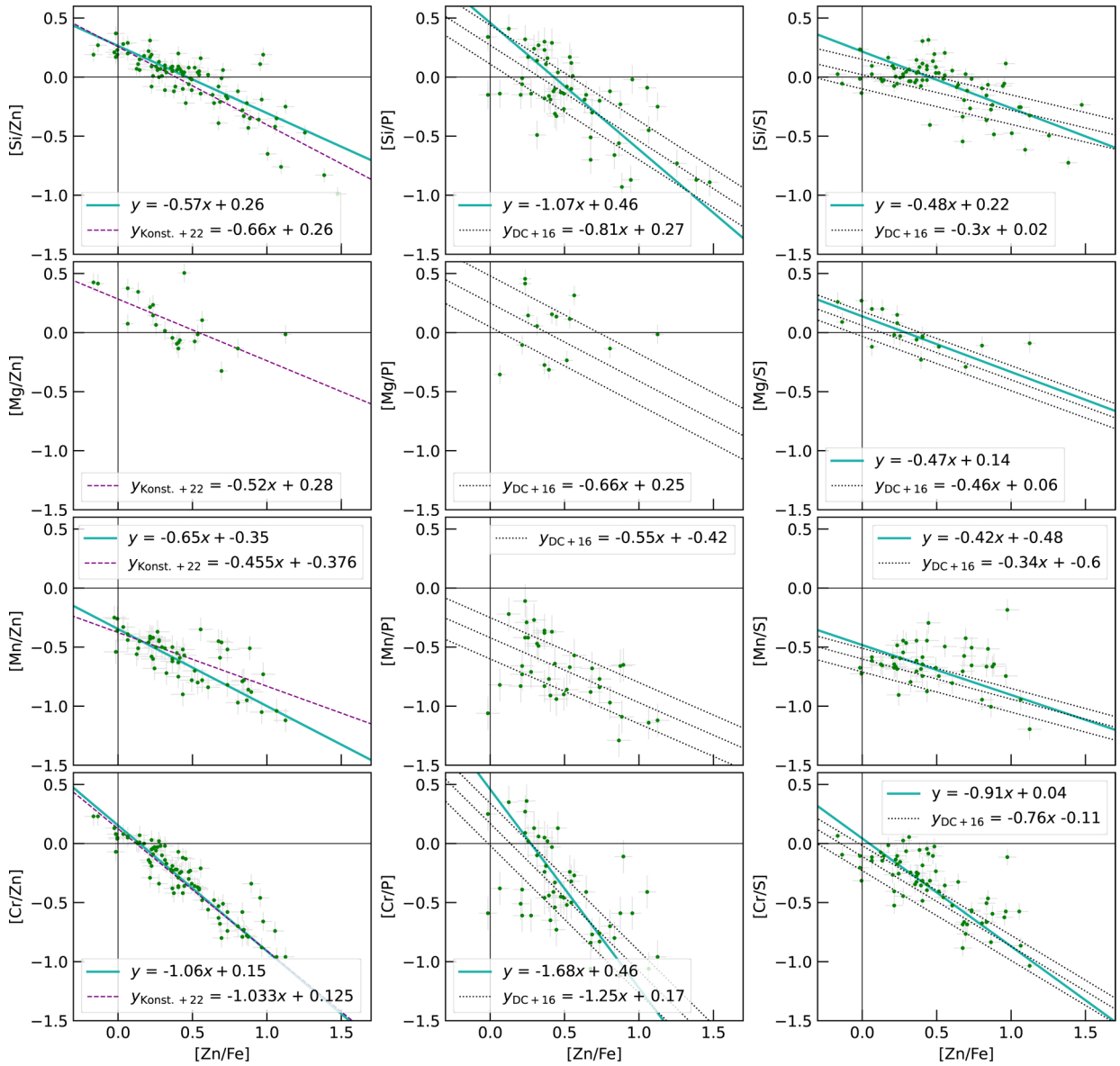

Fig. A.1. Depletion sequences (solid cyan line) fit to individual components (green points), with a comparison to those derived by De Cia et al. (2016) and Konstantopoulou et al. (2022), (black dotted and purple dashed lines respectively). We do not include linear fits for [Mg/P], [Mg/Zn] and [Mn/P] because the linear correlation coefficient is too small.

Appendix B: [Zn/Fe] versus $[Zn/Fe]_{fit}$

Figure B.1 shows a comparison between two determinations of the depletion factor. We gain a better understanding of the level of depletion when we consider more than two metals.

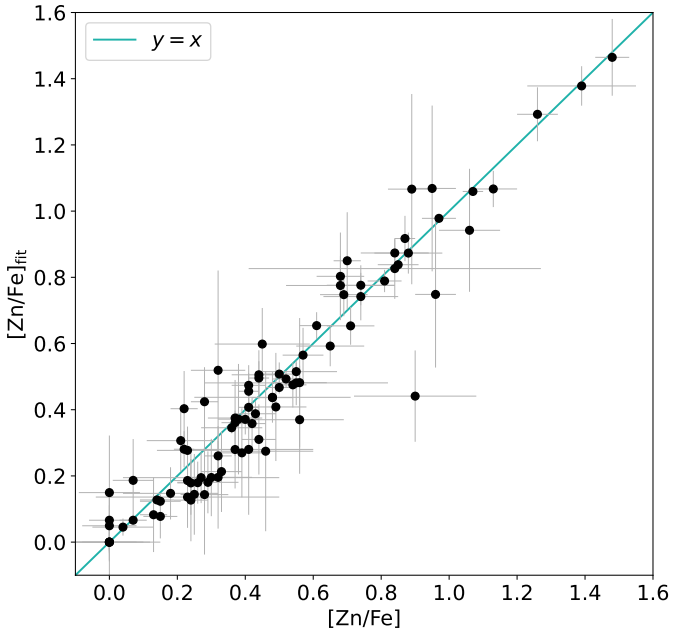

Fig. B.1. Comparison between two determinations of the depletion factor [Zn/Fe] and $[Zn/Fe]_{fit}$.

Appendix C: Depletion patterns

From the total of 70 systems, we included only those for which at least one of the individual components have three or more constrained measurements of ionic column densities. Following this criterion, we fit linear relations to the data for a total of 64 systems. Figures C.1 to C.59 show the depletion patterns of the individual components, except those already shown in Figures 1 to 4. A selected line profile to exemplify the line decomposition is shown in the bottom panel for each system.

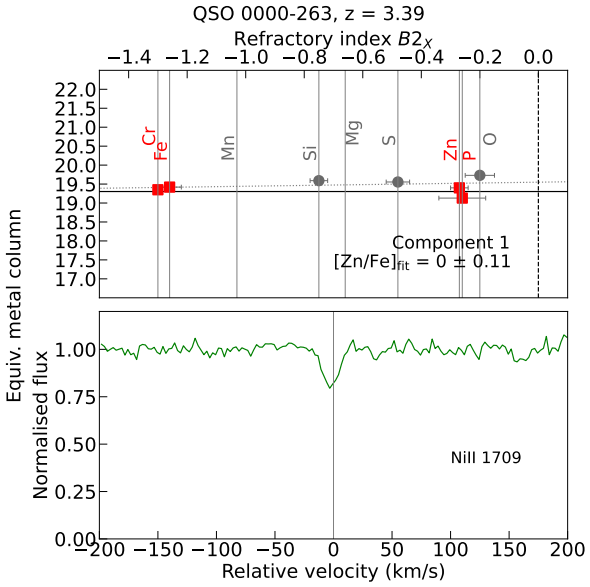

Fig. C.1. Depletion patterns and respective spectrum for QSO 0000-263.

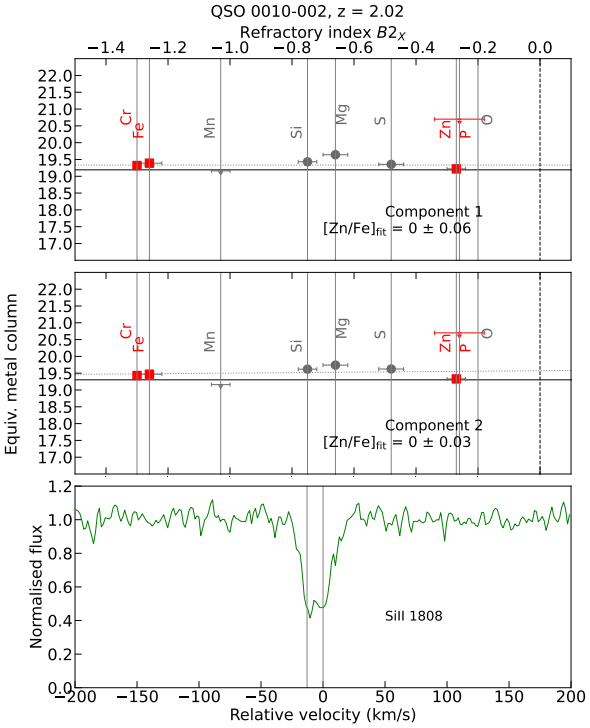

Fig. C.2. Depletion patterns and respective spectrum for QSO 0010-002.

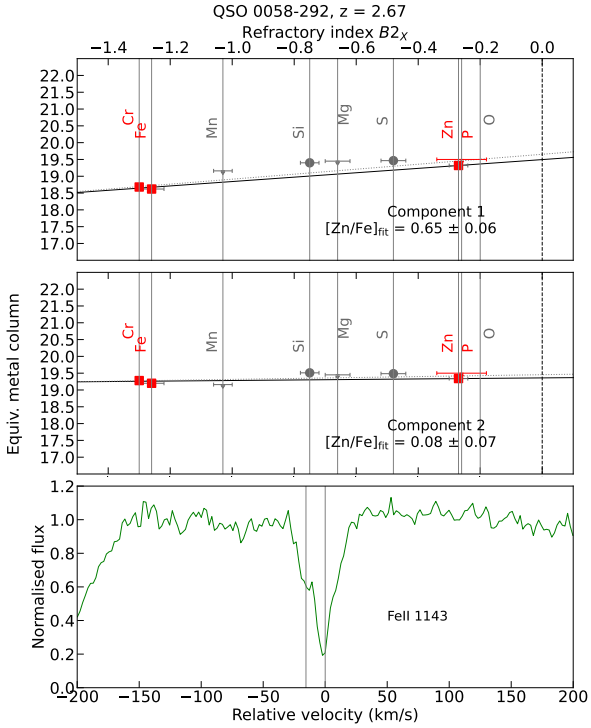

Fig. C.3. Depletion patterns and respective spectrum for QSO 0058-292.

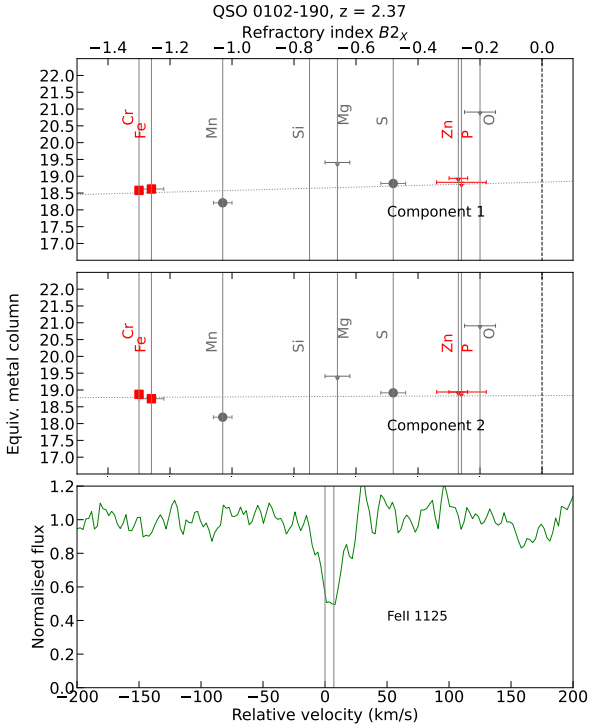

Fig. C.5. Depletion patterns and respective spectrum for QSO 0102-190.

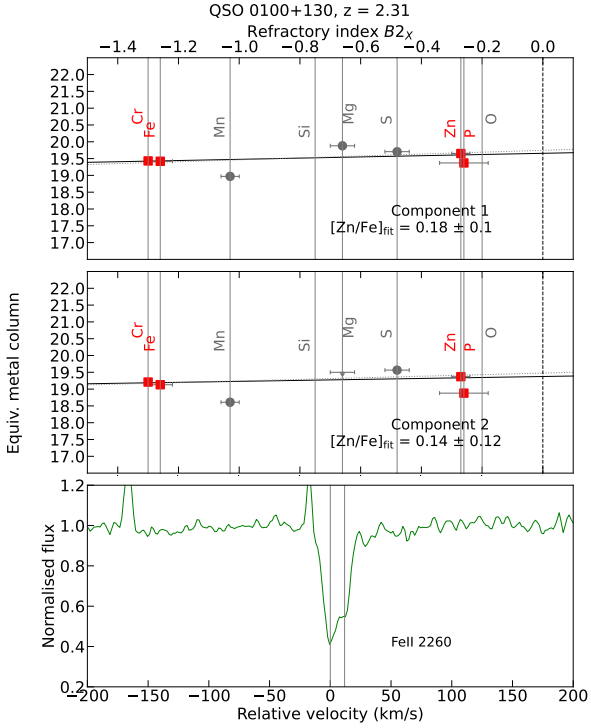

Fig. C.4. Depletion patterns and respective spectrum for QSO 0100+130.

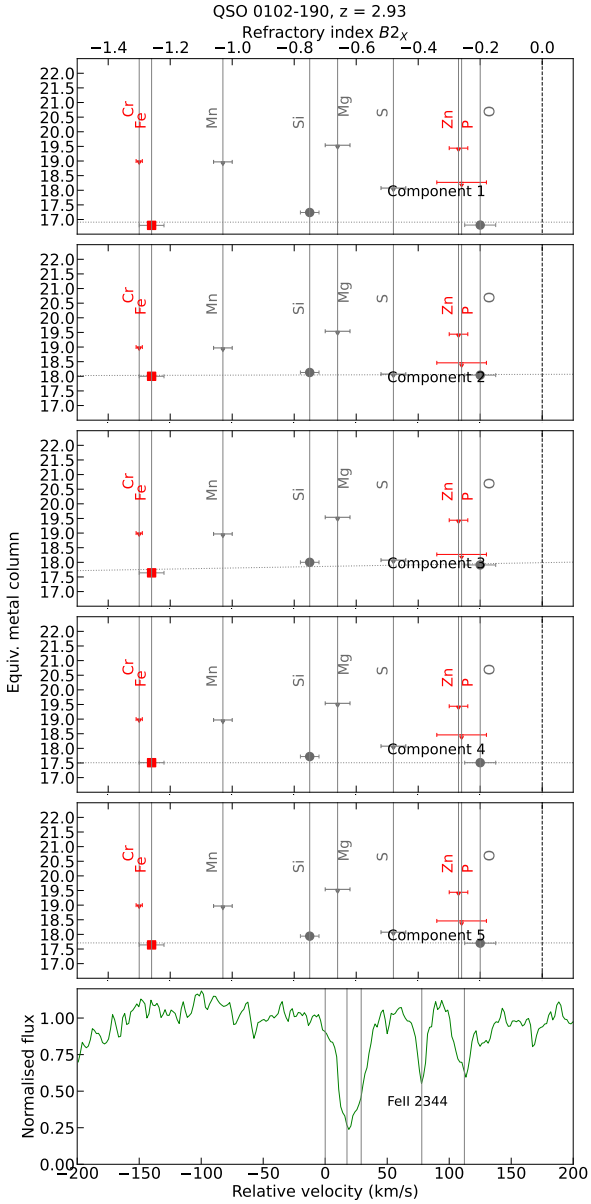

Fig. C.6. Depletion patterns and respective spectrum for QSO 0102-190.

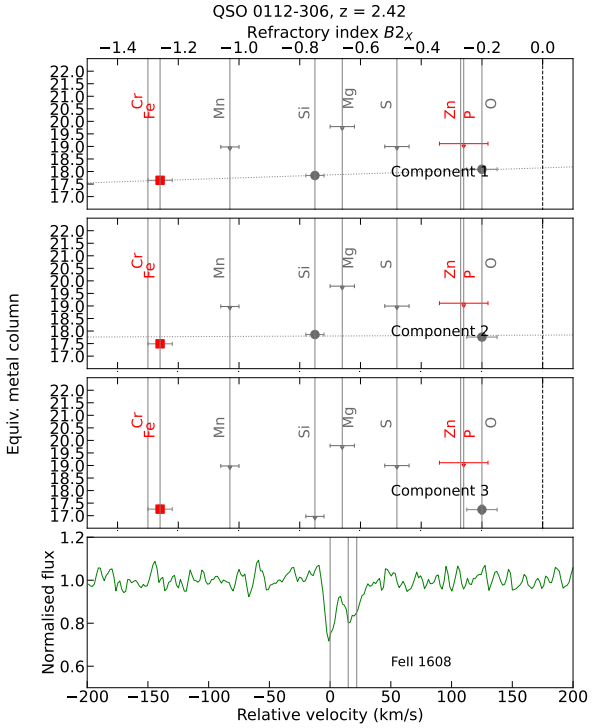

Fig. C.7. Depletion patterns and respective spectrum for QSO 0112-306.

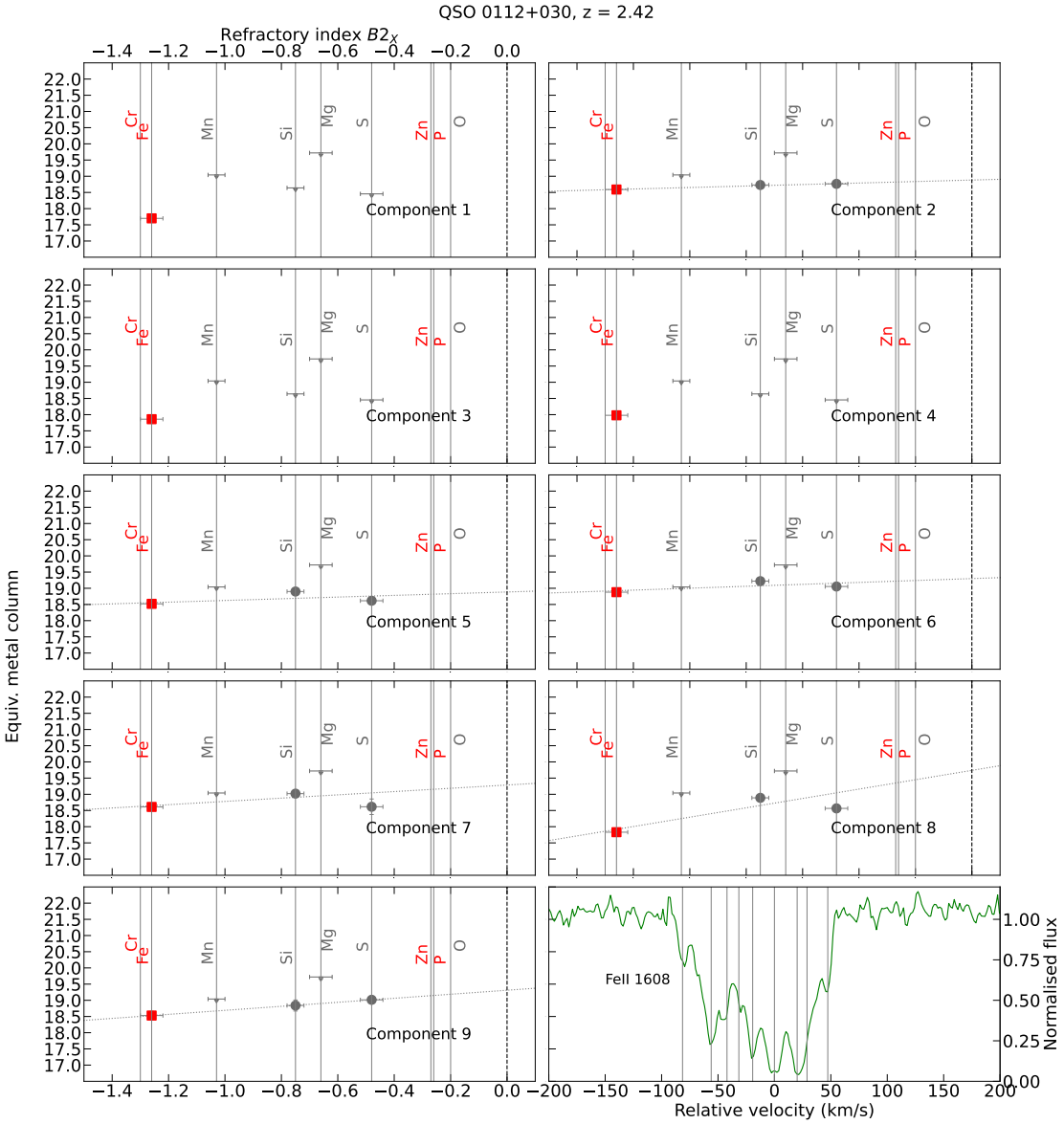

Fig. C.8. Depletion patterns and respective spectrum for QSO 0112+030.

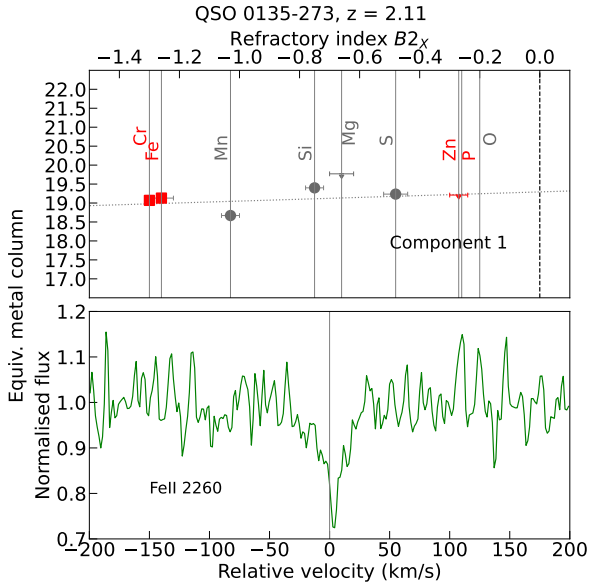

Fig. C.9. Depletion patterns and respective spectrum for QSO 0135-273

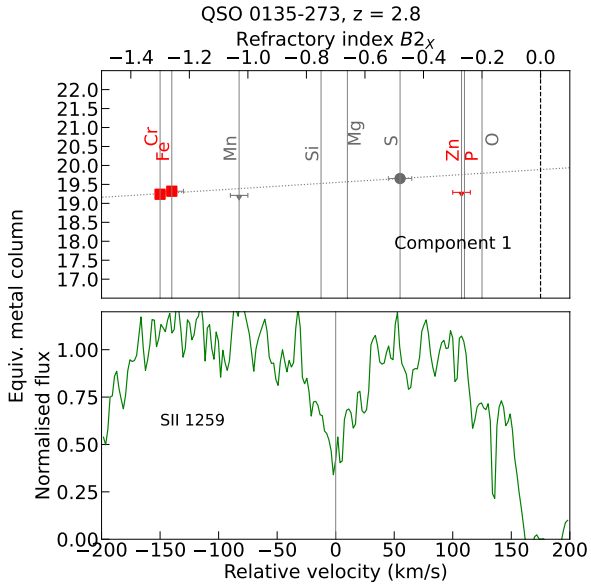

Fig. C.10. Depletion patterns and respective spectrum for QSO 0135-273

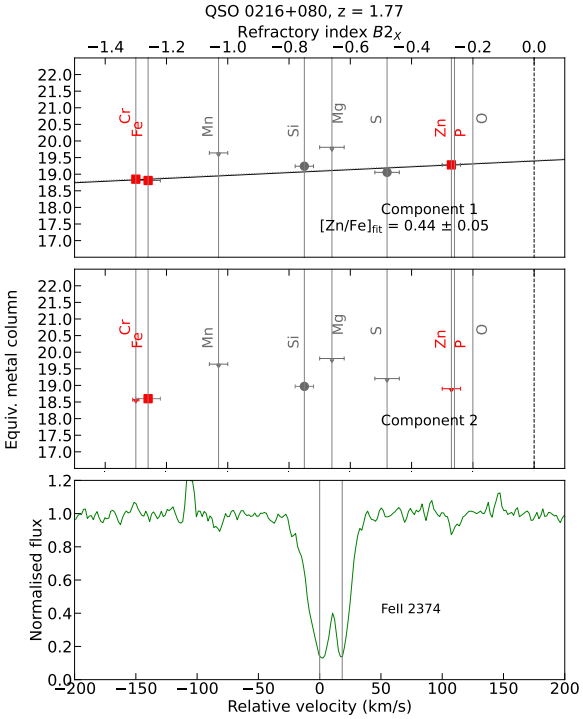

Fig. C.11. Depletion patterns and respective spectrum for QSO 0216+080.

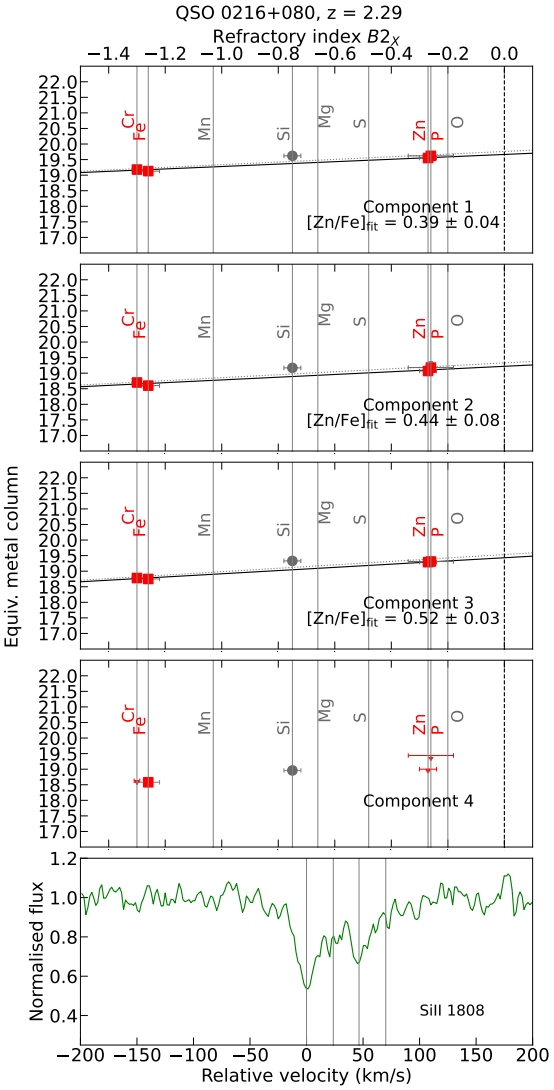

Fig. C.12. Depletion patterns and respective spectrum for QSO 0216+080.

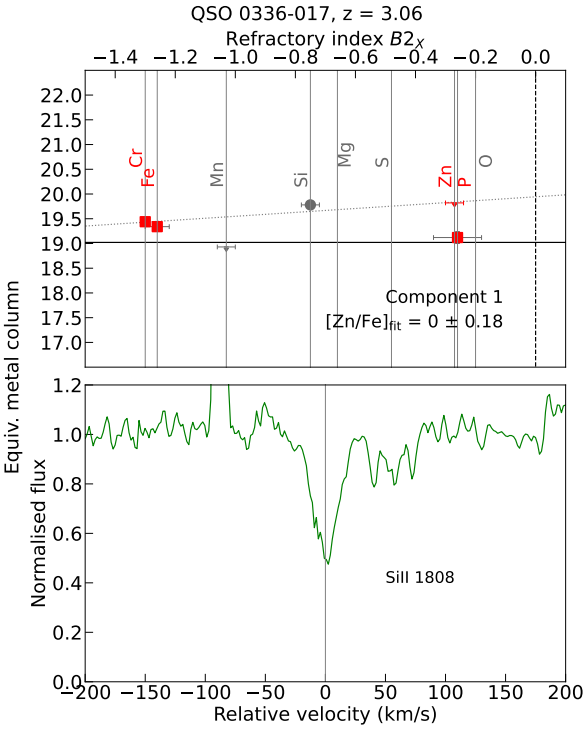

Fig. C.13. Depletion patterns and respective spectrum for QSO 0336-017.

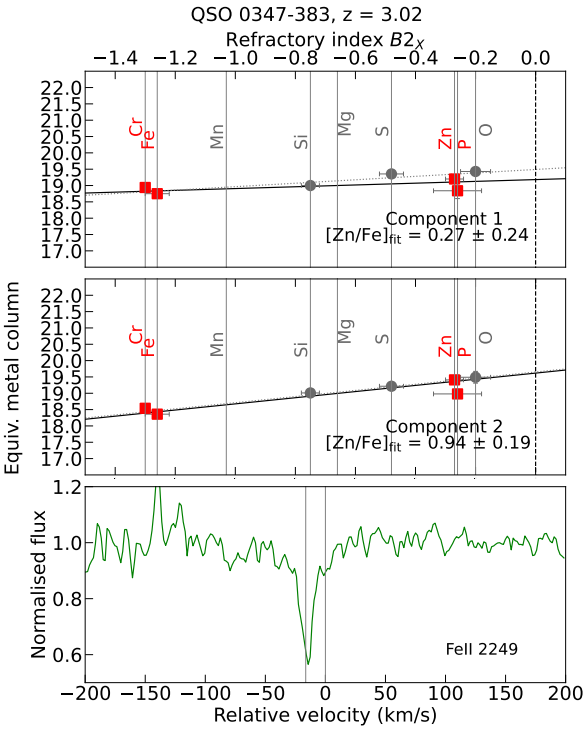

Fig. C.14. Depletion patterns and respective spectrum for QSO 0347-383.

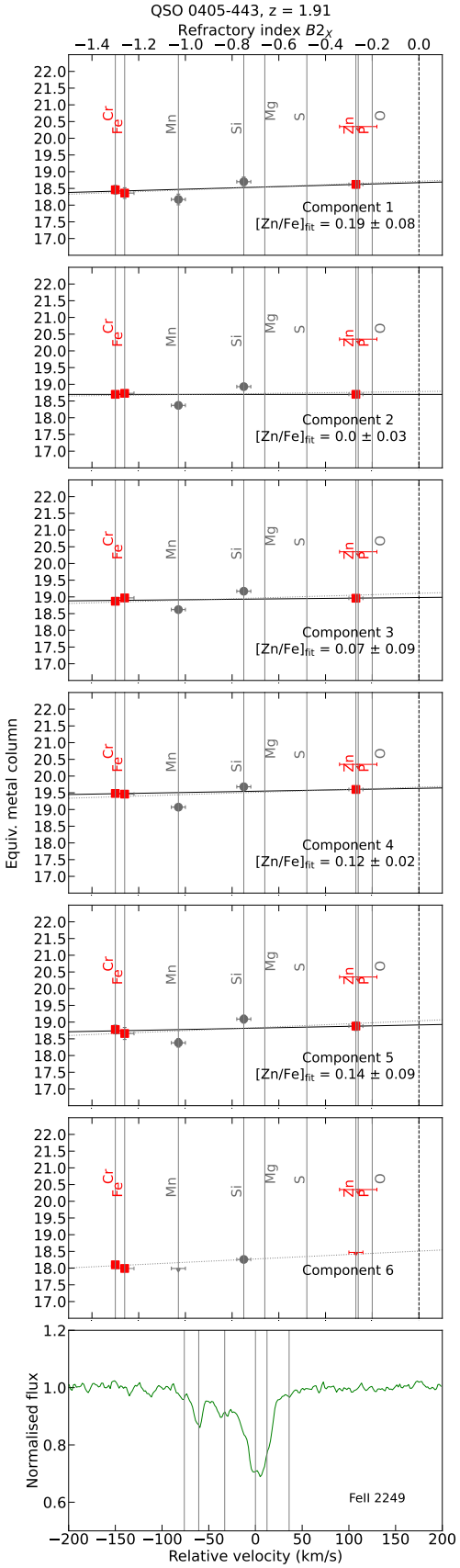

Fig. C.15. Depletion patterns and respective spectrum for QSO 0405-443.

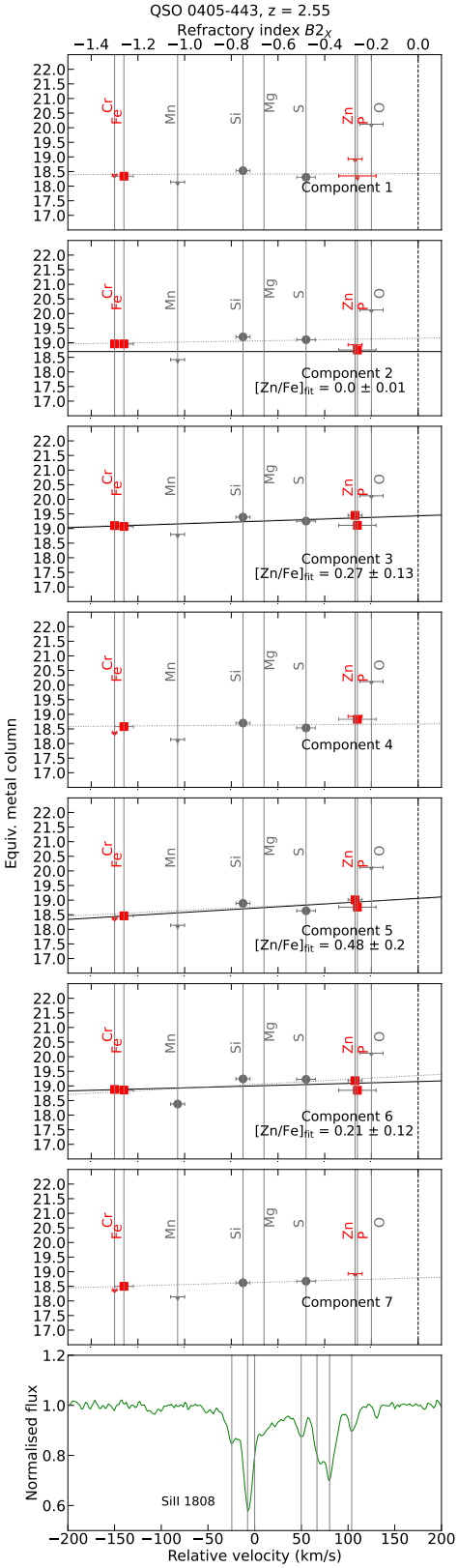

Fig. C.16. Depletion patterns and respective spectrum for QSO 0405-443.

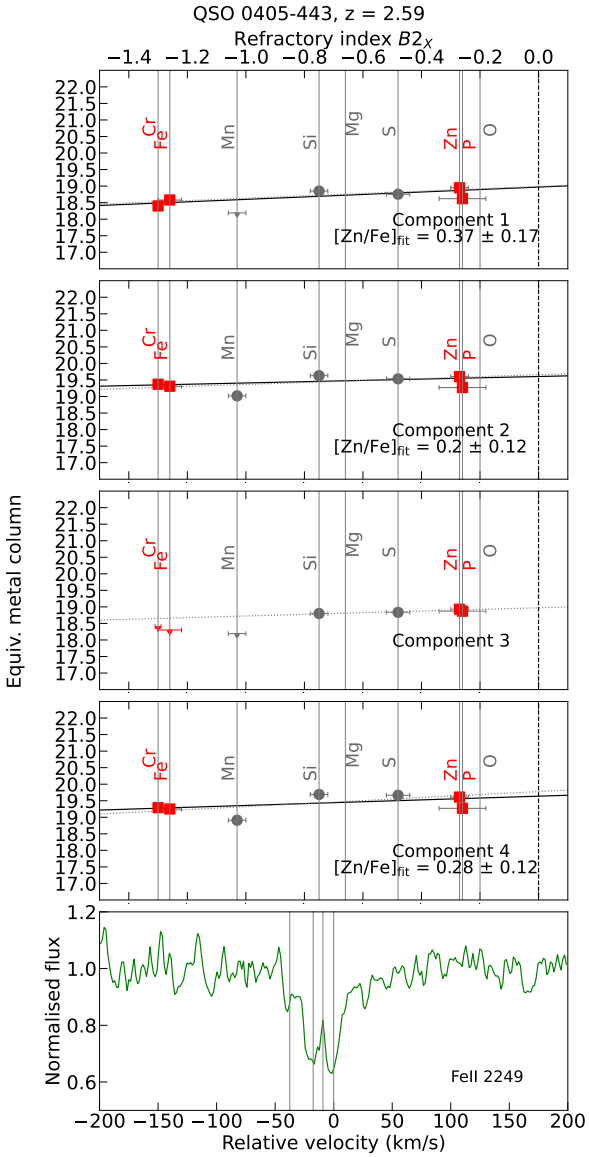

Fig. C.17. Depletion patterns and respective spectrum for QSO 0405-443.

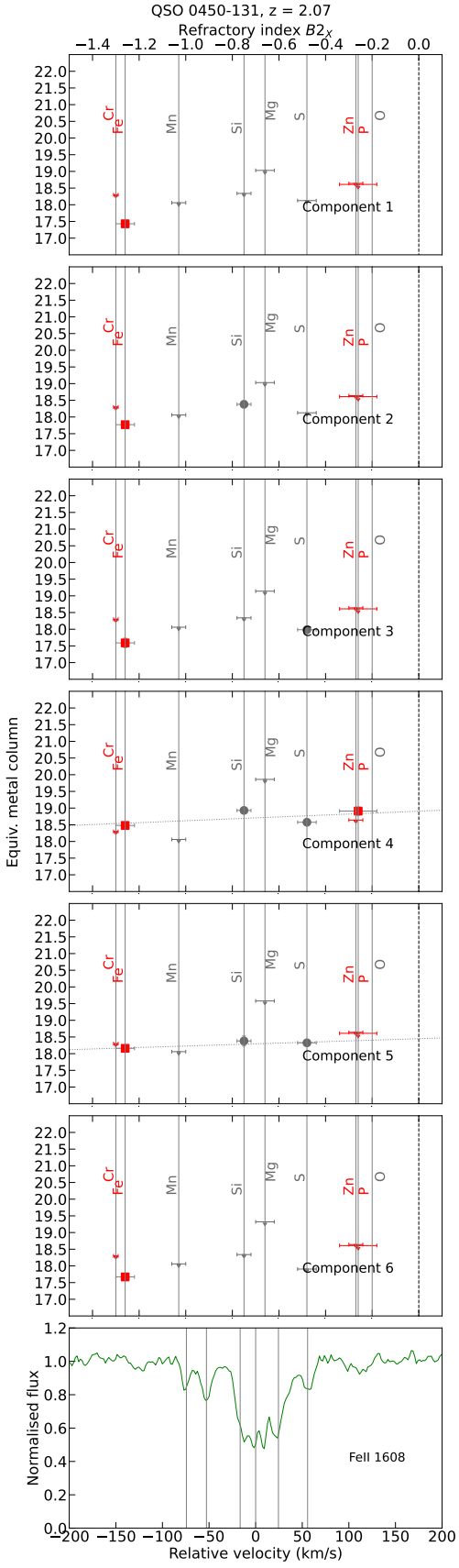

Fig. C.18. Depletion patterns and respective spectrum for QSO 0450-131.

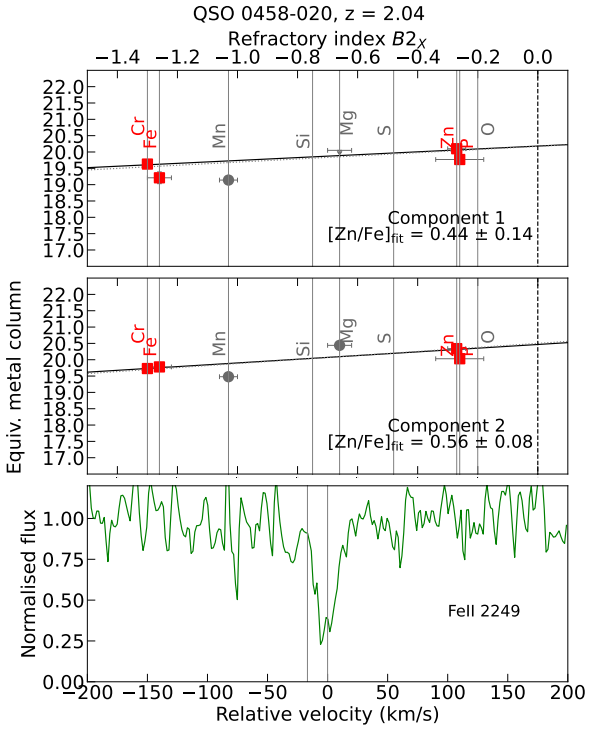

Fig. C.19. Depletion patterns and respective spectrum for QSO 0458-020.

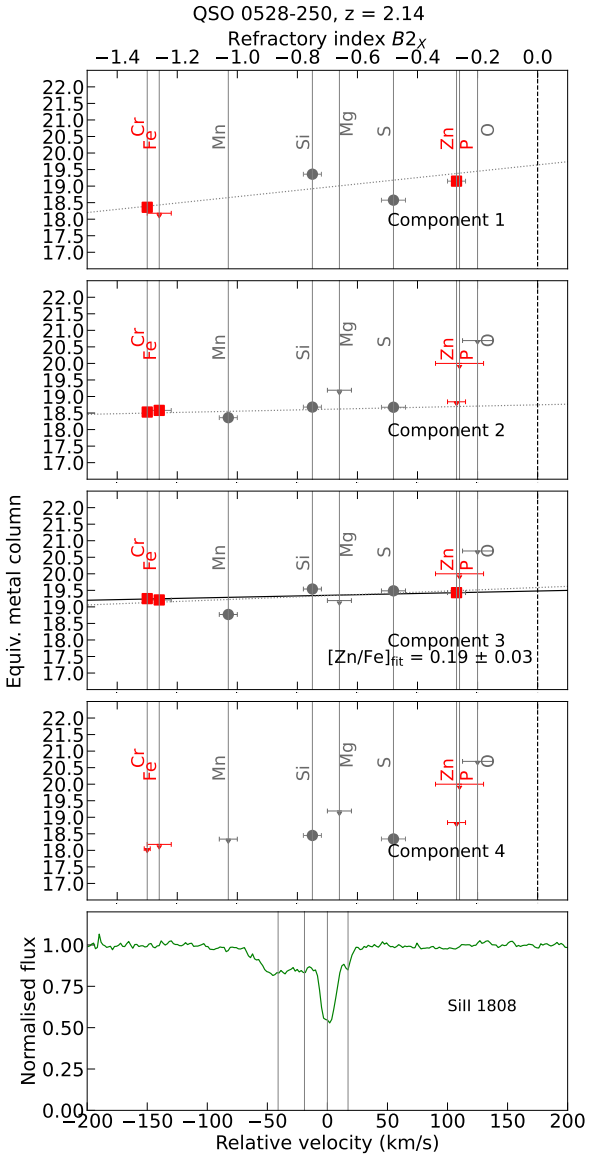

Fig. C.20. Depletion patterns and respective spectrum for QSO 0528-250.

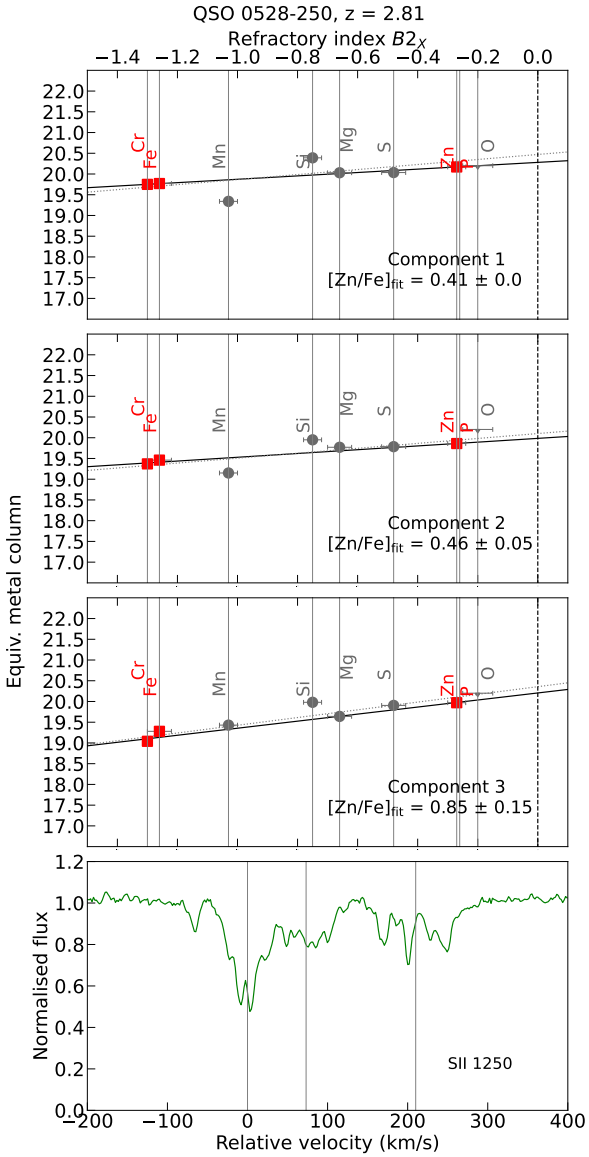

Fig. C.21. Depletion patterns and respective spectrum for QSO 0528-250.

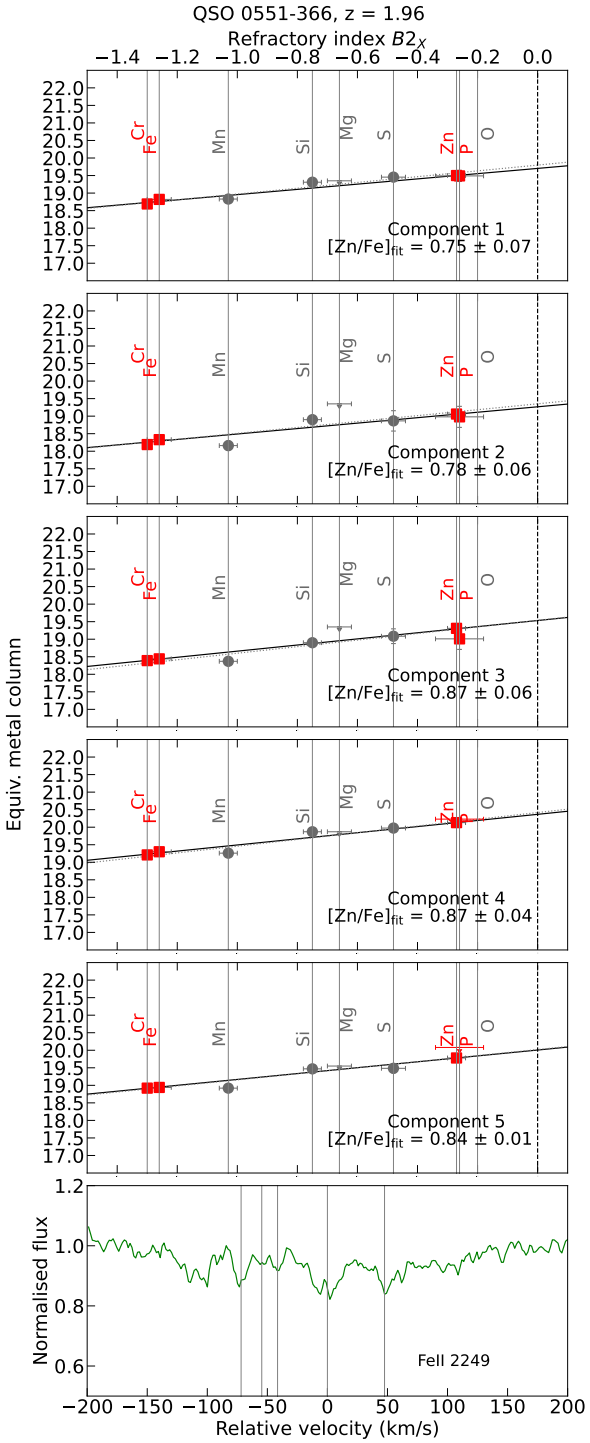

Fig. C.22. Depletion patterns and respective spectrum for QSO 0551-366.

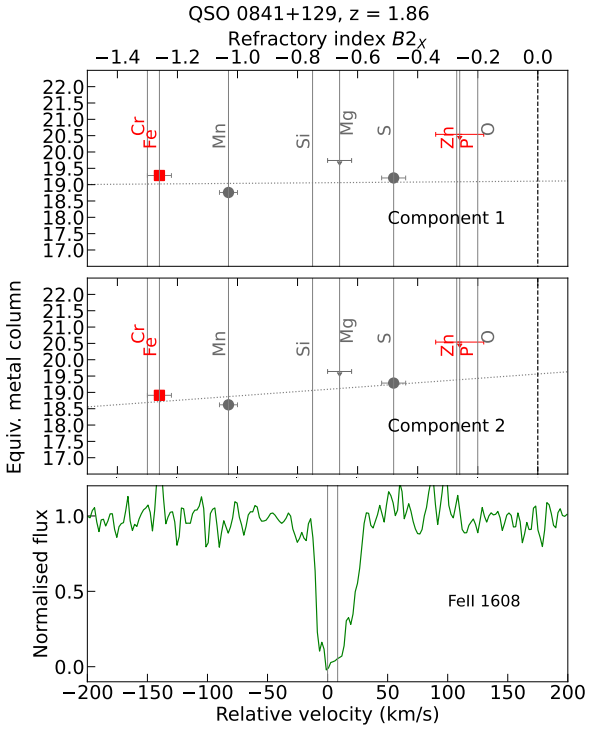

Fig. C.23. Depletion patterns and respective spectrum for QSO 0841+129.

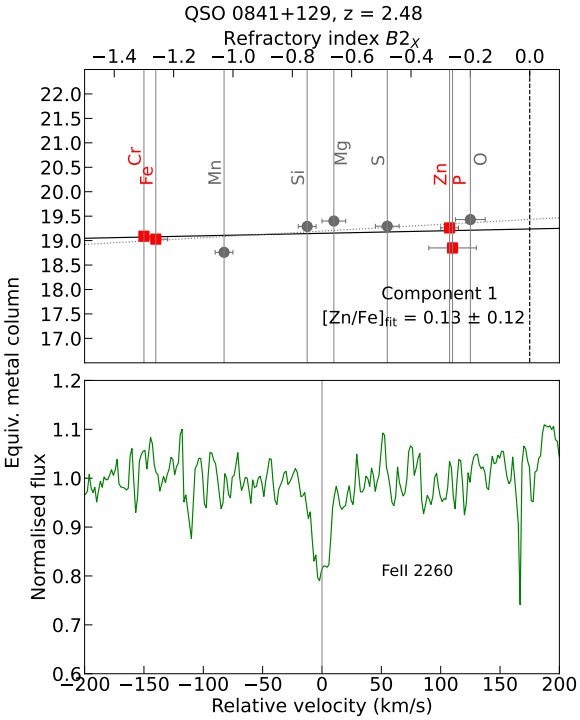

Fig. C.25. Depletion patterns and respective spectrum for QSO 0841+129.

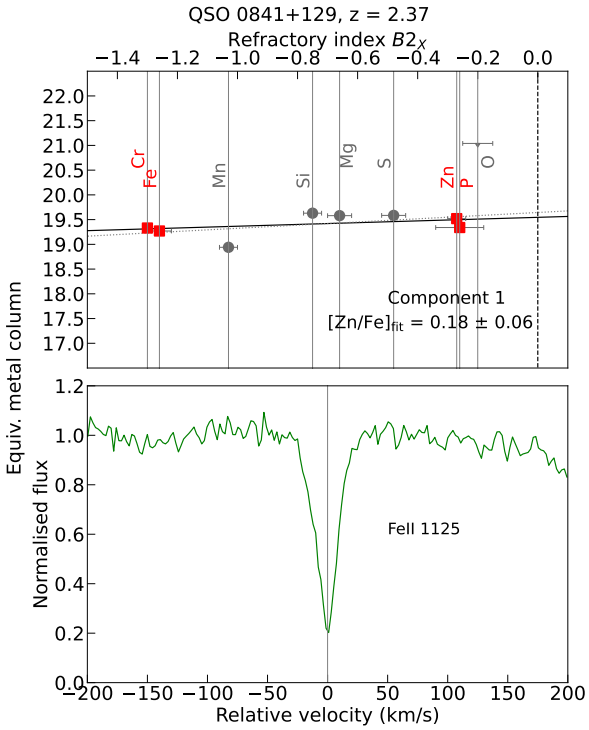

Fig. C.24. Depletion patterns and respective spectrum for QSO 0841+129.

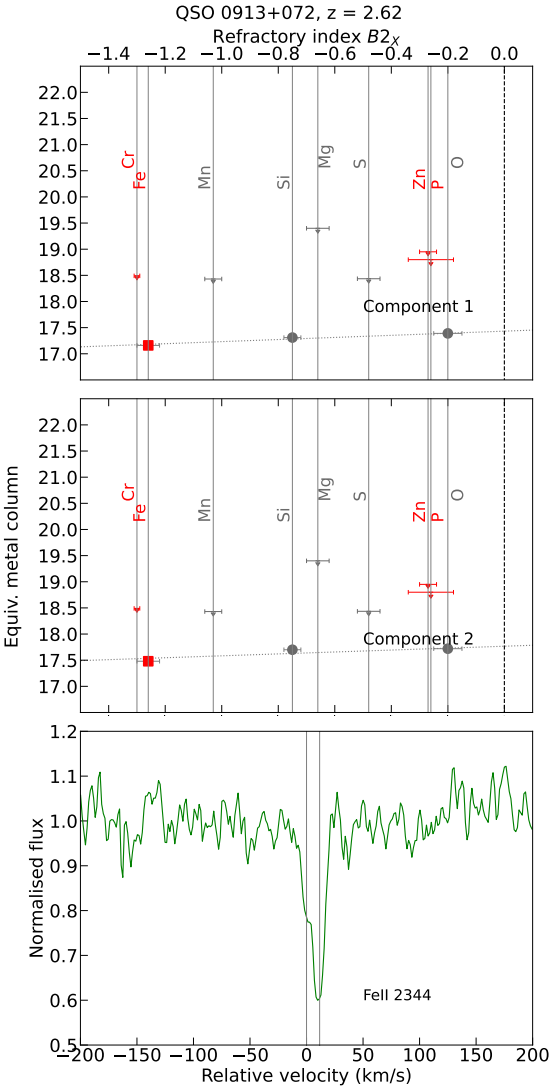

Fig. C.26. Depletion patterns and respective spectrum for QSO 0913+072.

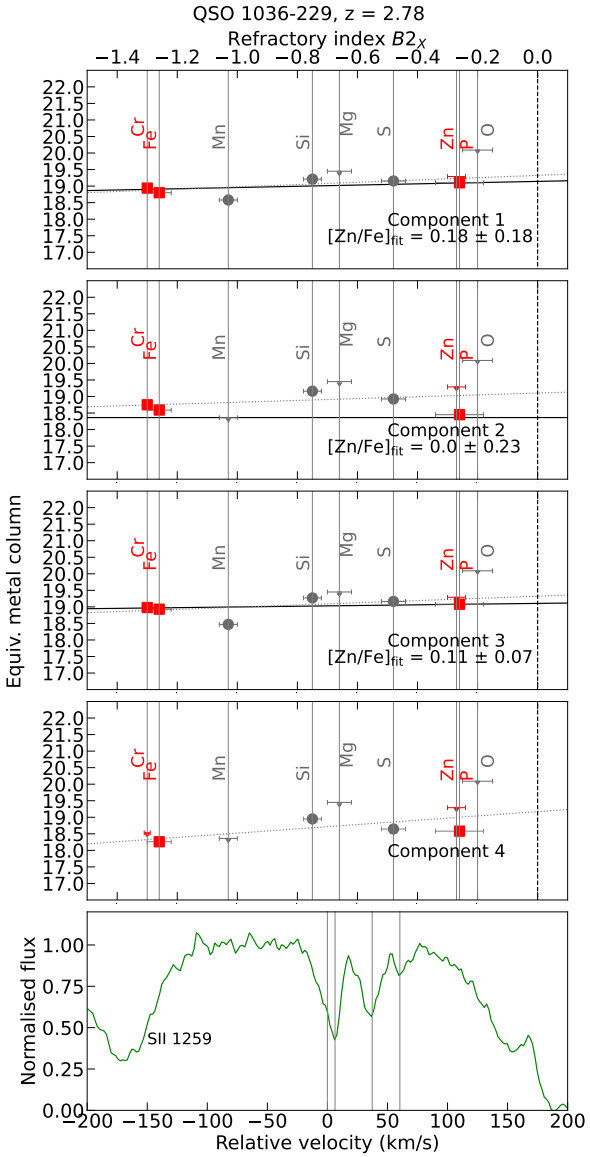

Fig. C.27. Depletion patterns and respective spectrum for QSO 1036-229.

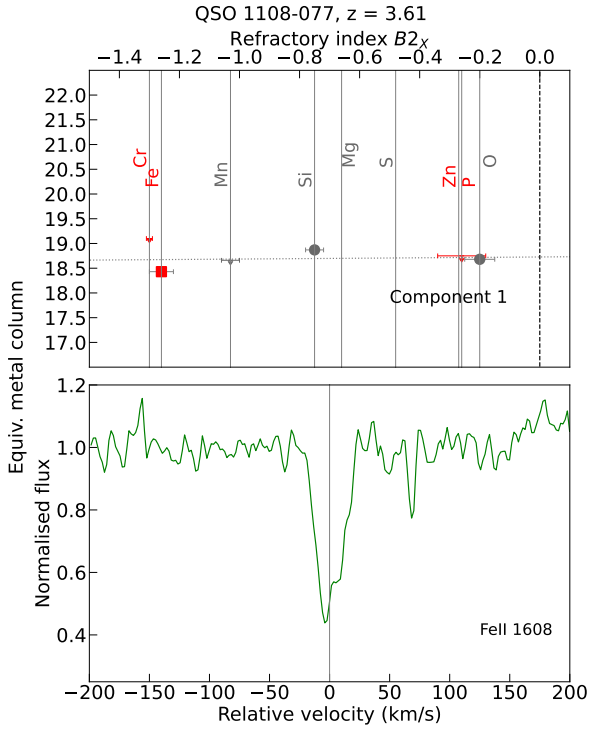

Fig. C.28. Depletion patterns and respective spectrum for QSO 1108-077.

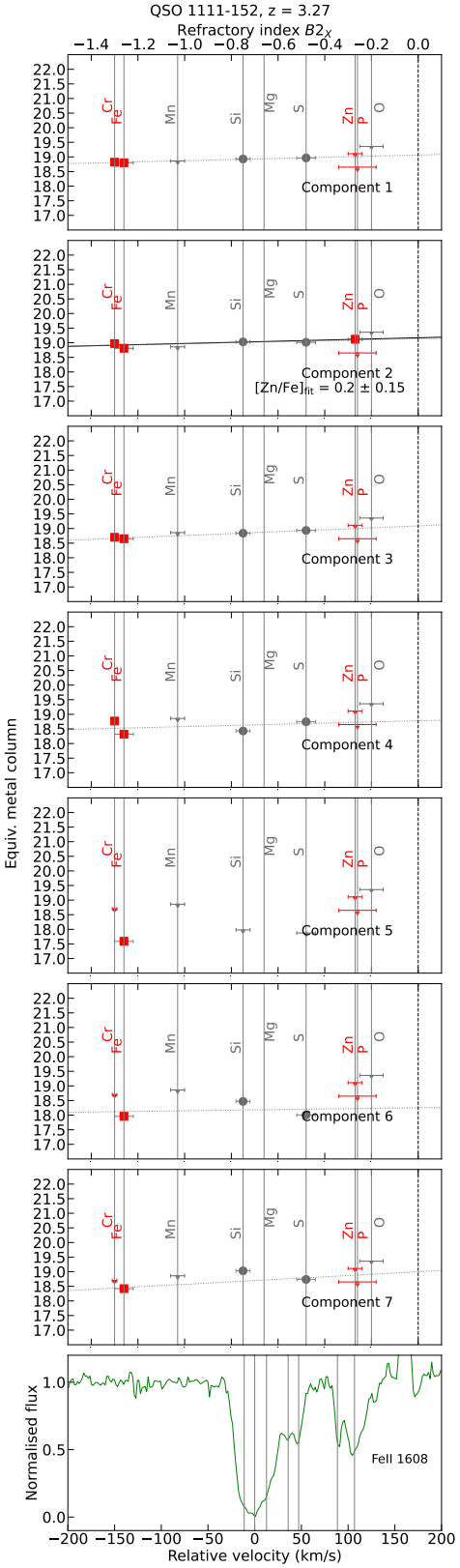

Fig. C.29. Depletion patterns and respective spectrum for QSO 1111-152.

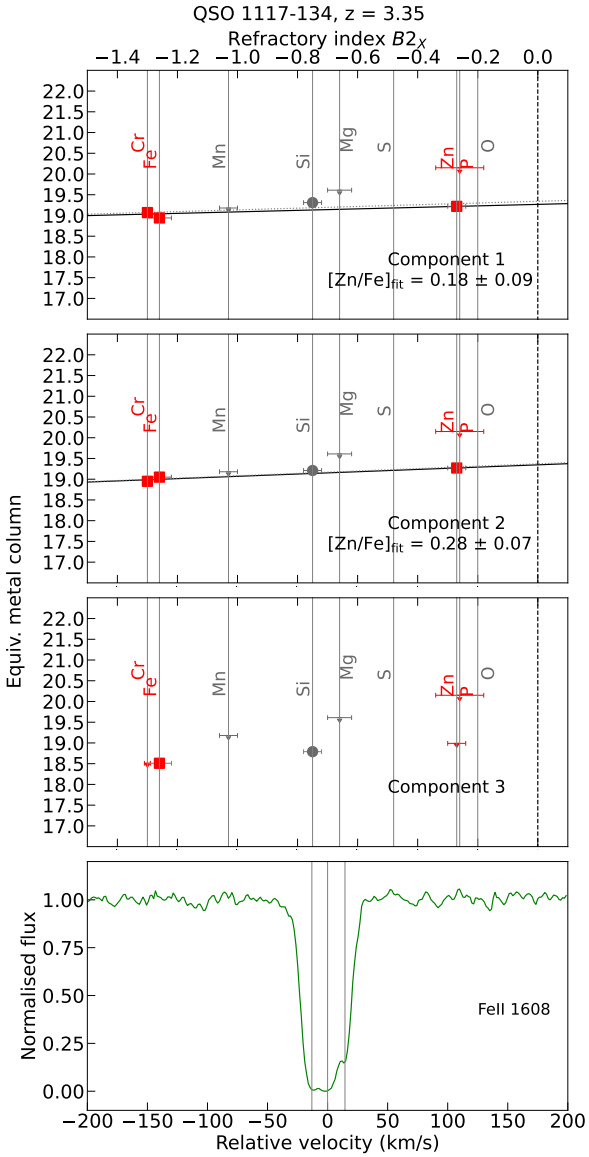

Fig. C.30. Depletion patterns and respective spectrum for QSO 1117-134.

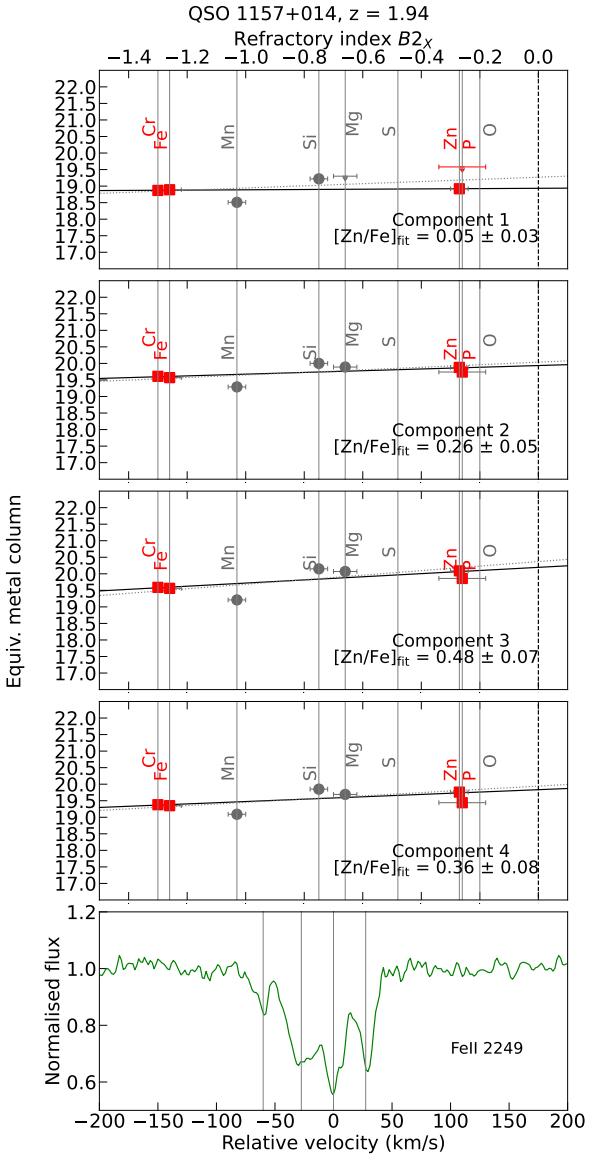

Fig. C.31. Depletion patterns and respective spectrum for QSO 1157+014.

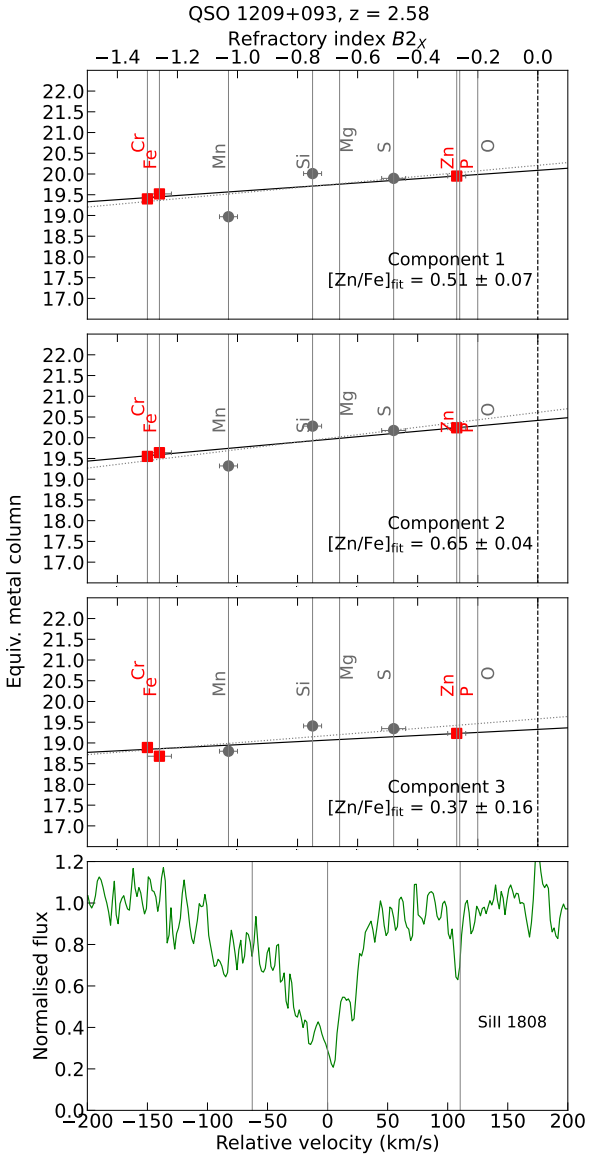

Fig. C.32. Depletion patterns and respective spectrum for QSO 1209+093.

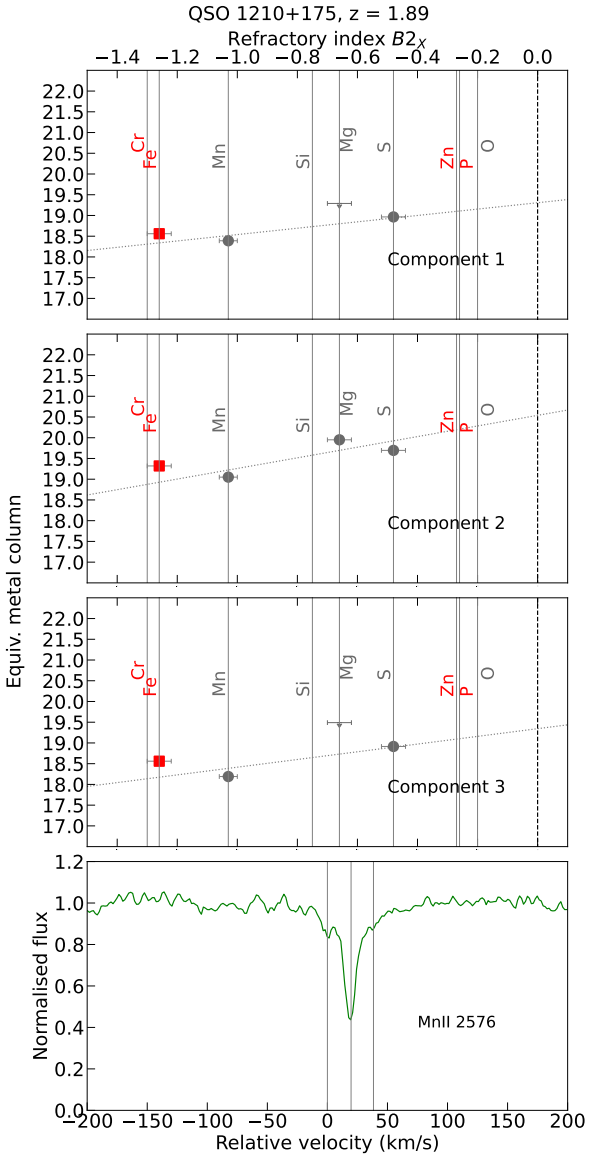

Fig. C.33. Depletion patterns and respective spectrum for QSO 1210+175.

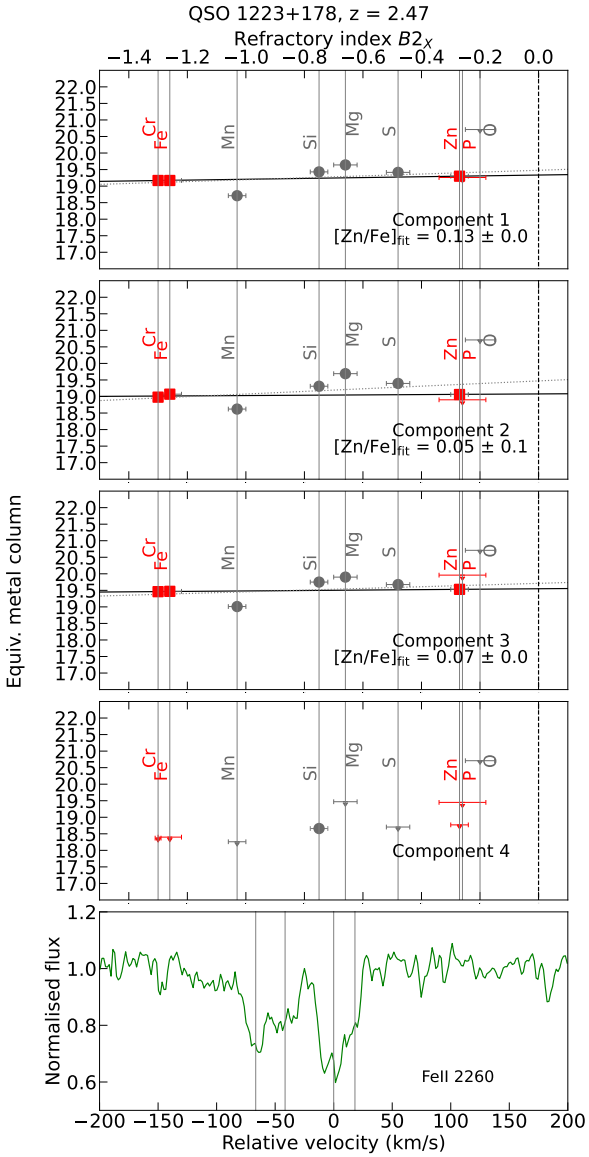

Fig. C.34. Depletion patterns and respective spectrum for QSO 1223+178.

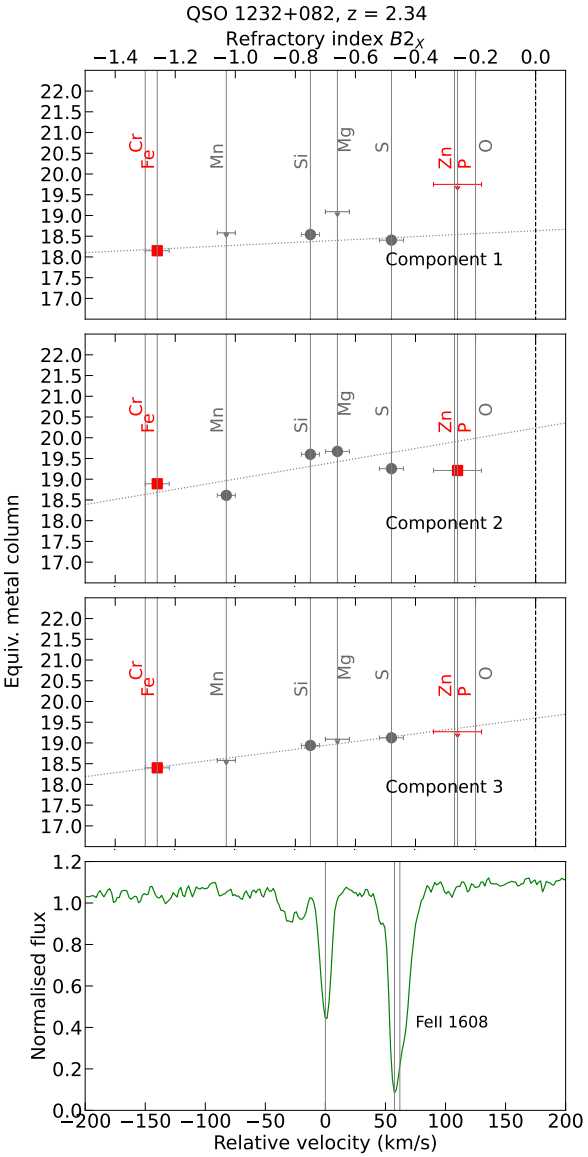

Fig. C.35. Depletion patterns and respective spectrum for QSO 1232+082.

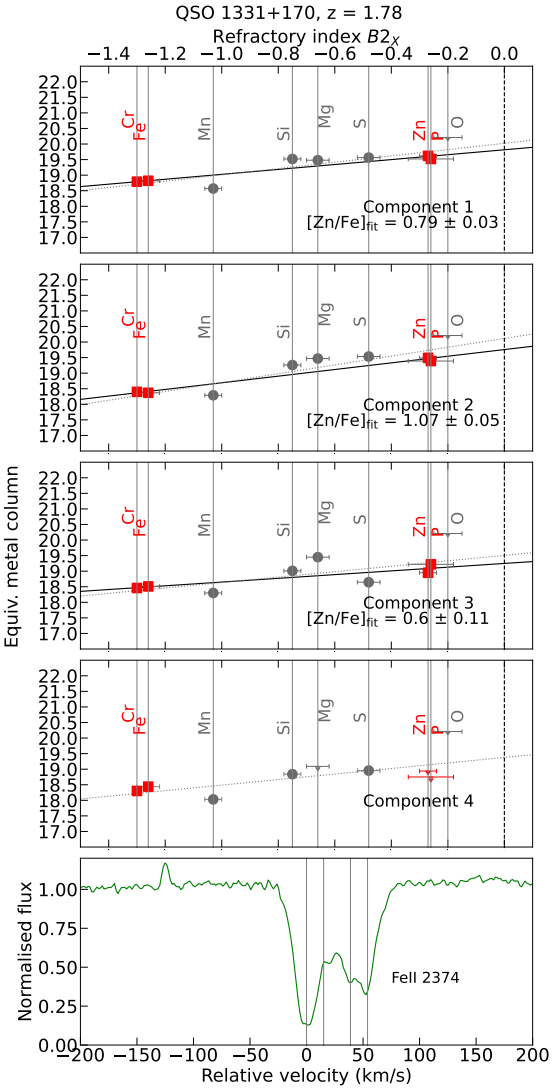

Fig. C.36. Depletion patterns and respective spectrum for QSO 1331+170.

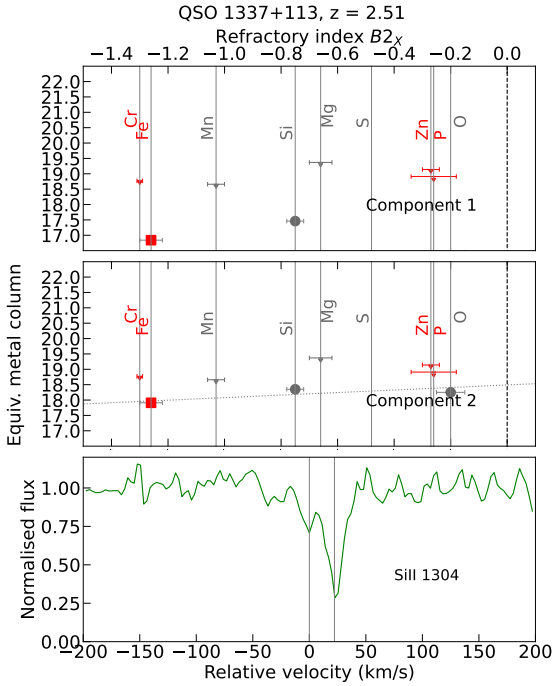

Fig. C.37. Depletion patterns and respective spectrum for QSO 1337+113.

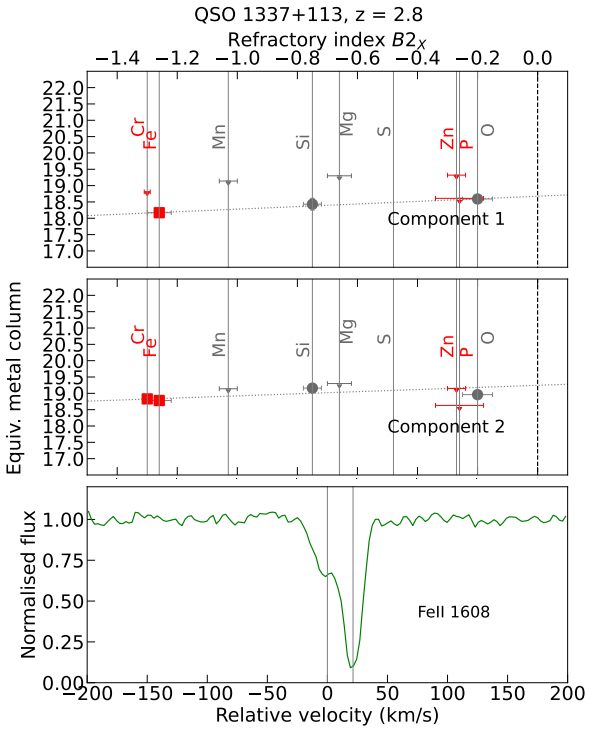

Fig. C.38. Depletion patterns and respective spectrum for QSO 1337+113.

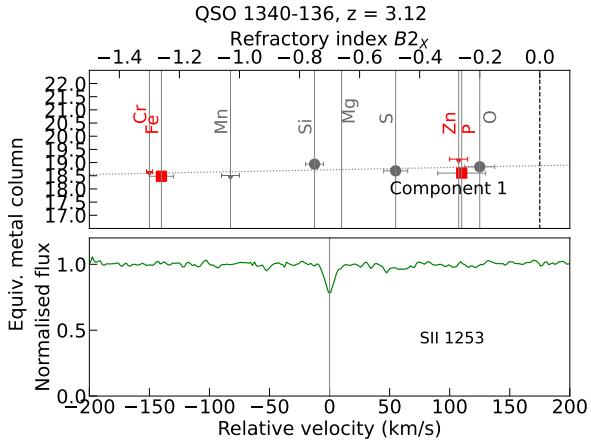

Fig. C.39. Depletion patterns and respective spectrum for QSO 1340-136.

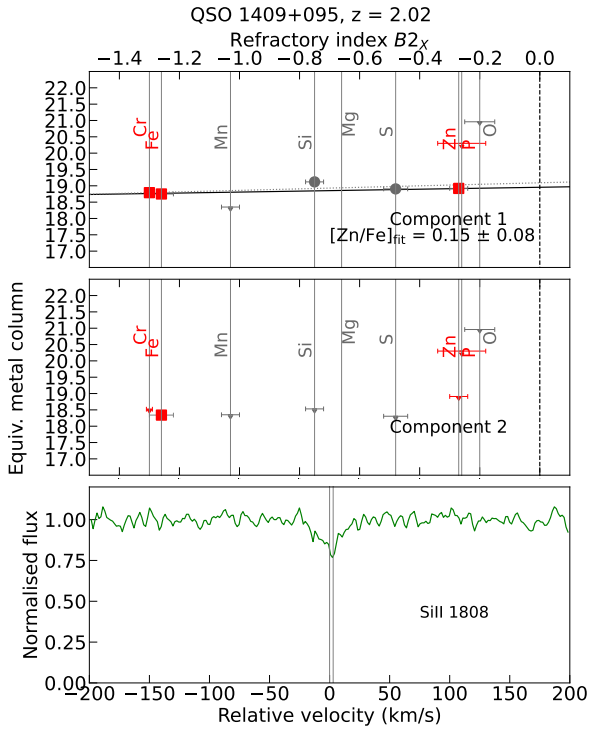

Fig. C.40. Depletion patterns and respective spectrum for QSO 1409+095.

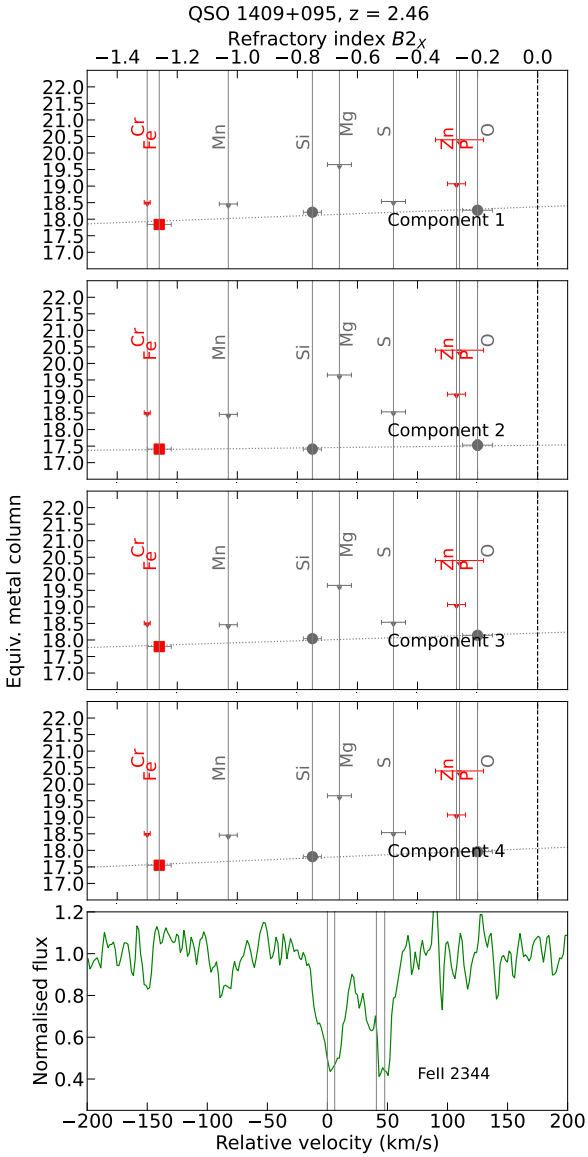

Fig. C.41. Depletion patterns and respective spectrum for QSO 1409+095.

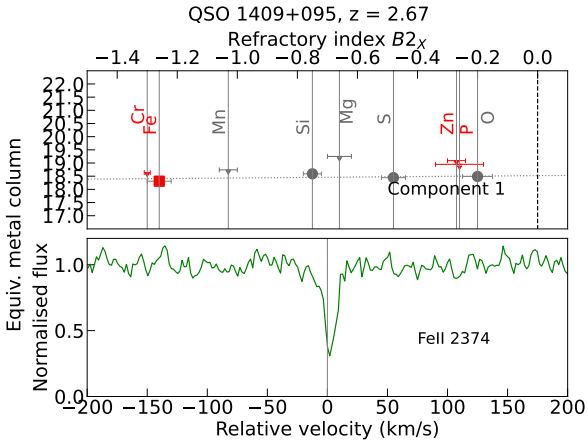

Fig. C.42. Depletion patterns and respective spectrum for QSO 1409+095.

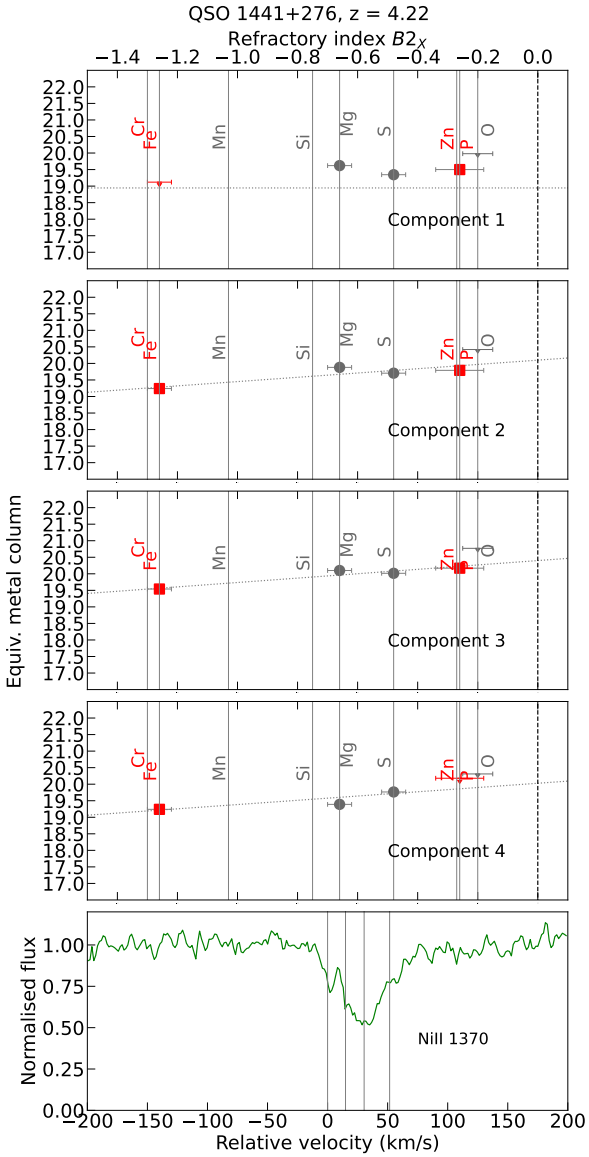

Fig. C.43. Depletion patterns and respective spectrum for QSO 1441+276.

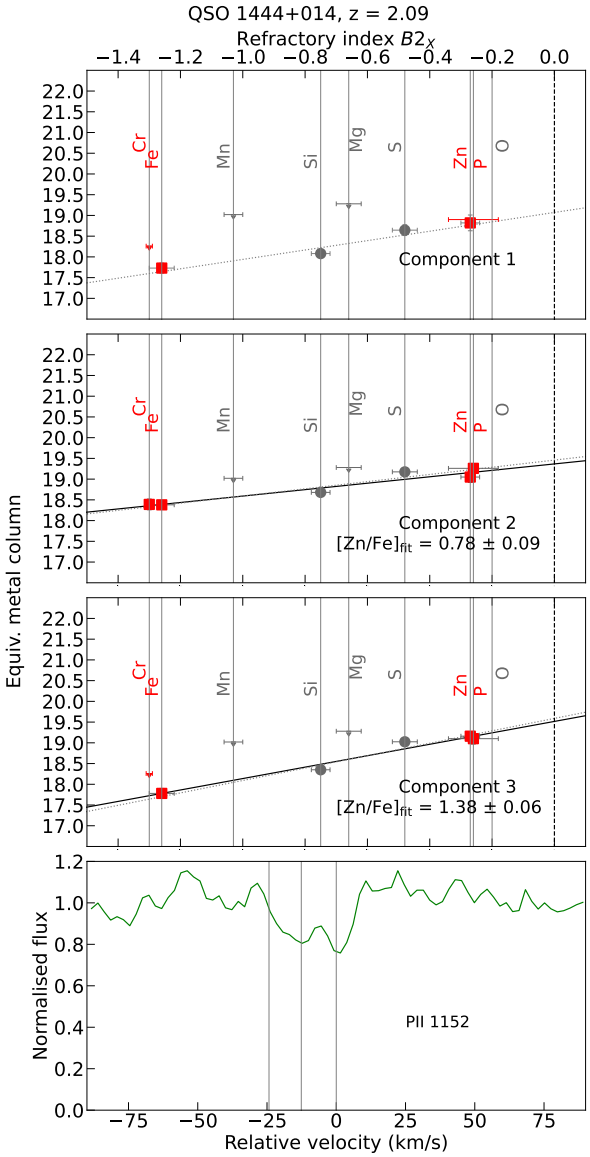

Fig. C.44. Depletion patterns and respective spectrum for QSO 1444+014.

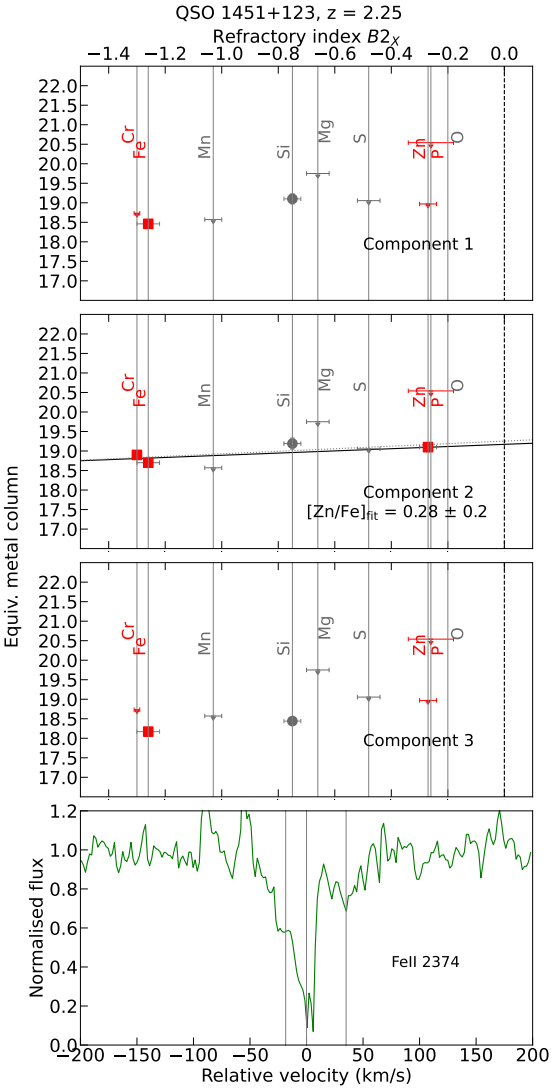

Fig. C.45. Depletion patterns and respective spectrum for QSO 1451+123.

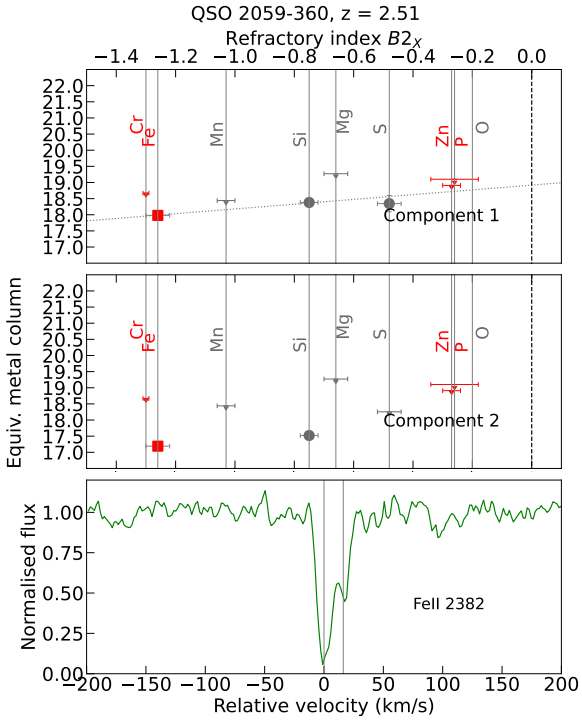

Fig. C.46. Depletion patterns and respective spectrum for QSO 2059-360.

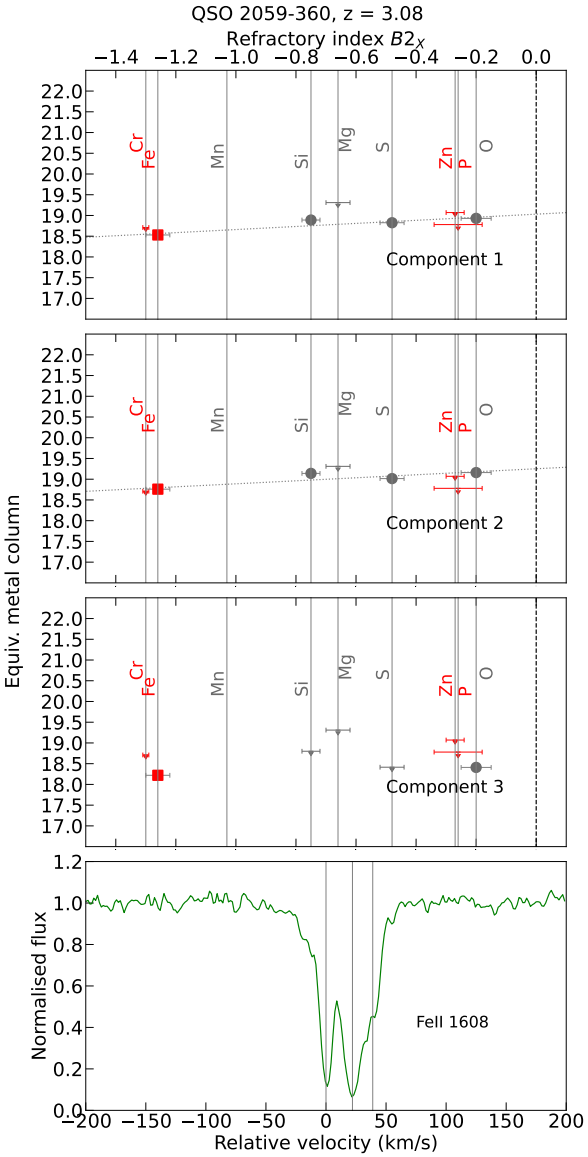

Fig. C.47. Depletion patterns and respective spectrum for QSO 2059-360.

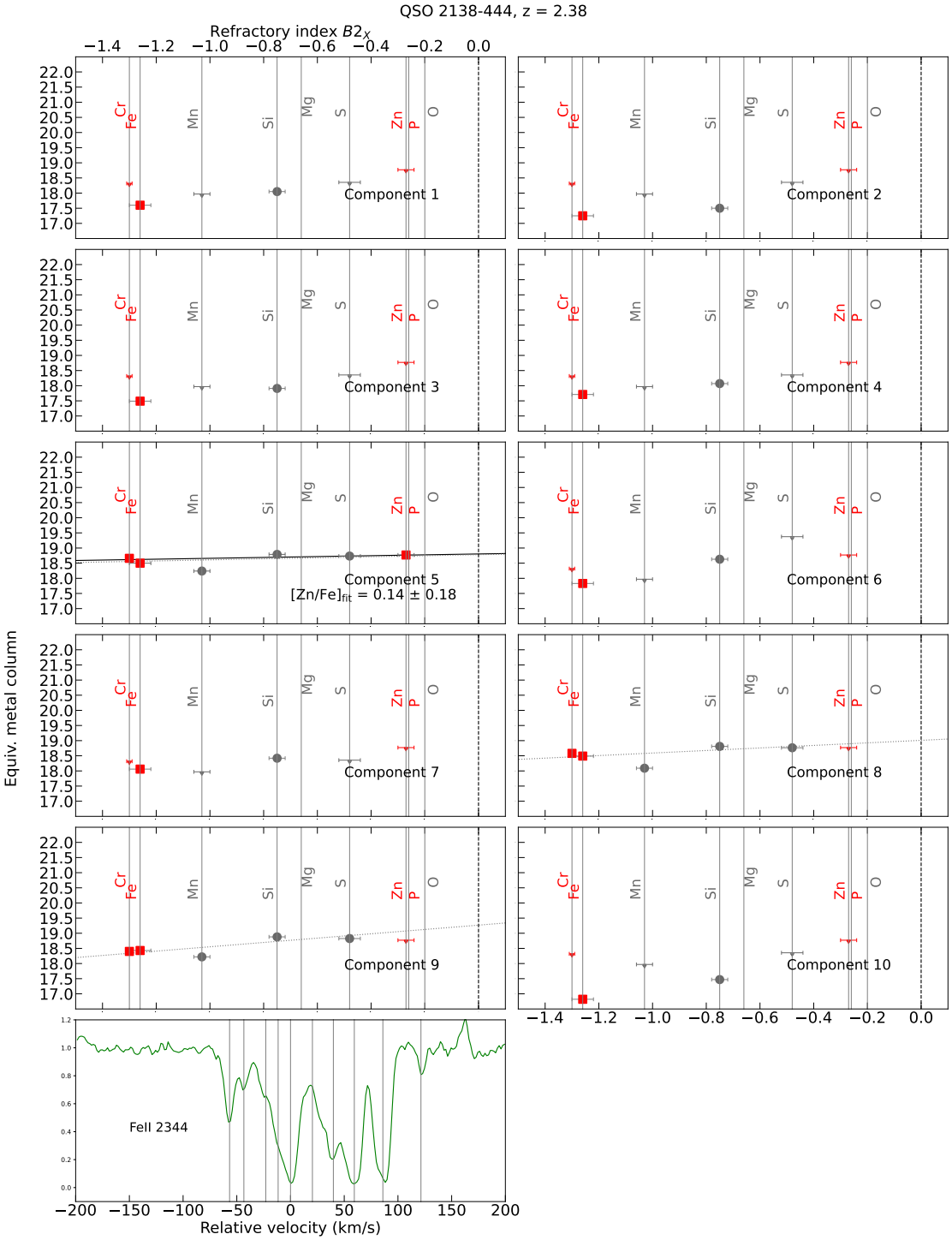

Fig. C.48. Depletion patterns and respective spectrum for QSO 2138-444.

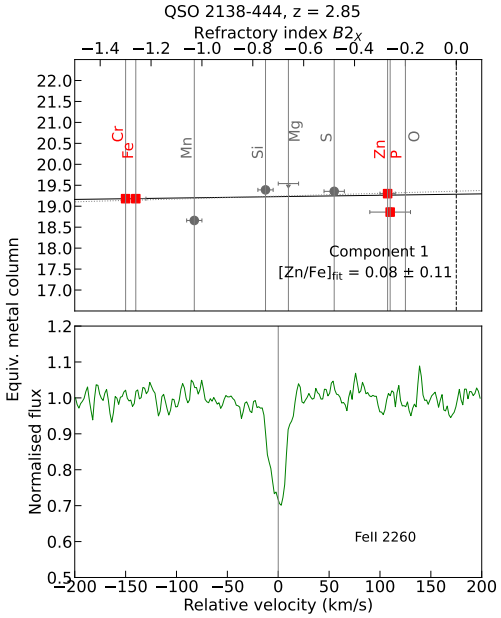

Fig. C.49. Depletion patterns and respective spectrum for QSO 2138-444.

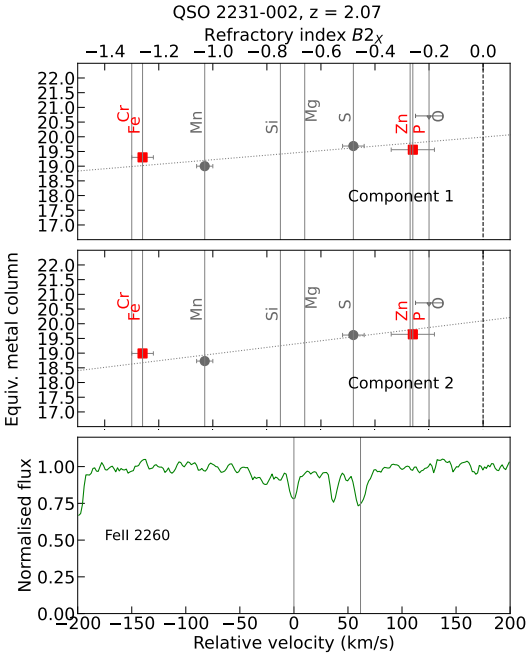

Fig. C.51. Depletion patterns and respective spectrum for QSO 2231-002.

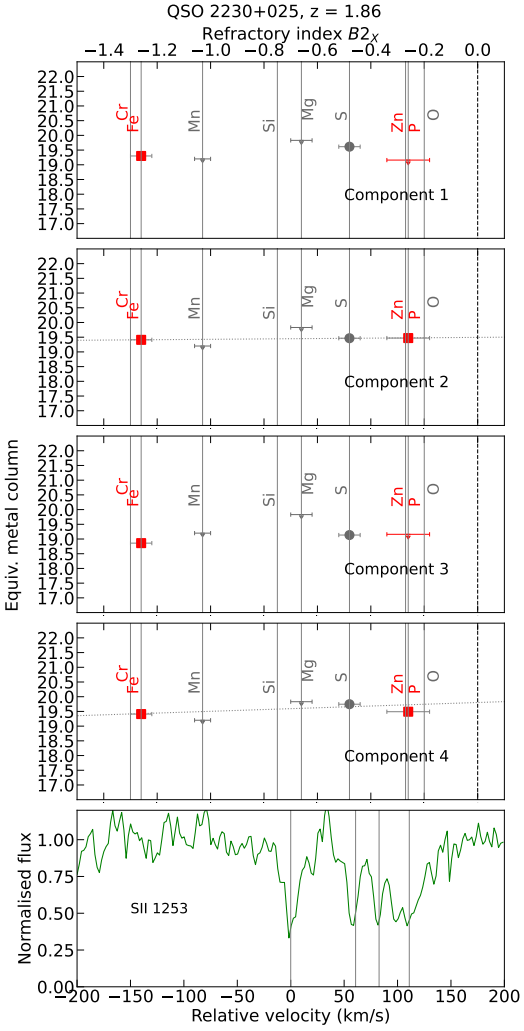

Fig. C.50. Depletion patterns and respective spectrum for QSO 2230+025.

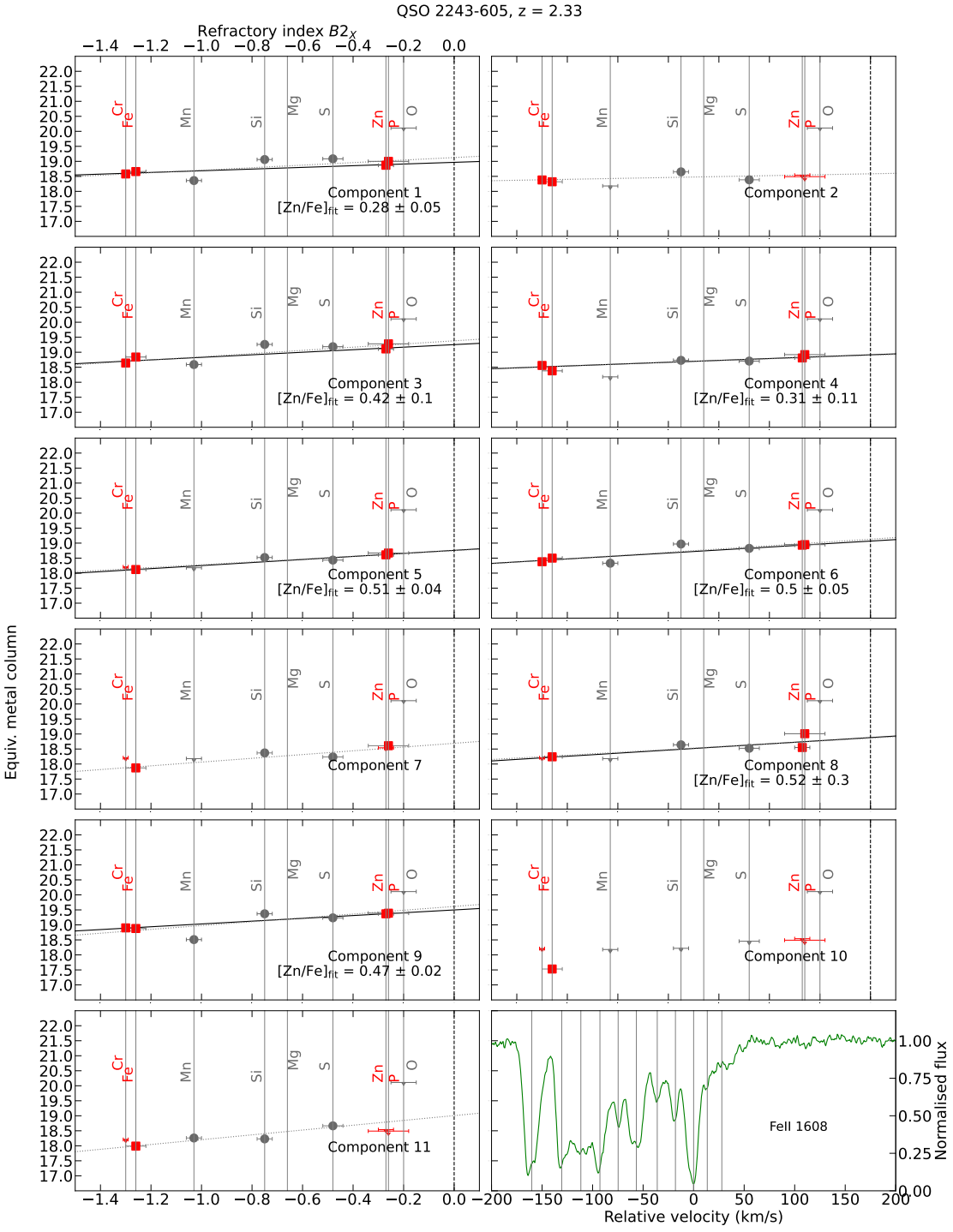

Fig. C.52. Depletion patterns and respective spectrum for QSO 2243-605.

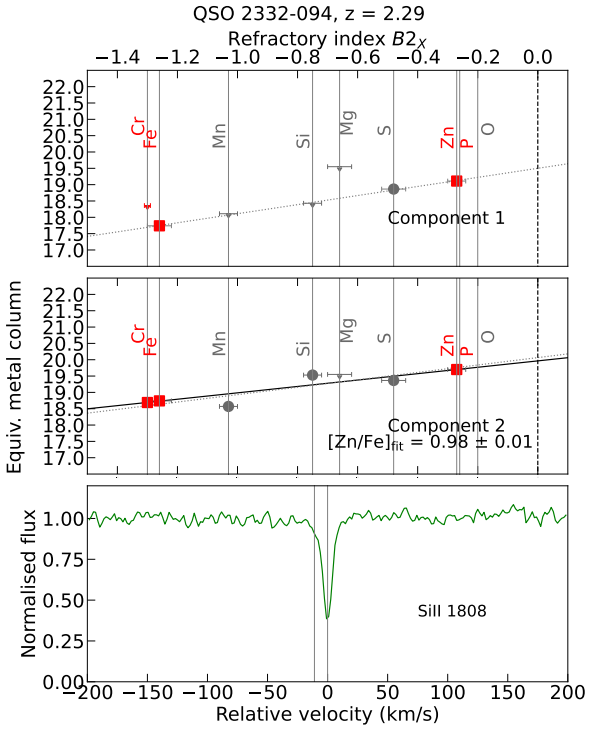

Fig. C.53. Depletion patterns and respective spectrum for QSO 2332-094.

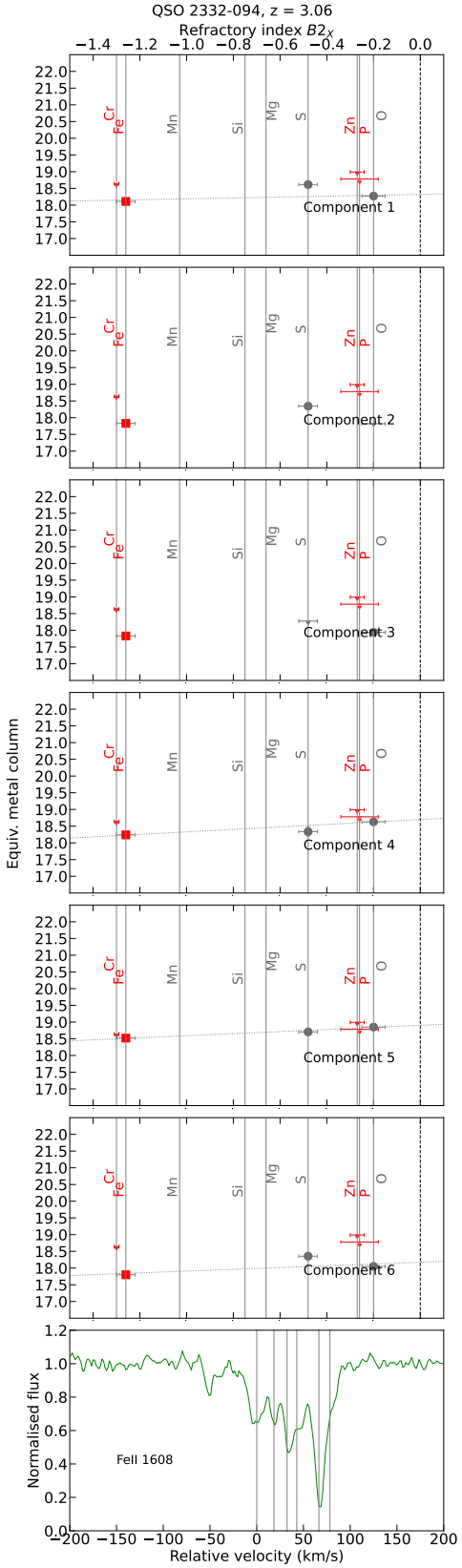

Fig. C.54. Depletion patterns and respective spectrum for QSO 2332-094.

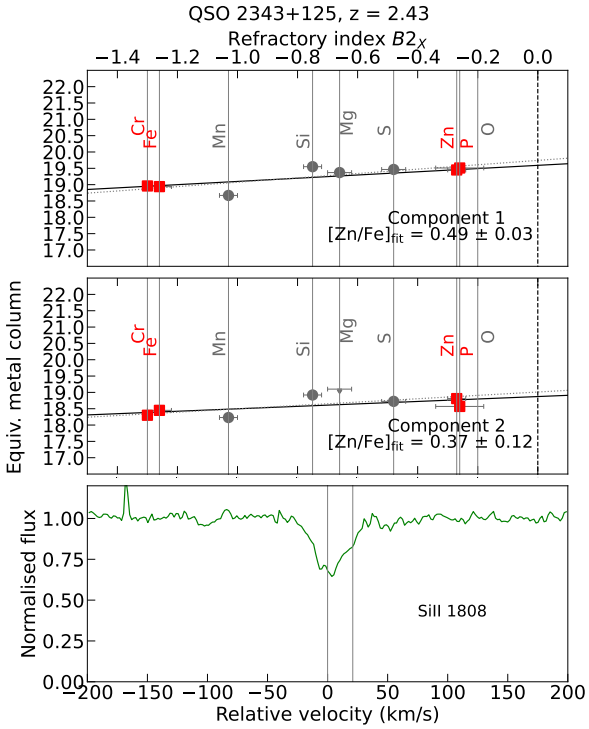

Fig. C.55. Depletion patterns and respective spectrum for QSO 2343+125.

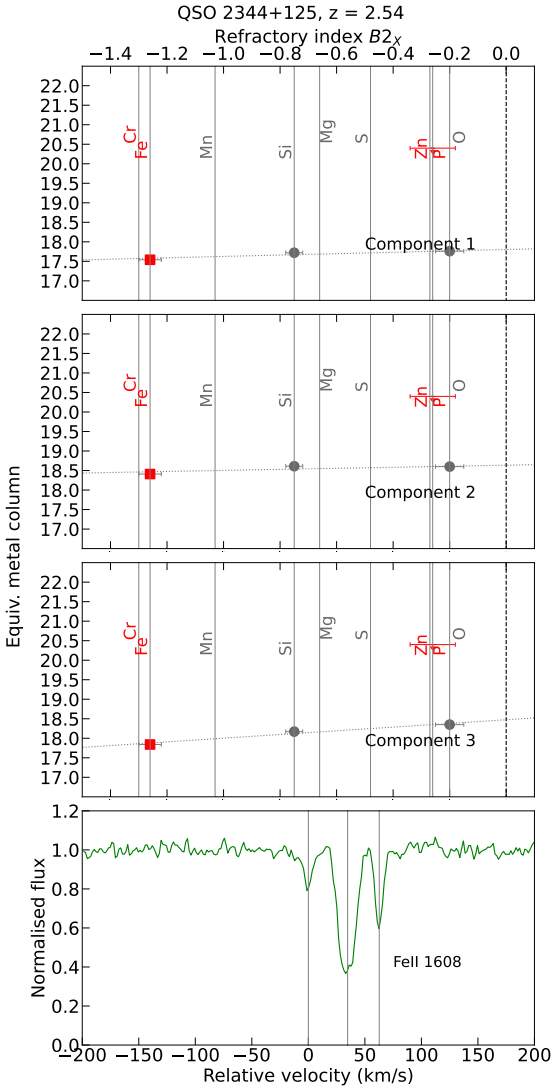

Fig. C.56. Depletion patterns and respective spectrum for QSO 2344+125.

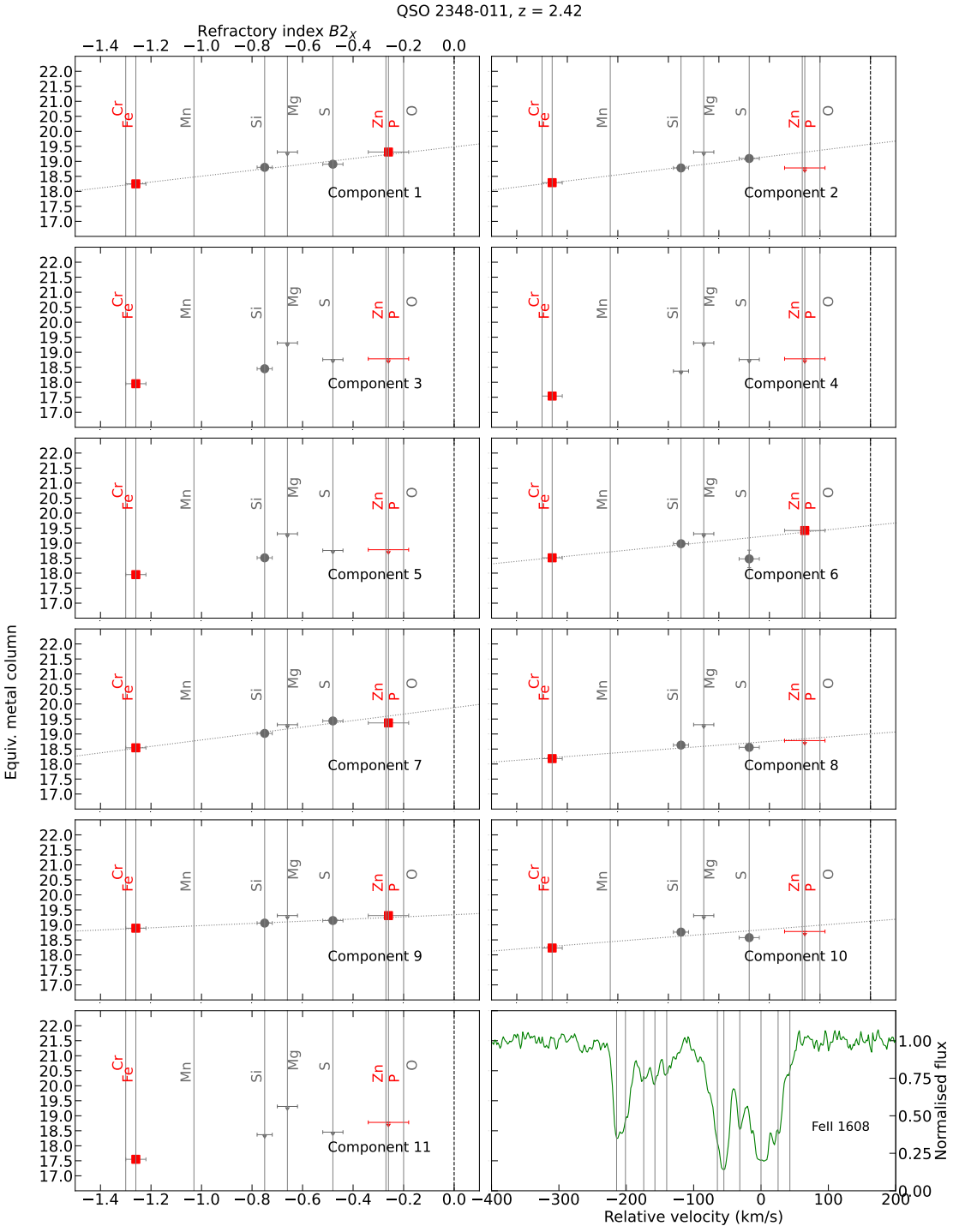

Fig. C.57. Depletion patterns and respective spectrum for QSO 2348-011.

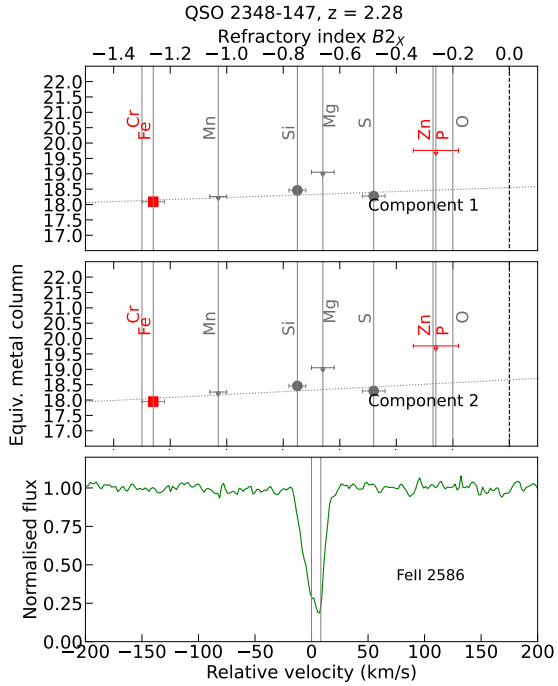

Fig. C.58. Depletion patterns and respective spectrum for QSO 2348-147.

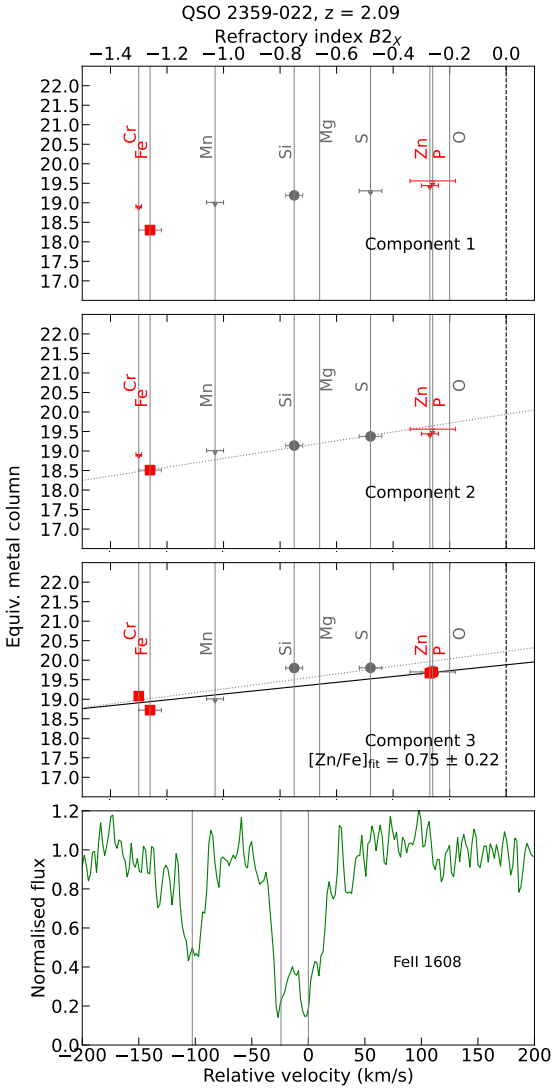

Fig. C.59. Depletion patterns and respective spectrum for QSO 2359-022.

Appendix D: Velocity-depletion plots

Figures D.1 to D.19 show the distribution of the depletion strength $[Zn/Fe]_{fit}$ with the velocity of the individual components for each system. Only systems with two or more constrained components are shown here, in total 18.

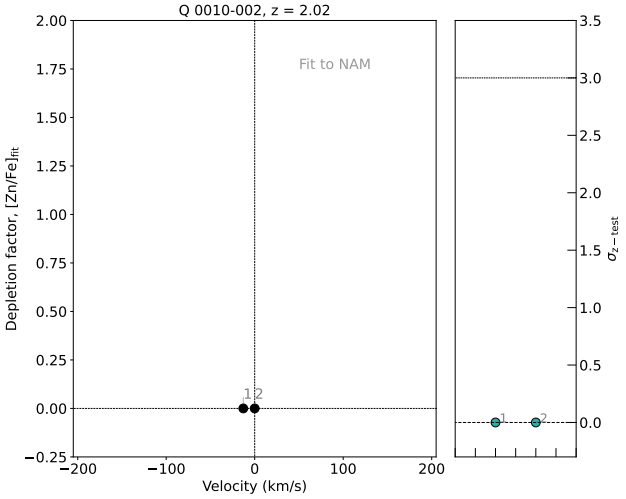

Fig. D.1. Velocity-depletion plot for DLA system towards QSO 0010-002.

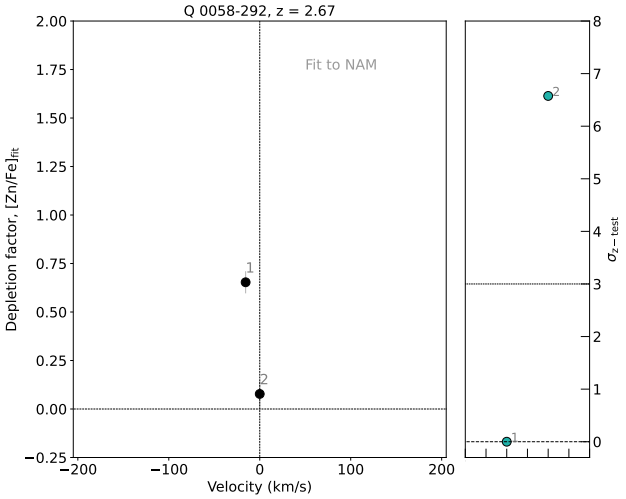

Fig. D.2. Velocity-depletion plot for DLA system towards QSO 0058-292.

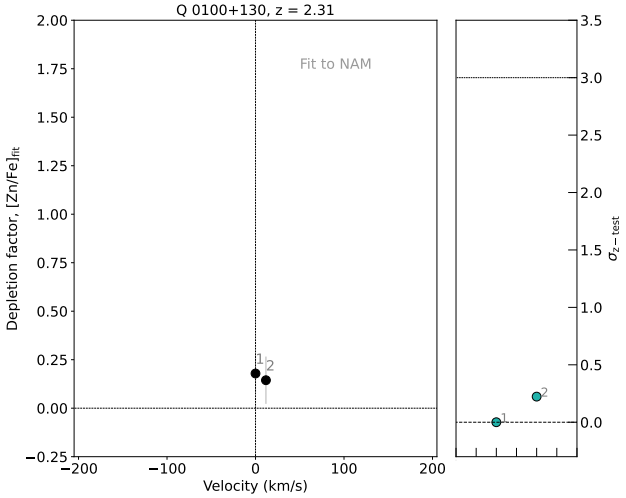

Fig. D.3. Velocity-depletion plot for DLA system towards QSO 0100+130.

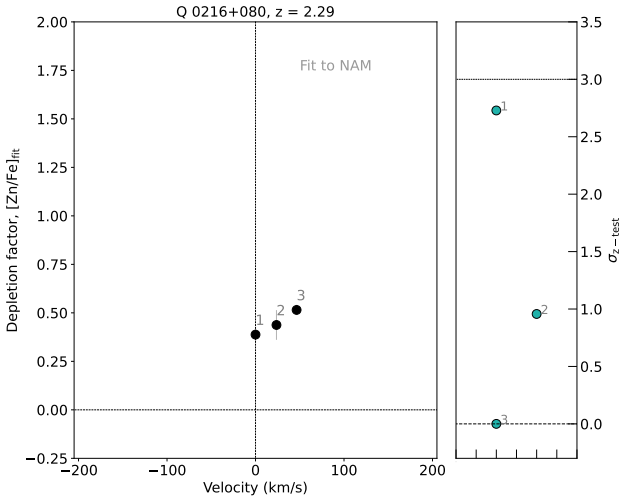

Fig. D.4. Velocity-depletion plot for DLA system towards QSO 0216+080.

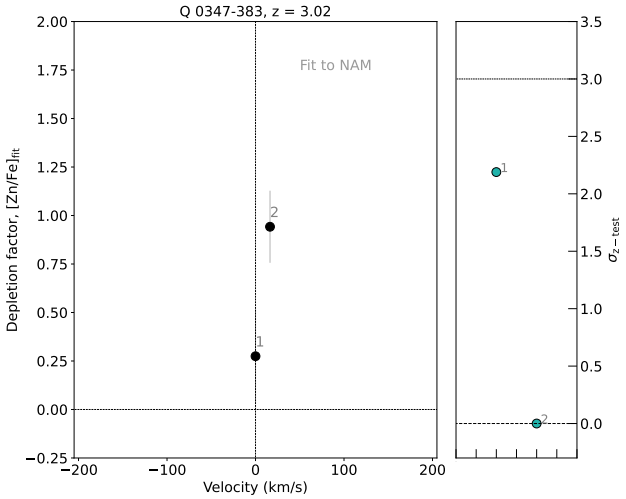

Fig. D.5. Velocity-depletion plot for DLA system towards QSO 0347-383.

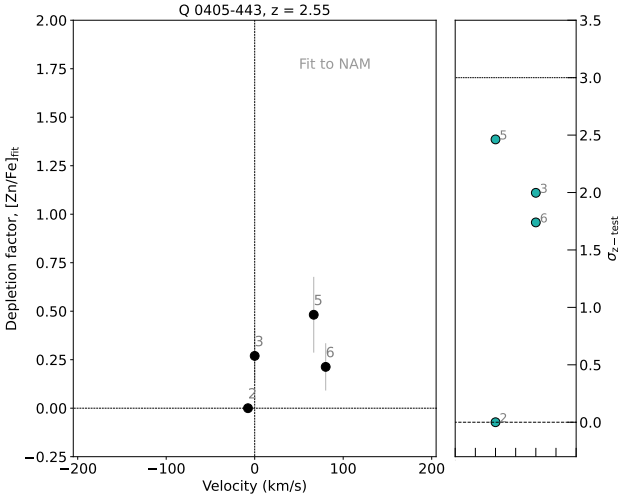

Fig. D.6. Velocity-depletion plot for DLA system towards QSO 0405-443.

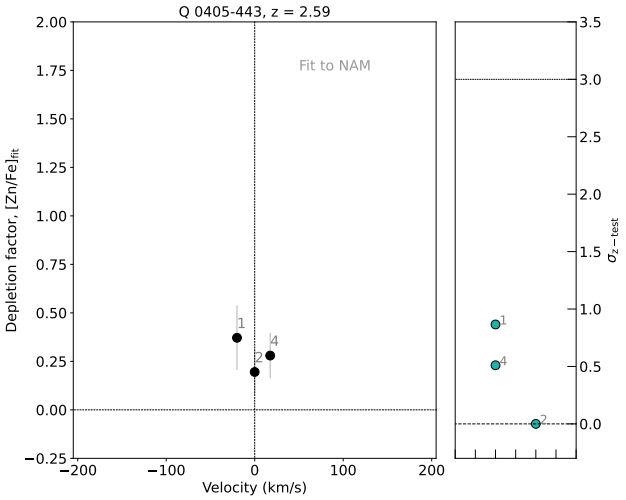

Fig. D.7. Velocity-depletion plot for DLA system towards QSO 0405-443

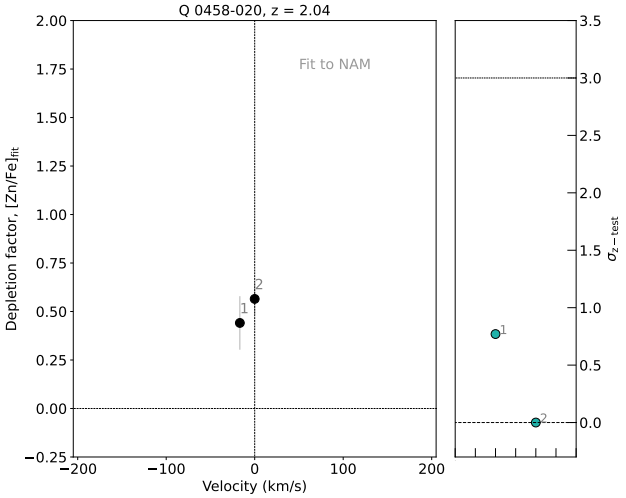

Fig. D.8. Velocity-depletion plot for DLA system towards QSO 0458-020.

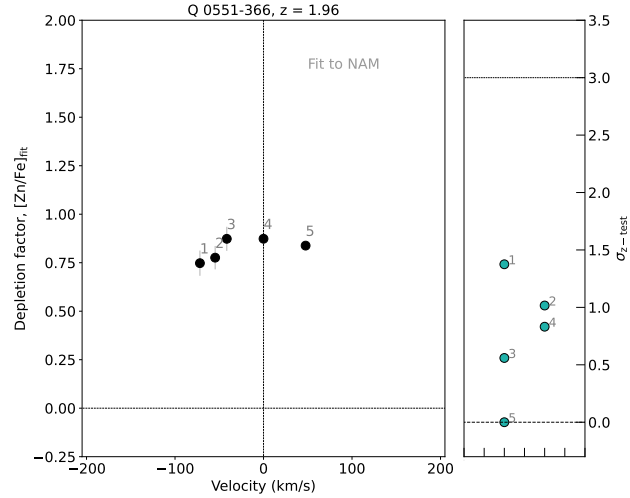

Fig. D.9. Velocity-depletion plot for DLA system towards QSO 0551-366.

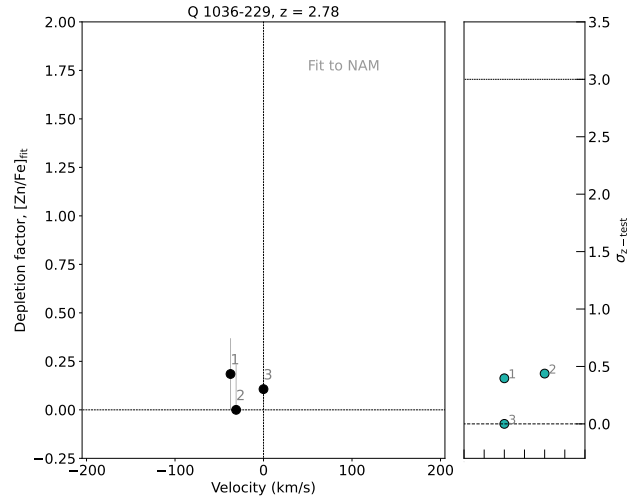

Fig. D.10. Velocity-depletion plot for DLA system towards QSO 1036-229.

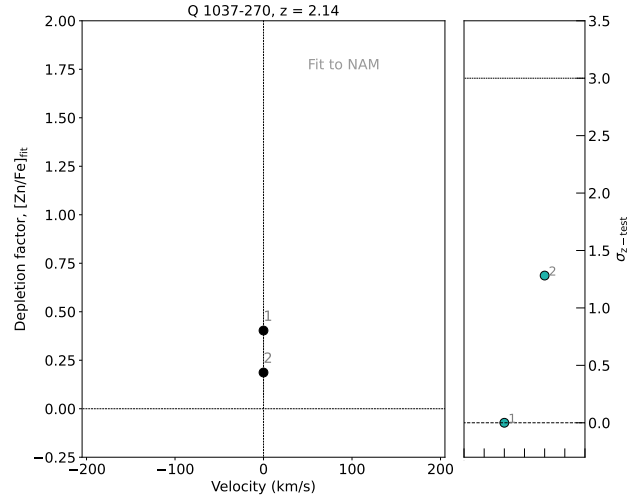

Fig. D.11. Velocity-depletion plot for DLA system towards QSO 1037-270.

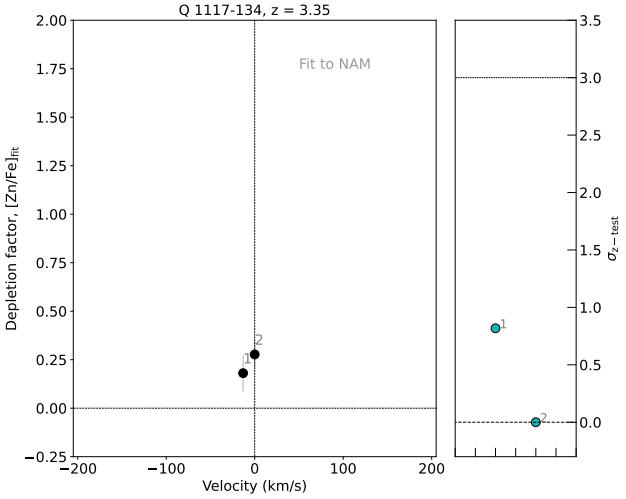

Fig. D.12. Velocity-depletion plot for DLA system towards QSO 1117-134.

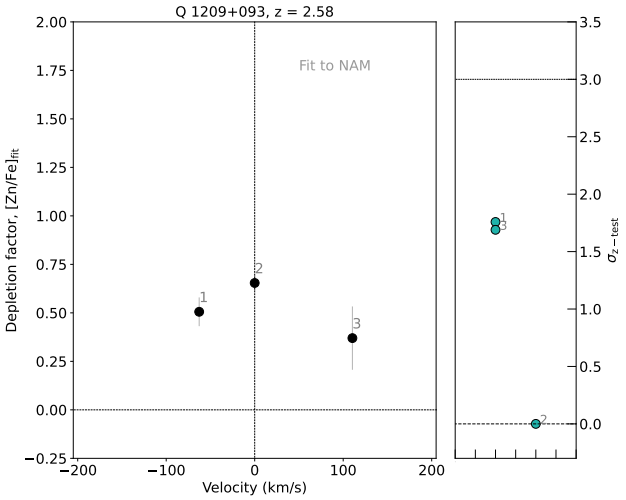

Fig. D.13. Velocity-depletion plot for DLA system towards QSO 1209+093.

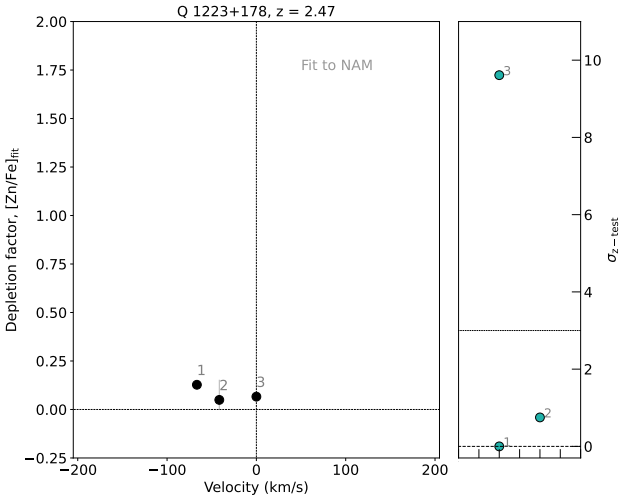

Fig. D.14. Velocity-depletion plot for DLA system towards QSO 1223+178.

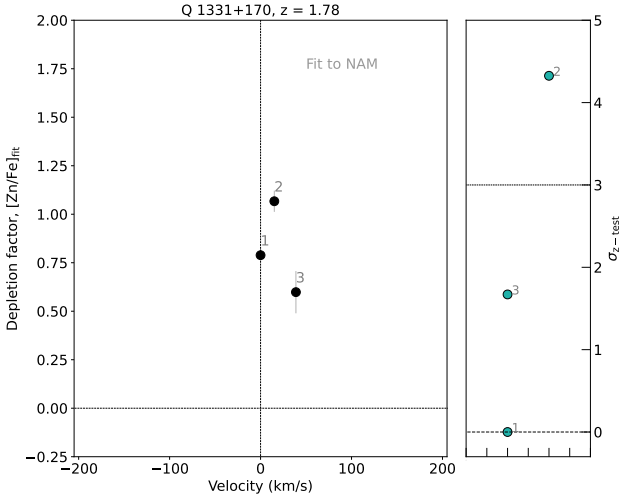

Fig. D.15. Velocity-depletion plot for DLA system towards QSO 1331+170.

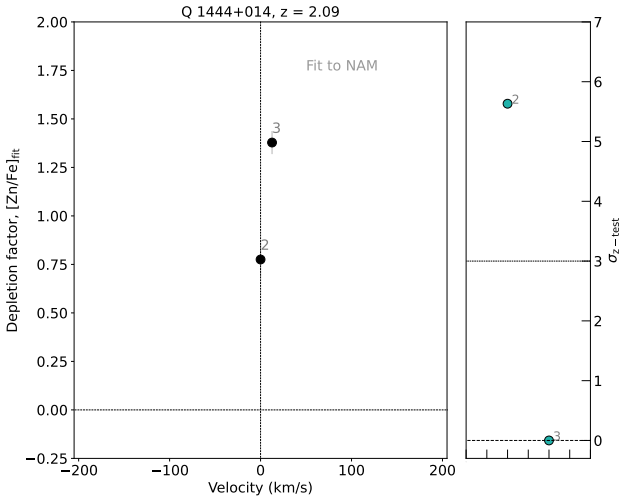

Fig. D.16. Velocity-depletion plot for DLA system towards QSO 1444+014.

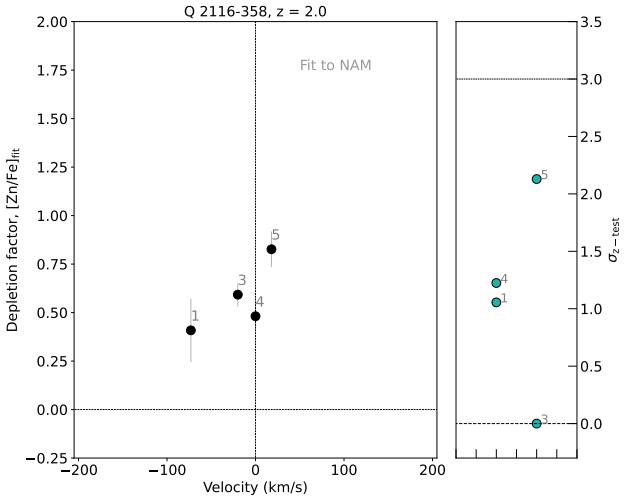

Fig. D.17. Velocity-depletion plot for DLA system towards QSO 2116-358.

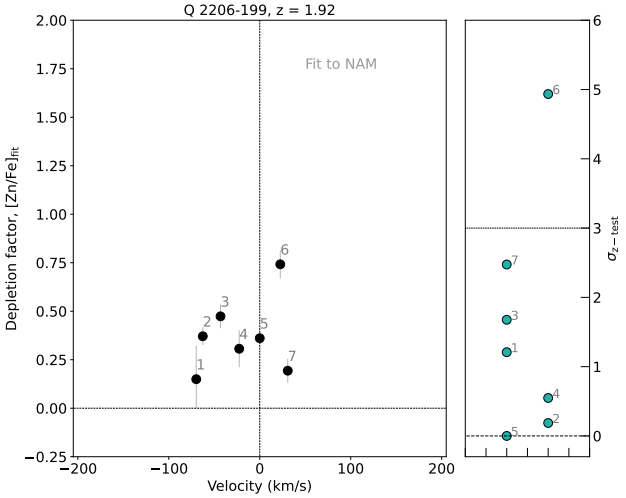

Fig. D.18. Velocity-depletion plot for DLA system towards QSO 2206-199.

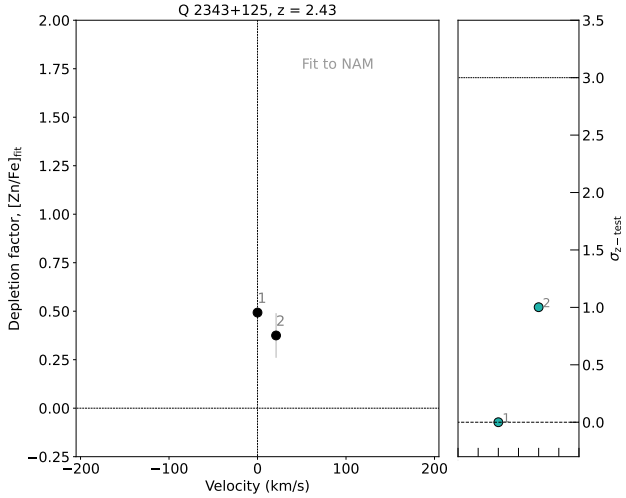

Fig. D.19. Velocity-depletion plot for DLA system towards QSO 2343+125.

Appendix E: Tables

Table E.1 lists the results from the linear fits of the depletion patterns, namely the depletion factors and equivalent metal column densities.

Table E.1. Depletion factor $[Zn/Fe]_{fit}$ and equivalent metal column density $[M/H]_{tot} + \log N(H)$ for each individual component. Values in columns 4 and 5 are calculated from a straight line fit to all the metals in the depletion patterns (all metals). Columns 6 and 7 have values calculated from fits which excluded the α-elements and Mn (NAM).

QSO	z	Comp.	$[Zn/Fe]_{fit}$ All metals	$[M/H]_{tot} + \log N(H)$ All metals	$[Zn/Fe]_{fit}$ NAM	$[M/H]_{tot} + \log N(H)$ NAM
Q0000-263	3.39013	1	0.11 ± 0.14	19.55 ± 0.14	0 ± 0.11	19.3 ± 0.11
Q0010-002	2.02471	1	0.0 ± 0.12	19.33 ± 0.12	0 ± 0.06	19.19 ± 0.06
	2.02484	2	0.07 ± 0.15	19.57 ± 0.15	0 ± 0.03	19.3 ± 0.03
Q0013-004	1.96648	1	0.23 ± 0.02	18.88 ± 0.02		
	1.9668	2	0.26 ± 0.39	18.89 ± 0.39	1.07 ± 0.29	19.28 ± 0.29
	1.96734	3	0.3 ± 0.33	19.3 ± 0.33	1.29 ± 0.08	19.18 ± 0.08
	1.96743	5	0.51 ± 0.51	19.29 ± 0.51	0.8 ± 0.13	19.52 ± 0.13
	1.96823	6	1.45 ± 0.95	19.74 ± 0.95		
	1.96999	7	0.62 ± 0.01	19.31 ± 0.01	1.46 ± 0.12	19.49 ± 0.12
	1.97027	8	1.4 ± 0.26	19.03 ± 0.26	1.07 ± 0.25	19.2 ± 0.25
	1.97102	9	1.14 ± 0.16	19.38 ± 0.16		
	1.97138	10	1.39 ± 0.15	19.33 ± 0.15	0.92 ± 0.07	19.86 ± 0.07
	1.97184	11	0.97 ± 0.16	19.76 ± 0.16		
	1.97289	14	2.32 ± 0.16	20.02 ± 0.16	1.06 ± 0.01	20.18 ± 0.01
	1.97321	15	1.48 ± 0.27	19.4 ± 0.27		
	1.97344	16	1.02 ± 0.2	19.14 ± 0.2		
	1.97367	17	0.88 ± 0.16	19.34 ± 0.16	0.35 ± 0.02	18.7 ± 0.02
	1.97381	18	1.03 ± 0.13	19.99 ± 0.13		
	1.97398	19	0.93 ± 0.16	19.16 ± 0.16		
Q0058-292	2.67123	1	1.13 ± 0.1	20.27 ± 0.1	0.65 ± 0.06	19.5 ± 0.06
	2.67142	2	1.12 ± 0.01	19.05 ± 0.01	0.08 ± 0.07	19.36 ± 0.07
Q0100+130	2.30903	1	1.02 ± 0.08	19.08 ± 0.08	0.18 ± 0.1	19.66 ± 0.1
	2.30916	2	0.51 ± 0.14	18.95 ± 0.14	0.14 ± 0.12	19.37 ± 0.12
Q0102-190	2.36958	1	0.85 ± 0.17	19.38 ± 0.17		
	2.36966	2	0.99 ± 0.12	19.27 ± 0.12		
Q0102-190	2.92625	1	0.24 ± 0.41	19.29 ± 0.41		
	2.92648	2	0.49 ± 0.06	19.89 ± 0.06		
	2.92663	3	0.43 ± 0.14	19.41 ± 0.14		
	2.92727	4	0.42 ± 0.15	19.76 ± 0.15		
	2.92772	5	0.47 ± 0.18	19.33 ± 0.18		
Q0112-306	2.41844	1	0.55 ± 0.17	19.53 ± 0.17		
	2.41861	2	0.39 ± 0.37	19.94 ± 0.37		
Q0112+030	2.42235	2	0.53 ± 0.13	19.49 ± 0.13		
	2.42277	5	0.94 ± 0.12	19.65 ± 0.12		
	2.42299	6	0.36 ± 0.15	18.99 ± 0.15		
	2.42322	7	0.3 ± 0.17	19.66 ± 0.17		
	2.42353	8	0.25 ± 0.08	18.97 ± 0.08		
	2.42332	9	0.46 ± 0.22	19.78 ± 0.22		
Q0135-273	2.10735	1	0.26 ± 0.19	18.71 ± 0.19		
Q0135-273	2.80004	1	0.09 ± 0.26	18.78 ± 0.26		
Q0216+080	1.76873	1	0.2 ± 0.27	19.11 ± 0.27	0.44 ± 0.05	19.4 ± 0.05
Q0216+080	2.29307	1	0.22 ± 0.25	19.67 ± 0.25	0.39 ± 0.04	19.67 ± 0.04
	2.29333	2	0.29 ± 0.34	19.04 ± 0.34	0.44 ± 0.08	19.22 ± 0.08
	2.29358	3	0.34 ± 0.16	18.51 ± 0.16	0.52 ± 0.03	19.43 ± 0.03
Q0336-017	3.06209	1	0.02 ± 0.34	18.43 ± 0.34	0 ± 0.18	19.02 ± 0.18
Q0347-383	3.02463	1	0.13 ± 0.17	19.15 ± 0.17	0.27 ± 0.24	19.18 ± 0.24
	3.02485	2	0.27 ± 0.13	19.45 ± 0.13	0.94 ± 0.19	19.62 ± 0.19
Q0405-443	1.91193	1	0.06 ± 0.2	18.67 ± 0.2	0.19 ± 0.08	18.67 ± 0.08

Table E.1. continued.

QSO	z	Comp.	$[Zn/Fe]_{fit}$ All metals	$[M/H]_{tot} + \log N(H)$ All metals	$[Zn/Fe]_{fit}$ NAM	$[M/H]_{tot} + \log N(H)$ NAM
	1.91208	2	0.39 ± 0.26	19.04 ± 0.26	0.0 ± 0.03	18.7 ± 0.03
	1.91235	3	0.43 ± 0.25	19.35 ± 0.25	0.07 ± 0.09	18.98 ± 0.09
	1.91267	4	0.23 ± 0.01	18.79 ± 0.01	0.12 ± 0.02	19.63 ± 0.02
	1.91279	5	0.29 ± 0.36	18.91 ± 0.36	0.14 ± 0.09	18.92 ± 0.09
	1.91302	6	0.22 ± 0.11	18.45 ± 0.11		
Q0405-443	2.54971	1	0.48 ± 0.21	20.17 ± 0.21		
	2.54991	2	0.62 ± 0.16	20.5 ± 0.16	0.0 ± 0.01	18.7 ± 0.01
	2.55	3	0.61 ± 0.26	20.47 ± 0.26	0.27 ± 0.13	19.43 ± 0.13
	2.55059	4	0.59 ± 0.19	20.1 ± 0.19		
	2.55079	5	0.93 ± 0.18	20.36 ± 0.18	0.48 ± 0.2	19.06 ± 0.2
	2.55095	6	0.96 ± 0.78	19.64 ± 0.78	0.21 ± 0.12	19.15 ± 0.12
	2.55123	7	0.19 ± 0.15	18.75 ± 0.15		
Q0405-443	2.59442	1	0.35 ± 0.24	19.59 ± 0.24	0.37 ± 0.17	18.97 ± 0.17
	2.59466	2	0.83 ± 0.1	19.8 ± 0.1	0.2 ± 0.12	19.6 ± 0.12
	2.59476	3	0.84 ± 0.15	19.35 ± 0.15		
	2.59487	4	0.94 ± 0.11	19.54 ± 0.11	0.28 ± 0.12	19.64 ± 0.12
Q0450-131	2.06658	4	0.96 ± 0.14	20.42 ± 0.14		
	2.06683	5	0.87 ± 0.1	20.02 ± 0.1		
Q0458-020	2.03939	1	0.74 ± 0.2	19.65 ± 0.2	0.44 ± 0.14	20.18 ± 0.14
	2.03956	2	0.14 ± 0.1	19.45 ± 0.1	0.56 ± 0.08	20.47 ± 0.08
Q0528-250	2.14062	1	0.07 ± 0.81	19.11 ± 0.81		
	2.14085	2	0.67 ± 0.51	19.56 ± 0.51		
	2.14105	3	0.34 ± 0.13	19.43 ± 0.13	0.19 ± 0.03	19.48 ± 0.03
Q0528-250	2.81111	1	0.32 ± 0.17	19.64 ± 0.17	0.41 ± 0.0	20.28 ± 0.0
	2.81204	2	0.2 ± 0.04	17.43 ± 0.04	0.46 ± 0.05	19.98 ± 0.05
	2.81378	3	0.18 ± 0.1	17.77 ± 0.1	0.85 ± 0.15	20.21 ± 0.15
Q0551-366	1.9615	1	0.28 ± 0.18	19.75 ± 0.18	0.75 ± 0.07	19.7 ± 0.07
	1.96167	2	0.23 ± 0.17	19.48 ± 0.17	0.78 ± 0.06	19.27 ± 0.06
	1.9618	3	0.25 ± 0.36	18.83 ± 0.36	0.87 ± 0.06	19.53 ± 0.06
	1.96221	4	0.04 ± 0.46	18.83 ± 0.46	0.87 ± 0.04	20.37 ± 0.04
	1.96268	5	0.0 ± 0.55	16.91 ± 0.55	0.84 ± 0.01	20.01 ± 0.01
Q0841+129	1.86384	1	0.03 ± 0.1	18.07 ± 0.1		
	1.86392	2	0.18 ± 0.24	17.99 ± 0.24		
Q0841+129	2.37452	1	0.0 ± 0.2	17.51 ± 0.2	0.18 ± 0.06	19.55 ± 0.06
Q0841+129	2.47622	1	0.0 ± 0.26	17.71 ± 0.26	0.13 ± 0.12	19.24 ± 0.12
Q0913+072	2.61829	1	0.35 ± 0.2	19.32 ± 0.2		
	2.61843	2	0.28 ± 0.3	19.1 ± 0.3		
Q1036-229	2.77732	1	0.33 ± 0.29	19.32 ± 0.29	0.18 ± 0.18	19.14 ± 0.18
	2.7774	2	0.65 ± 0.55	19.17 ± 0.55	0.0 ± 0.23	18.36 ± 0.23
	2.77779	3	0.65 ± 0.22	19.74 ± 0.22	0.11 ± 0.07	19.1 ± 0.07
	2.77808	4	0.38 ± 0.21	19.25 ± 0.21		
Q1037-270	2.139	1	0.04 ± 0.35	18.73 ± 0.35	0.4 ± 0.11	19.45 ± 0.11
	2.139	2	0.2 ± 0.02	19.07 ± 0.02	0.19 ± 0.12	19.08 ± 0.12
Q1108-077	3.60767	1	0.17 ± 0.08	19.14 ± 0.08		
Q1111-152	3.26536	1	0.33 ± 0.04	19.09 ± 0.04		
	3.26552	2	0.2 ± 0.34	18.78 ± 0.34	0.2 ± 0.15	19.17 ± 0.15
	3.2657	3	0.1 ± 0.79	18.25 ± 0.79		
	3.26603	4	0.43 ± 0.37	19.0 ± 0.37		
	3.26678	6	0.21 ± 0.15	19.34 ± 0.15		
	3.26704	7	0.29 ± 0.07	19.37 ± 0.07		

Table E.1. continued.

QSO	z	Comp.	[Zn/Fe]$_{fit}$ All metals	[M/H]$_{tot}$ + log N(H) All metals	[Zn/Fe]$_{fit}$ NAM	[M/H]$_{tot}$ + log N(H) NAM
Q1117-134	3.35027	1	0.4 ± 0.03	18.14 ± 0.03	0.18 ± 0.09	19.27 ± 0.09
	3.35046	2	0.05 ± 0.32	17.84 ± 0.32	0.28 ± 0.07	19.35 ± 0.07
Q1157+014	1.94317	1	0.33 ± 0.34	19.27 ± 0.34	0.05 ± 0.03	18.93 ± 0.03
	1.94349	2	0.39 ± 0.19	20.04 ± 0.19	0.26 ± 0.05	19.94 ± 0.05
	1.94376	3	0.69 ± 0.25	20.37 ± 0.25	0.48 ± 0.07	20.2 ± 0.07
	1.94403	4	0.49 ± 0.2	19.94 ± 0.2	0.36 ± 0.08	19.83 ± 0.08
Q1209+093	2.58362	1	0.67 ± 0.29	20.21 ± 0.29	0.51 ± 0.07	20.09 ± 0.07
	2.58437	2	0.9 ± 0.28	20.61 ± 0.28	0.65 ± 0.04	20.42 ± 0.04
	2.58569	3	0.57 ± 0.21	19.58 ± 0.21	0.37 ± 0.16	19.33 ± 0.16
Q1210+175	1.89158	1	0.77 ± 0.42	19.31 ± 0.42		
	1.89177	2	1.28 ± 0.68	20.54 ± 0.68		
	1.89195	3	0.93 ± 0.72	19.34 ± 0.72		
Q1223+178	2.4653	1	0.28 ± 0.22	19.48 ± 0.22	0.13 ± 0.0	19.33 ± 0.0
	2.46559	2	0.4 ± 0.27	19.47 ± 0.27	0.05 ± 0.1	19.08 ± 0.1
	2.46607	3	0.26 ± 0.23	19.71 ± 0.23	0.07 ± 0.0	19.55 ± 0.0
Q1232+082	2.33707	1	0.35 ± 0.28	18.63 ± 0.28		
	2.33771	2	1.23 ± 0.72	20.23 ± 0.72		
	2.33776	3	0.94 ± 0.09	19.6 ± 0.09		
Q1331+170	1.77635	1	1.01 ± 0.2	20.02 ± 0.2	0.79 ± 0.03	19.81 ± 0.03
	1.77649	2	1.42 ± 0.25	20.12 ± 0.25	1.07 ± 0.05	19.76 ± 0.05
	1.77671	3	0.87 ± 0.32	19.51 ± 0.32	0.6 ± 0.11	19.25 ± 0.11
	1.77685	4	0.89 ± 0.37	19.38 ± 0.37		
Q1337+113	2.50792	2	0.4 ± 0.03	18.67 ± 0.03		
Q1337+113	2.79557	1	0.32 ± 0.23	19.25 ± 0.23		
	2.79584	2	0.41 ± 0.32	18.49 ± 0.32		
Q1340-136	3.11835	1	0.22 ± 0.2	18.88 ± 0.2		
Q1409+095	2.01881	1	0.09 ± 0.13	18.52 ± 0.13	0.15 ± 0.08	18.95 ± 0.08
Q1409+095	2.45593	1	0.34 ± 0.19	18.37 ± 0.19		
	2.456	2	0.1 ± 0.06	17.53 ± 0.06		
	2.4564	3	0.29 ± 0.08	18.21 ± 0.08		
	2.45648	4	0.38 ± 0.07	18.06 ± 0.07		
Q1409+095	2.668	1	0.23 ± 0.16	19.09 ± 0.16		
Q1441+276	4.22348	1	0.0 ± 1.12	18.94 ± 1.12		
	4.22374	2	0.65 ± 0.27	20.1 ± 0.27		
	4.22401	3	0.66 ± 0.18	20.4 ± 0.18		
	4.22438	4	0.64 ± 0.24	20.03 ± 0.24		
Q1444+014	2.08667	1	1.13 ± 0.24	19.07 ± 0.24		
	2.08679	2	0.87 ± 0.13	19.46 ± 0.13	0.78 ± 0.09	19.37 ± 0.09
	2.08692	3	1.5 ± 0.19	19.59 ± 0.19	1.38 ± 0.06	19.52 ± 0.06
Q1451+123	2.25466	2	0.33 ± 0.19	19.25 ± 0.19	0.28 ± 0.2	19.17 ± 0.2
Q2059-360	2.50734	1	0.37 ± 0.1	19.03 ± 0.1		
Q2059-360	3.08261	1	0.36 ± 0.12	19.25 ± 0.12		
	3.08291	2	0.74 ± 0.15	18.92 ± 0.15		
Q2116-358	1.99542	1	0.52 ± 0.16	19.15 ± 0.16	0.41 ± 0.16	18.98 ± 0.16
	1.99578	2	0.68 ± 0.1	19.37 ± 0.1		
	1.99595	3	0.59 ± 0.07	19.35 ± 0.07	0.59 ± 0.06	19.35 ± 0.06
	1.99615	4	0.63 ± 0.2	19.7 ± 0.2	0.48 ± 0.07	19.43 ± 0.07
	1.99633	5	0.83 ± 0.07	19.52 ± 0.07	0.83 ± 0.09	19.53 ± 0.09
Q2138-444	2.38279	5	0.17 ± 0.23	18.78 ± 0.23	0.48 ± 0.07	19.43 ± 0.07
	2.38346	8	0.42 ± 0.36	19.01 ± 0.36		
	2.38376	9	0.71 ± 0.3	19.27 ± 0.3		
Q2138-444	2.85234	1	0.17 ± 0.17	19.36 ± 0.17	0.08 ± 0.11	19.29 ± 0.11
Q2152+137	3.31558	1	0 ± 0.38	17.51 ± 0.38		
Q2206-199	1.91993	1	0.43 ± 0.36	19.28 ± 0.36	0.15 ± 0.17	18.98 ± 0.17
	1.92	2	0.52 ± 0.16	19.69 ± 0.16	0.37 ± 0.05	19.57 ± 0.05
	1.92019	3	0.66 ± 0.23	19.59 ± 0.23	0.47 ± 0.06	19.4 ± 0.06

Table E.1. continued.

QSO	z Comp.	$[Zn/Fe]_{fit}$	$[M/H]_{tot} + \log N(H)$ All metals	$[Zn/Fe]_{fit}$ All metals	$[M/H]_{tot} + \log N(H)$ NAM	NAM
	1.92039	4	0.51 ± 0.24	19.23 ± 0.24	0.31 ± 0.09	19.02 ± 0.09
	1.92061	5	0.46 ± 0.15	19.93 ± 0.15	0.36 ± 0.03	19.85 ± 0.03
	1.92083	6	0.79 ± 0.07	19.84 ± 0.07	0.74 ± 0.07	19.8 ± 0.07
	1.92091	7	0.72 ± 0.35	20.12 ± 0.35	0.19 ± 0.06	19.39 ± 0.06
Q2230+025	1.86379	2	0.07 ± 0.01	19.49 ± 0.01		
	1.86427	4	0.3 ± 0.29	19.8 ± 0.29		
Q2231-002	2.06552	1	0.77 ± 0.41	19.99 ± 0.41		
	2.06615	2	1.13 ± 0.44	20.1 ± 0.44		
Q2243-605	2.32884	1	0.42 ± 0.17	19.13 ± 0.17	0.28 ± 0.05	18.97 ± 0.05
	2.32917	2	0.15 ± 0.22	18.59 ± 0.22		
	2.32938	3	0.53 ± 0.18	19.38 ± 0.18	0.42 ± 0.1	19.25 ± 0.1
	2.32959	4	0.3 ± 0.08	18.9 ± 0.08	0.31 ± 0.11	18.91 ± 0.11
	2.32979	5	0.47 ± 0.12	18.75 ± 0.12	0.51 ± 0.04	18.76 ± 0.04
	2.32999	6	0.54 ± 0.14	19.13 ± 0.14	0.5 ± 0.05	19.07 ± 0.05
	2.33022	7	0.63 ± 0.25	18.69 ± 0.25		
	2.33042	8	0.47 ± 0.21	18.86 ± 0.21	0.52 ± 0.3	18.88 ± 0.3
	2.33062	9	0.64 ± 0.22	19.61 ± 0.22	0.47 ± 0.02	19.5 ± 0.02
	2.33093	11	0.8 ± 0.17	19.01 ± 0.17		
Q2332-094	2.28737	1	0.13 ± 0.28	18.32 ± 0.28		
	2.28749	2	0.37 ± 0.08	18.7 ± 0.08	0.98 ± 0.01	19.96 ± 0.01
Q2332-094	3.05632	1	0.31 ± 0.05	18.9 ± 0.05		
	3.0569	4	0.27 ± 0.29	18.18 ± 0.29		
	3.05722	5	1.39 ± 0.05	19.5 ± 0.05		
	3.05738	6	1.13 ± 0.25	20.07 ± 0.25		
Q2343+125	2.43123	1	0.67 ± 0.19	19.74 ± 0.19	0.49 ± 0.03	19.59 ± 0.03
	2.43147	2	0.51 ± 0.21	19.01 ± 0.21	0.37 ± 0.12	18.87 ± 0.12
Q2344+125	2.53746	1	0.18 ± 0.07	17.8 ± 0.07		
	2.53787	2	0.13 ± 0.1	18.64 ± 0.1		
	2.5382	3	0.47 ± 0.1	18.47 ± 0.1		
Q2348-011	2.4245	1	0.98 ± 0.11	19.48 ± 0.11		
	2.42465	2	1.02 ± 0.04	19.57 ± 0.04		
	2.42621	6	0.85 ± 0.25	19.59 ± 0.25		
	2.42632	7	1.08 ± 0.19	19.88 ± 0.19		
	2.42659	8	0.63 ± 0.3	19.0 ± 0.3		
	2.42695	9	0.36 ± 0.05	19.34 ± 0.05		
	2.42724	10	0.66 ± 0.47	19.12 ± 0.47		
Q2348-147	2.27932	1	0.33 ± 0.36	18.55 ± 0.36		
	2.27941	2	0.48 ± 0.49	18.66 ± 0.49		
Q2359-022	2.09485	2	1.13 ± 0.08	19.94 ± 0.08		
	2.0951	3	0.96 ± 0.28	20.22 ± 0.28	0.75 ± 0.22	19.88 ± 0.22